



**Au & Pd Surfaces:
From Capping Agents to Methane Oxidation**

Ali Nasrallah

*A thesis submitted in partial fulfillment of the requirements for the degree of
Doctor of Philosophy*

April 2020

Acknowledgments

First and foremost, I would like to express my deepest gratitude to both my supervisors, Prof. Richard Catlow and Dr. David Willock. The training that they provided along with the work-related discussions that we had, have certainly contributed to my development as both a researcher and an individual.

I would also like to thank my co-workers and friends in the main building and 55 Park Place for their constant support and help. This includes: Cameron, Julien, Samantha, Stefan, Harry, Fabrizio, Mathew, Mala, Lara and Maicon. I would also like to recognise the assistance and support that I had from Dr. Alberto Roldan Martinez, Dr. Andrew Logsdail, and Dr. German Sastre. I would additionally like to thank Geroge, Moira, and Caru in the PGR office for their hard work and assistance throughout the three years.

Of course, I would like to express my sincere appreciation to the two people who have made all this possible. Thank you, mum and dad, for your constant support, love, and trust, without which I would not have become the person that I am today. I would also like to thank my siblings and all my friends in Lebanon, Switzerland, France, Italy, Spain, the United States, and the United Kingdom. This includes: Sahar, Dalia, Hasan, Nadine, Kris, Sienna, Hammam, Layth, Ahmed, Rania, Khouloud, Paula, Woody, Jenan, Corine, Rima, Mario, and Anna. Without you all, finishing my PhD would have been a lot harder.

Finally, I would like to thank Cardiff University for funding my PhD and Supercomputing Wales and the Materials Chemistry Consortium for the computational time provided on ARCHER and THOMAS.

Table of Contents

| | |
|---|----|
| Chapter 1 Introduction | 1 |
| 1.1 Why Methanol? | 1 |
| 1.2 Methane Activation | 2 |
| 1.2.1 Methane Chemistry | 2 |
| 1.2.2 Historical Context | 4 |
| 1.2.3 Methane in Nature | 5 |
| 1.3 Noble Metal Catalysts..... | 6 |
| 1.3.1 Au and Pd | 6 |
| 1.3.2 Transition metal doped graphene on Ni (111) surfaces | 14 |
| 1.4 Iron- and Copper- containing Zeolites | 16 |
| Chapter 2 Theoretical Background | 21 |
| 2.1 The Schrödinger Equation | 21 |
| 2.2 Electron Density | 23 |
| 2.3 Density Functional Theory..... | 25 |
| 2.3.1 Hohenberg-Kohn Theorems | 25 |
| 2.3.2 Kohn-Sham Approach..... | 26 |
| 2.3.3 Approximations of the Exchange-Correlation Functional..... | 28 |
| 2.4 Plane Wave Basis Functions | 30 |
| 2.5 Pseudopotentials | 32 |
| 2.6 Vibrational Frequency Calculations | 34 |
| 2.7 Nudged Elastic Band and Dimer Method | 36 |
| 2.8 Density of States..... | 38 |
| 2.9 Implementation of DFT..... | 39 |
| Chapter 3 Partial Oxidation of Methane to Methanol on Au and Pd Surfaces..... | 41 |
| 3.1 Introduction..... | 41 |

| | |
|--|-----|
| 3.2 Computational Details | 44 |
| 3.3 Methodology | 46 |
| 3.4 Results and Discussion..... | 51 |
| 3.4.1 Adsorption and cleavage of hydrogen peroxide on the surface..... | 51 |
| 3.4.2 Hydrogen abstraction from Methane..... | 56 |
| 3.4.3 Formation of the Methyl Peroxyl Intermediate | 60 |
| 3.4.4 Formation and Adsorption of the methyl hydroperoxide on the surface | 75 |
| 3.4.5 Role of the oxygen atom on the surface | 82 |
| 3.4.6 Effect of periodic interactions on adsorption energies and activation barriers | 84 |
| 3.5 Conclusions..... | 87 |
| Chapter 4 Doped Au and Pd Surfaces..... | 88 |
| 4.1 Introduction..... | 88 |
| 4.2 Computational Details and Methodology | 90 |
| 4.3 Results and Discussion..... | 94 |
| 4.3.1 Oxygen Adsorption and Cleavage..... | 94 |
| 4.3.2 Formation of the Methyl Peroxyl Radical | 96 |
| 4.4 Conclusions:..... | 101 |
| Chapter 5 DFT-assisted Spectroscopic Studies on the Coordination of Small Ligands to Palladium: From Isolated Ions to Nanoparticles..... | 102 |
| 5.1 Introduction..... | 102 |
| 5.1.1 Stabilisation of Metal Nanoparticles: | 102 |
| 5.1.2 Effect on Catalysis..... | 105 |
| 5.2 Computational Details | 107 |
| 5.3 Results and Discussion..... | 109 |
| 5.4 Conclusion | 118 |
| Chapter 6 Summary and General Conclusions | 119 |

| | |
|---|-----|
| References:..... | 123 |
| Appendix: QM/MM Studies of Fe and Cu Containing Zeolites..... | 129 |

List of Papers/Publications:

1. J. Carter, N. Dummer, Y. Chow, C. Williams, A.Nasrallah, D. J. Willock, G.J.Hutchings, S.H.Taylor, *The Selective Oxidation of Methane to Oxygenates using Heterogeneous Catalysts*, Book Chapter, Submitted.
2. A.Nasrallah, J.Engel, D.J.Willock, C.R.A.Catlow, *Density Functional Theory Study of the Partial Oxidation of Methane to Methanol on Au and Pd Surfaces*, ACS Catalysis, Submitted.
3. S. Campisi, C. Beevers, A. Nasrallah, C. R. A. Catlow, C. E. Chan-Thaw, M. Manzoli, N. Dimitratos, D. J. Willock, A. Roldan and A. Villa, *DFT-assisted Spectroscopic Studies on the Coordination of Small Ligands to Palladium: From Isolated Ions to Nanoparticles*, *J. Phys. Chem. C*, , DOI:10.1021/acs.jpcc.9b09791.
4. N.Agarwal, L.Thomas, A.Nasrallah, M.Sainna, S.Freakley, J.Edwards, C.R.A. Catlow G.J.Hutchings, S.H.Taylor, D.J.Willock, *The in-situ production of hydrogen peroxide over Au and Pd nanoparticles: A DFT study*, Catalysis Today, Submitted.

Summary

This thesis uses Density Functional Theory (DFT) to study the applications of transition metal surfaces in the fields of catalysis and nanoparticle synthesis. Chapter 1 provides the reader with a detailed literature review on methane oxidation, methanol synthesis, and an outlook on the different catalysts that have been used for methane activation. Chapter two then addresses the theoretical background of DFT and the different methods used.

The work produced in this thesis is then split into two main sections:

Section 1 which encompasses chapters 3 and 4 covers the partial oxidation of methane to methanol on Au and Pd surfaces. By modelling two low index surfaces of Au and Pd, we studied the partial oxidation of methane to methanol using hydrogen peroxide and molecular oxygen as oxidants. We performed a detailed study of the reaction mechanism by modelling the adsorption of intermediary species and the activation energy barriers for each of the steps. The results obtained were then used to explain why the alloy is catalytically superior to the pure metals and the different steps at which the pure surfaces fail to catalyse. Once identified, we then model doped surfaces in order understand how the alloy would tackle the problems associated with the pure metal surfaces. The results obtained show that the Pd surfaces are too active for molecular oxygen to an extent that upon adsorption, the molecule cleaves on the surface with a small barrier to form two oxygen metal-bound atoms. The Au surfaces on the other hand, show an opposite effect with a very endothermic energy of reaction for the displacement of water by molecular oxygen. Upon modelling the doped system, an improved binding of molecular oxygen on the Pd-doped Au surfaces is observed along with a decrease in the affinity of the Au-doped Pd surfaces to molecular oxygen.

Section 2 which comprises of chapter 5 discusses the use of capping agents in nanoparticle synthesis. The chapter first describes the importance of the use of capping agents in the stabilisation of nanoparticles in nanoparticle synthesis. Hetero-atom containing ligands provide a main class of capping agents used experimentally and thus using DFT, we study how aminopropanol can be used as a capping agent for the synthesis of Pd nanoparticles. By modelling the adsorption of aminopropanol on Pd surfaces and plotting IR spectra, we rationalise how aminopropanol, a ligand made of two heteroatoms, binds to Pd nanoparticles. Our adsorption energies and IR spectra show that 3-amino-propan-1-ol prefers

to bind to the Pd surfaces through the amino-group. This was further supported by a comparison of the computed IR and experimental spectra which show strong correlation. Chapter 6 provides general conclusions regarding the significance of the results in all three chapters

Chapter 1 Introduction

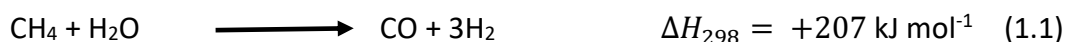
This thesis focuses on the partial oxidation of methane to methanol using heterogenous catalysis – one of the most important and long-standing challenges in catalytic science. Au and Pd metal surfaces along with iron-containing zeolites are studied for this reaction. In this chapter, we provide an introduction to the field and to previous experimental and computational studies.

We note that some of the work in this chapter is taken from reference 1 in the list of publications on page (vi) of which the author of this thesis is a co-author. The author's main contribution in this publication involved a thorough literature review on the computational aspect of methane to methanol oxidation.

1.1 Why Methanol?

Natural gas, a fossil fuel that is composed of 70 to 90% methane, has been utilised for its energy content for a long time. Our consumption of natural gas has drastically increased over the years. According to the U.S. Energy Information Administration (EIA), the consumption of natural gas is set to increase to levels as high as 203 trillion cubic feet (Tcf) in 2040 from just 120 Tcf in 2012 with the industrial and electric power sectors accounting for 73% of the increase¹. In the industrial sector, a major part of the demand for natural gas is the use of methane as a raw material to produce other valuable chemicals such as methanol and olefins.

Large-scale production of methanol happens via two routes: Fischer-Tropsch or Methane-to-Gasoline synthesis.² Both processes require the conversion of methane to syn-gas (a mixture of CO and H₂) first using alumina supported nickel catalysts. However, the production of syngas is a highly endothermic process that is traditionally produced by steam reforming:



Thus, the development of a direct route to convert methane to other C₁ oxygenates such as methanol and formaldehyde would be of very considerable value for industry and as a result the demand for such routes has led to extensive research in this area by both academic and industrial researchers.

Methanol is considered to be one of the most important C₁ oxygenates in the industrial world due to its high scale production and role as a versatile platform chemical³.

Methanol acts as a valuable non-crude oil source for the production of olefin based petrochemicals through the methanol-to-olefin (MTO) or methanol-to-propylene (MTP) processes^{4,5}. Methanol is also used for the production of dimethyl ether through a dehydration reaction catalysed by acidic compounds such as γ -alumina, silica-alumina, zeolites (HZSM-5, NaHZSM-5, HY, Ferrierite), mesoporous materials (MCM and SAPO families), or ZrO_2 ⁶. Along with methanol, dimethyl ether is a key intermediate for the production of liquid fuels such as gasoline, kerosene, and gasoil. It is also used as a propellant for spray cans, a low boiling point solvent, and a foaming agent for polystyrene insulating material³.

Another important path for methanol use is in the production of acetic acid and formaldehyde. Acetic acid is produced by the carbonylation of methanol using the Monsanto and Cativa processes which use rhodium- and iridium-based catalysts respectively⁷.

Industrially, methanol is converted to its aldehyde by oxidative dehydrogenation in the presence of a silver catalyst (BASF process) or in the presence of iron-molybdenum-vanadium oxide catalysts at 250–400°C (FORMOX process)³.

1.2 Methane Activation

1.2.1 Methane Chemistry

Methane activation is often referred to as one of the “Holy Grails of Catalysis⁸,” which is primarily due to the difficulty associated with the activation of the methane C–H bond. As a result of its perfectly symmetrical tetrahedral structure, methane is a stable hydrocarbon with its C–H energy of dissociation equivalent to 440 kJ mol⁻¹. Therefore, harsh reaction conditions are needed to activate methane which makes it thermodynamically challenging to preserve and isolate methanol as a product.

Moreover, the energy of dissociation of the C–H bond of methanol is 47 kJ mol⁻¹ lower than that of the methane C–H bond. As a result, methanol is highly vulnerable to over oxidation under these reaction conditions to produce CO₂ and water. Another reason for the higher activity of methanol as opposed to methane is polarity. Since methanol is a polar molecule, it is easier for it to adsorb on the surface of a catalyst and become activated for oxidation. Thus, an ideal catalyst should not just be able to activate methane for oxidation but also inhibit its further oxidation to undesired compounds such as carbon dioxide⁹.

It has been previously shown that the activation of the C–H bond can proceed via two routes: Upon the cleavage of the C–H bond, the methyl group can then either be (1) stabilised by the catalyst or (2) a radical-like intermediate is formed where the methyl group is stabilised by a hydroxyl bond. Therefore, the type of the catalyst present has a huge effect on which route the reaction mechanism proceeds. In catalysts where the active site is isolated such as in zeolites and other porous materials, the reaction proceeds via the second route. On the other hand, catalysts with a high density of active sites (such as metals) will normally proceed via a surface stabilised structure¹⁰.

However, recent work by Nørskov and co-workers suggested that the catalyst structure is not the only determining factor and that reactivity needs to be taken into account in order to determine the route with the lowest transition state^{10,11}.

The group studied the hydrogen abstraction from methane via the two routes on both pure and oxygen-promoted face centred cubic (fcc) (111) metal surfaces. DFT calculations were performed to determine whether it is possible for the hydrogen abstraction step to proceed via a radical like transition state on the pure (111) surfaces. However, since no saddle points were found between the initial state and the radical final state, the radical transition state energy was approximated to be that of $\text{CH}_3\bullet + \text{H}^*$. The same was then repeated on the oxygen-promoted metal surfaces. Contrary to expectation, the reaction mechanism for Au and Ag proceeded through a radical-like transition state and a surface stabilised transition state could not be determined. This was rather an odd observation as both Au and Ag (111) surfaces are capable of a surface-stabilised transition state. This led the research group to believe that the preference for these noble metals to proceed via a radical-like transition state depends on the electronic structure as well.

Transition state energies were then plotted against the hydrogen abstraction energy (E_{H}):

$$E_{\text{H}} = E(\text{M}_m\text{O}_x\text{H}_{y+1}) - E(\text{M}_m\text{O}_x\text{H}_y) \quad (1.2)$$

where $E(\text{M}_m\text{O}_x\text{H}_{y+1})$ and $E(\text{M}_m\text{O}_x\text{H}_y)$ are the formation energies of the hydrogenated and the dehydrogenated active sites respectively.

A major feature of the plot plotted by the group was that the oxygen-promoted noble catalysts had the most favourable hydrogen abstraction energy. This was explained by considering the effect of the promoting species on the catalyst. A promoter on a noble

metal catalyst (oxygen in this case) is weakly bound making the hydrogen abstraction energy favourable. Moreover, the transition state barriers for the oxygen-promoted Au and Ag were quite low with energies very similar to that of Pd and Pt.

This method of studying catalysts' ability at hydrogen abstraction can be used as a universal indicator in determining which catalysts are best suited for this reaction. This is an important contribution to the catalysis community as it would allow the determination of the route down which the catalyst will proceed for C–H bond activation. After the screening process is performed, other factors such as selectivity of product formation can then be further examined.

1.2.2 Historical Context

Research on methane oxidation took off at the beginning of the 20th century when Lance and Elworthy studied the oxidation of methane to methanol using hydrogen peroxide in the presence of ferrous sulphate¹². This work opened the door for the further investigation of iron oxides and sulphates as potential catalysts for the reaction.

Soon after, Newitt and Haffner¹³ began their work on the design of high-pressure methane combustion systems which demonstrated the production of methanol and formaldehyde at pressures as high as 107 bar. They claimed that an increase in pressure resulted in an increase in the product yield and the methanol to formaldehyde ratio.

Boomer and Thomas then built on the work of Newitt and Haffner by studying an electrolytic copper catalyst to determine the influence of several parameters on the production of methanol¹⁴. Their work concluded that the yield was strongly influenced by the concentration of oxygen and temperature. Nevertheless, the efficiency of these high-pressure combustion systems was low with a methanol selectivity lower than 60% for 1.6% of converted methane.

In order to understand the reason for this low selectivity, Boomer and Naldrett then investigated the mechanism of the reaction. Their work suggested that the formation of methanol is a result of a surface reaction between methane and oxygen. However, a second homogenous gas phase reaction between oxygen and methane in an activated or atomic form, resulted in the formation of the aldehyde¹⁴.

After the end of the second world war, Boomer and Naldrett moved away from copper catalysts and explored other catalysts such as silver, zinc, and nickel-based catalysts¹⁵.

At the same time, several Russian scientists examined oxides of zinc, cobalt, aluminium,

and molybdenum for the oxidation of methane to methanol. Work performed by Atroshchenko *et al.*¹⁶ demonstrated the activity of molybdenum trioxide and chromium oxide for the partial oxidation of methane at elevated temperatures.

This led Dowden and Walker to commence their work on a family of oxides based on molybdenum. The most active catalyst was found to be $\text{Fe}_2\text{O}_3(\text{MoO}_3)_3$ where the space-time yield of methanol was $869 \text{ g}(\text{kg}_{\text{cat.}})^{-1} \text{ h}^{-1}$ at 713 K and 30 bar with a selectivity of 19% at 2.3% methane conversion over molybdenum oxide with an increased selectivity of 51% upon the introduction of zinc oxide as a second component¹⁷.

1.2.3 Methane in Nature

Methanotrophic bacteria also known as methanotrophs are a physiological group of bacteria known for their unique ability to utilise methane as their main source of energy. These organisms use enzymes known as methane monooxygenases (MMOs) to convert methane to methanol¹⁸.

The oxidation of methane by aerobic methanotrophs use MMOs that utilise two reducing equivalents to split the O–O bond of molecular oxygen. One of the oxygen atoms is then reduced to water whilst the other is used to form methanol. There are three main components present in all MMOs: the hydroxylase component which contains nonheme iron, the B component which is a colourless protein with no cofactors, and the reductase component which contains flavin adenine dinucleotide and an $[\text{Fe}_2\text{S}_2]$ cluster¹⁸.

The dimeric protomer structure of the hydroxylase component contains three subunits (α, β, γ) and a hydroxo-bridged di-nuclear iron cluster. The structure of the hydroxylase component is shown in figure 1.1. It is known that all biologically evolved catalytic cycles for the oxidation of methane involve this di-iron complex¹⁹.

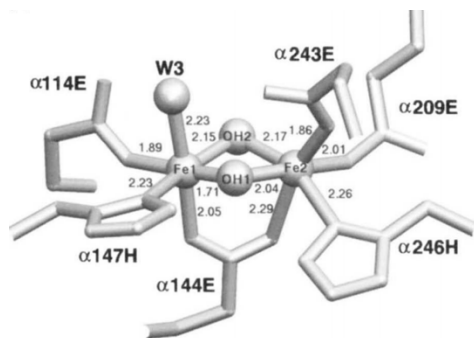


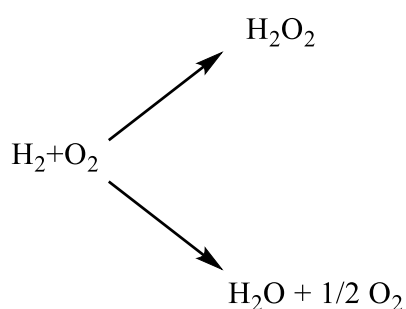
Figure 1.1: Hydroxylase component of the MMO enzyme with the di-iron active site^{18,19}.

1.3 Noble Metal Catalysts

1.3.1 Au and Pd

The use of noble metal catalysts such as Au and Pd for the total and selective oxidation of many organic compounds has shown promising results. In particular, Au has been found to be exceptionally active for many reactions including: Oxidation of carbon monoxide^{20,21}, hydrochlorination of ethyne using supported chlorides²¹, the epoxidation of propene²², and the synthesis of hydrogen peroxide²³.

Au catalysts on different supports were studied for the production of hydrogen peroxide using H₂ and O₂. Landon *et al.* studied the direct formation of hydrogen peroxide from H₂/O₂ using Au supported on Al₂O₃. The selectivity of H₂O₂ was determined to be 53%. The supported Au catalyst produces more H₂O₂ than the supported Pd catalyst. However, the supported alloy (1:1) produces even more H₂O₂ than the Au catalyst²⁴. This reduced selectivity is likely to be due to a side reaction of hydrogen and oxygen to produce water as shown in scheme 1.1.



Scheme 1.1: Reaction of hydrogen and oxygen to produce hydrogen peroxide

The same group then decided to expand the study to other supports. Edwards *et al.* studied the direct synthesis of hydrogen peroxide from H₂ and O₂ using a range of Au, Pd and Au–Pd metal nanoparticles supported on iron oxide²³. The choice of the support

was based on previous studies that showed the remarkable activity of Au/Fe₂O₃ for the oxidation of CO at ambient temperatures²⁵. The preparation of the catalysts was performed using two methods: impregnation and co-precipitation. Results showed that the best method of preparation for CO oxidation is co-precipitation whilst impregnation is the preferred method for H₂O₂ synthesis. For example, catalysts prepared by co-precipitation resulted in a 91-100% conversion rate of CO as opposed to <1% of CO conversion for catalysts prepared using impregnation. The productivity of hydrogen peroxide increases from 0.207 mol h⁻¹ kg_{cat}⁻¹ when using co-precipitation as a preparation method to 0.54 mol h⁻¹ kg_{cat}⁻¹ when using impregnation. In fact, there was an inverse relationship in that catalysts that were active for CO oxidation were inactive for H₂O₂ production and vice-versa.

For the Au catalysts made by impregnation, H₂O₂ was produced but at low rates. However, the addition of Pd to Au significantly enhanced the synthesis of H₂O₂. In fact, the 2.5% Au – 2.5% Pd catalyst showed 22% selectivity to H₂O₂ with a H₂ conversion of 71% at 2 °C both of which are higher than the Au-only and Pd-only catalyst²³.

The same study was then repeated for titania-supported Au, Pd, and Au–Pd catalysts²⁶. Once again, the best catalysts for H₂O₂ production were prepared using impregnation. Unlike on alumina-supported catalysts, higher production rates were observed for Pd. However, an optimum Pd-Au composition was observed for the alloy where the rate of H₂O₂ was even higher than the pure Pd catalyst. The 2.5 wt% Au – 2.5 wt% Pd/TiO₂ catalyst displayed the highest rates. Moreover, the rates of hydrogen peroxide formation for the titania-supported catalysts were found to be a factor of three higher than the corresponding alumina-supported catalysts indicating that the nature of the support has an important role on the oxidation process²⁶.

Soon after, the same group decided to explore the oxidation of primary alcohols to aldehydes using Au–Pd/TiO₂ catalysts. Since hydroperoxyl species are involved in the synthesis of hydrogen peroxide and since these are considered to be key intermediates in the oxidation of alcohols, it is highly likely these catalysts will be effective for the oxidation of alcohols. The Au–Pd/TiO₂ catalysts were found to be very active for the oxidation of benzyl alcohol at 373 K with O₂ as an oxidant in the absence of solvent. The reaction produced benzaldehyde with a selectivity of more than 96%. The Pd/TiO₂ catalyst on the other hand also produced toluene and benzene as by-products whilst the Au/TiO₂ catalyst also produced a significant amount of acetal product. The Al₂O₃ and the

Fe₂O₃ supports were also explored for this reaction but the titania-supported alloy catalyst was preferred for the oxidation of benzyl alcohol. This is due to the more acidic nature of the other two supports which leads to enhanced by-product formation²⁷.

Since the oxidation of benzyl alcohol to its aldehyde using Au–Pd alloy supported on titania proved successful. The same catalyst was investigated for the partial oxidation of methane to methanol using H₂O₂ as an oxidant²⁸. The preparation of the catalyst by sol immobilisation resulted in a high decomposition of the hydrogen peroxide oxidant. As a result, 1 wt % Au–Pd/TiO₂ of the catalyst was prepared by incipient wetness (IW) which resulted in an increase in the turnover frequency by a factor of two with 58% of the oxidant remaining after the reaction. The effect of the temperature on the catalytic activity was also examined with the reaction being run at various temperatures. As the temperature increased, there was an increase in the catalytic productivity with the maximum turnover frequency (ca. 25 h⁻¹) and selectivity (19%) achieved at the highest temperature (90 °C). However, at all temperatures, the major reaction product was methyl hydroperoxide.

Increasing the weight percent from 1 to 5, resulted in a higher methanol selectivity, but a similar overall oxygenate selectivity. However, the overall catalyst productivity was found to be lower due to the high decomposition of hydrogen peroxide.

The 5 wt% catalyst was then investigated at a lower temperature of 2 °C. Reducing the temperature resulted in 93% oxygenate selectivity (45% to methanol), low hydrogen peroxide decomposition (~ 90% left of the oxidant), and a similar rate to the experiments that were conducted at higher temperatures. Experiments performed using titania without Au or Pd did not result in any products indicating that the alloy is the active component of the catalyst. The time-on-line study of the reaction clearly indicates that the methyl hydroperoxide intermediate is the primary intermediate in the reaction. Electron paramagnetic resonance (EPR) studies were performed to study the nature of the oxidation. CH₃• and OH radicals were formed during the reaction indicating that the mechanism of the reaction proceeds via a radical pathway. The termination reaction of the two radicals can then form methanol. Alternatively, methyl radicals can also react with dissolved oxygen originating from hydrogen peroxide decomposition on the surface resulting in the formation of CH₃OO•.

Improved methanol selectivity was also observed when using *in situ* generated H₂O₂. The *in situ* reaction results in a three-fold increase in reactivity. As discussed earlier,

hydrogen peroxide can be produced using the catalyst at 2 °C, therefore methane oxidation was studied at this temperature as well. Once again, the results suggest the ability of the supported alloy to activate methane and produce methanol via a methyl hydroperoxide intermediate²⁸.

In order to rationalise how the alloy facilitates the partial oxidation of methane to methanol on supported oxides, Liu *et al.* studied the liquid phase oxidation of cyclohexane to cyclohexanol using Au–Pd/MgO catalysts²⁹. Previous work described the role of Au catalysts in the partial oxidation of cyclohexane³⁰. Conte *et al.* found that Au catalyses the reaction by increasing the concentration of the intermediate species which are considered to be chain carriers in the radical pathway of the reaction thus promoting catalytic autoxidation via a radical chain mechanism.

Industrially, the oxidation of cyclohexane to cyclohexanol is catalysed by the commercial cobalt naphthenate initiator³⁰(figure 1.2). The conversion of cyclohexane to cyclohexanol using 1 wt% Au–Pd/MgO exhibited a conversion of 11% with a total selectivity of 95% as opposed to the commercial catalyst which has a conversion rate of 9% with a selectivity of 85%. Monometallic Au/MgO and Pd/MgO displayed much lower catalytic performance indicating that neither Au nor Pd on their own are effective as catalysts for the reaction²⁹.

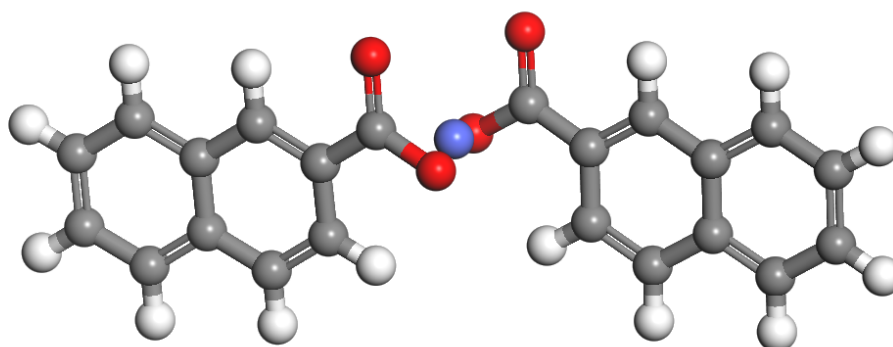


Figure 1.2: Structure of the commercial cobalt naphthenate initiator (Colour code: Grey: Carbon, White: Hydrogen, Red: Oxygen, Purple: Cobalt)

EPR-spin trapping experiments were then performed in order to study the mechanism of the reaction. The main radicals trapped that were identified were RO•, ROO•, and carbon radicals. The amount of RO• trapped for the 1 wt% Au/MgO, 1 wt% Pd/MgO, and 1 wt% Au–Pd/MgO was significantly higher than the Co-naphthenate initiator. Moreover, the most remarkable difference between the four catalysts is the fraction of

the alkoxy species vs the peroxy species. In the case of the alloy, the RO•/ROO• is almost twice that of the monometallic catalysts. The RO•/ROO• for Co-naphthenate, 1 wt% Au/MgO, 1 wt% Pd/MgO, 1 wt% Au–Pd/MgO was 0.9, 15.6, 12.8, and 30.3. This simple observation suggests that the MgO supported noble metal catalysts are capable of homo-cleavage of the O–O of the cyclohexyl hydroperoxide. The difference in ratio between the alloy and the monometallic catalysts suggests that the alloy has an intrinsically stronger chemical affinity for cyclohexyl hydroperoxide and its cleavage, which can be explained by examining the electronic structure at the surface of the Au–Pd alloy. Alloying Au and Pd may shift the electron density from Pd to Au atoms due to the higher electronegativity of Au. Hence, upon the adsorption of the cyclohexyl hydroperoxide on the alloyed surface, the difference in induced charge between the two metal components (Figure 1.3) will result in the cleavage of the O–O of the cyclohexyl hydroperoxide²⁹.

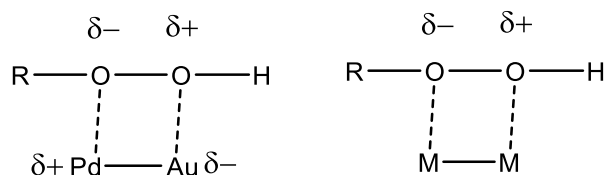
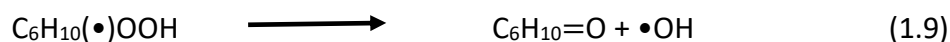
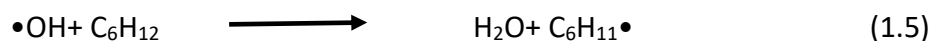
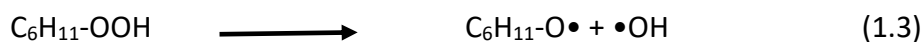


Figure 1.3: The adsorption of the hydroperoxide on the surface in the case of the alloy (left) and in the case of the monometallic catalyst(right)

Using results from the EPR-spin trapping experiments, the group proposes a reaction mechanism for the production of cyclohexanol and cyclohexanone starting with the cyclohexyl hydroperoxide intermediate (scheme 1.2)





Scheme 1.2: Reaction Mechanism for the production of cyclohexanol and cyclohexanone from cyclohexyl hydroperoxide

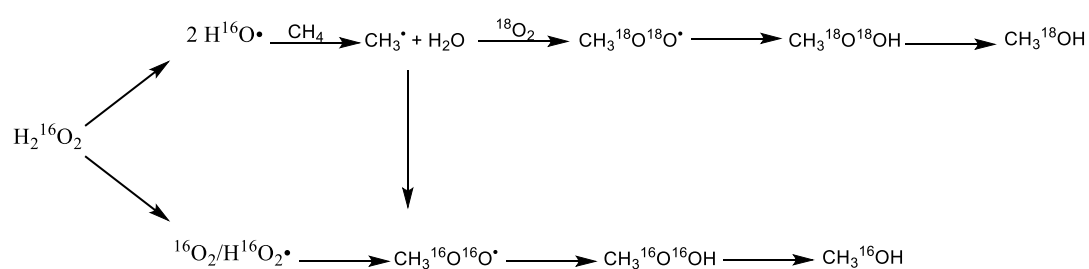
With all this in mind, Agarwal *et al.* studied the selective oxidation of methane to methanol using aqueous Au–Pd colloids using both H₂O₂ and O₂ as oxidants³¹. They prepared polyvinylpyrrolidone (PVP)– stabilized Au–Pd (1:1 molar ratio) colloids and supported catalysts by immobilising the colloid on titania. They then studied the oxidation of methane in water with H₂O₂ as an oxidant at 50°C and 30 bar of CH₄ for 30 minutes. With the supported colloid material catalyst (1% Au–Pd/TiO₂), minimal products were observed with a primary oxygenate selectivity of 26%. As observed in earlier studies²⁸, there was a high decomposition rate for H₂O₂ with 73% of the oxidant decomposing. This high rate of decomposition had a negative impact on the efficiency of the catalyst. As a result of the concentration of OH radicals being too high, the reactive radical chains in the reaction were immediately terminated. Moreover, the consumption of the oxidant at such a high rate did not allow sufficient interaction with methane.

The high decomposition of the oxidant was not observed in the presence of the bare support and the unsupported Au–Pd colloids. Only upon supporting the metal colloids on the titania support, did the catalyst exhibit such high decomposition of hydrogen peroxide, which could be either due to a change in the nanoparticle morphology upon immobilisation or the interfacial sites at the support/metal interface. In order to investigate this further, the partial oxidation of methane on unsupported PVP-stabilized Au–Pd colloids was studied. Using the same amount of metal as in the supported catalyst and a 1000 μmol of H₂O₂, substantially more product was observed with less H₂O₂ consumption than the supported catalyst. The colloidal catalyst was an order of magnitude more efficient than the titania supported colloids with a gain factor (which is defined as as mole of oxygenate produced per mol of hydrogen peroxide consumed) of 3×10^{-2} compared with 2×10^{-3} . Moreover, the primary products in the reaction (methanol and methyl hydroperoxide) were produced with 90% selectivity. The presence of CH₃OOH, CH₃OH, HCOOH, and CO₂ indicates the reaction proceeds via a consecutive oxidation pathway. The presence of methyl hydroperoxide as the primary product implies that the primary termination step is either a reaction between •CH₃ and •OOH or from recombination of •CH₃ with dissolved O₂ which was formed as a result of

H₂O₂ decomposition. Since in the case of the unsupported colloidal catalyst, the rate of the decomposition of hydrogen peroxide is low, they tested whether the addition of oxygen to the reaction mixture would result in an increase in the production the methyl hydroperoxyl radical. The addition of 5 bar of molecular oxygen resulted in an increased product yield when compared with the H₂O₂-only reaction. (26.8 μmol vs 15.7 μmol). The gain factor was also more than double that of the colloidal catalyst with H₂O₂, which suggests that the addition of molecular oxygen to the reaction mixture promotes the production of the primary intermediates in the reaction. In order to prove that the oxygen source present in the products is from molecular oxygen, isotope labelled oxygen was introduced into the reaction mixture. Mass spectrometry was then used to confirm the presence of CH₃O¹⁸O¹⁸H. The results confirmed that CH₃OH mass fragments containing the 18 O label were responsible for 51% of the observed signal.

The effect of decreasing the amount of hydrogen peroxide in the reaction mixture from 2000 to 1000 μmol over 60 minutes in the presence of 5 bar of molecular oxygen was next investigated. The results obtained displayed an increase in the products formed from 18 to 43 μmol with a reduced consumption of H₂O₂ from 81 to 64%. Halving the amount of hydrogen peroxide once again (from 1000 to 500 μmol) resulted in a further increase in the amount of primary oxygenate products (from 43 μmol to 50 μmol). Reducing the amount of H₂O₂ any further resulted in a decrease in the amount of product as a result in the reduction in the concentration of radicals generated. In order to demonstrate that the source of oxygen in the methyl hydroperoxide is indeed molecular oxygen, isotope labelled experiments were conducted by adding 5 bar of ¹⁸O₂ into the reaction mixture. Mass spectroscopy analysis of the primary products revealed that 51% of the observed signal corresponded to CH₃OH mass fragments containing ¹⁸O label. Reactions in the absence of hydrogen peroxide but in the presence of molecular oxygen showed no product formation indicating that the presence of hydrogen peroxide is crucial for the initiation step. A decrease in the concentration of hydrogen peroxide to levels as low as 500 μmol resulted in an increase in the reaction products from 43 to 50 μmol, which further supports the role played by hydrogen peroxide as only an initiator. Control experiments on the monometallic colloids using the same experimental conditions were also conducted. Pure Au and Pd showed no activity for methane oxidation further suggesting that the alloyed nanoparticles display a synergistic effect in term both stability and activity for the reaction.

Since the reaction only happens in the presence of hydrogen peroxide, it is highly likely the activation of methane will occur through a radical mechanism. The methyl radicals generated can then react with the dissolved oxygen resulting in the incorporation of more than 70% of molecular oxygen into the primary products. Products containing ^{16}O were also formed, which were, however, a result of the decomposition of the hydrogen peroxide into either $^{16}\text{O}^{16}\text{OH}$ or $^{16}\text{O}_2$. This study confirmed that once the C–H bond in methane is activated using hydrogen peroxide, it is then possible to use molecular oxygen in order to form the primary intermediate in this reaction: methyl hydroperoxide (scheme 1.3). This method of converting methane to methanol would make the entire process substantially cheaper and economically viable.



Scheme 1.3: Proposed reaction scheme of the partial oxidation of methane to methanol using hydrogen peroxide and oxygen as oxidants.

1.3.2 Transition metal doped graphene on Ni (111) surfaces

Within the catalytic community, two types of catalysts are extensively studied: Strong-Metal Support Interaction (SMSI)³² and Electron-Metal Support Interaction (EMSI)³³. Whilst both models involve a metal supported on a metal oxide support, the former results in a reduction or complete blockage of the metal activity whilst the latter results in a higher activity as a result of electronic perturbation by the metal oxide. However, the role of a metal as a support is less commonly studied³⁴. Recently a research group led by Andreas Heyden at the University of South Carolina studied the partial oxidation of methane to methanol on Rh-doped graphene supported on Ni(111) surfaces using molecular oxygen as an oxidant³⁴. The group proposed a novel Electronic Atomic Monolayer-metal Support Interaction (EAMSI) model which is capable of activating molecular oxygen upon adsorption allowing for the activation of methane via an Eley-Rideal reaction mechanism.

The group compared the reaction mechanism at 473 K on two different surfaces: (1) Rh-doped graphene supported on Ni (111) surface and (2) Rh-doped graphene. The reaction mechanism proposed by the group for the first model involves the adsorption of two molecular oxygen molecules on the Rh atom present on graphene. One of the oxygen molecules then abstracts a hydrogen atom from methane resulting in a Rh-C bond with the methyl group and the cleavage of the O-O bond leaving an O-H connected to the Rh atom. The hydrogen abstraction process has a barrier of 1.37 eV. The formation of the first methanol group then occurs rapidly with a barrier of 0.09 eV. The oxygen atom left on the surface then reacts with another methane molecule with a free energy barrier of 0.96 eV. The catalytic cycle is then closed upon the desorption of the second methanol molecule. The group described this mechanism as an Eley-Rideal as the methane molecule is only physisorbed at the Rh active centre with pre-adsorbed oxygen molecules.

The proposed reaction mechanism for the second model (Rh-doped graphene) proceeds in a similar fashion but involves the adsorption of only one molecule of oxygen. The energy barrier of the hydrogen abstraction for the free-standing graphene-Rh model was found to be significantly higher with an energy barrier of 2.02 eV. This noticed difference highlighted the importance of the Ni (111) support.

Since Cu-containing zeolites have shown remarkable activity for this reaction, the group then decided to study Cu-doped graphene supported on a Ni (111) surface. The energy barrier for the first C–H bond cleavage was found to be significantly higher with a value of 1.62 eV. This 0.25 eV difference between the two catalysts suggests a lower reaction rate of about 460 times at 473 K. As a result, the Cu-doped graphene on Ni was classified as not a good catalyst for the reaction.

The interaction between the Rh-doped graphene and the Ni (111) surface were described as electronic atomic monolayer metal support interaction (EAMSI). The general nature of EAMSI was explored further by the group by comparing the adsorption of CO, C₂H₄, and OH on Cu-, Fe-, Ir-, Mn-, and Rh-doped graphene on Ni (111) and the free-standing structures. In all cases, the adsorption energy was stronger on the catalysts that were supported on the Ni (111) surface. This suggests that the presence of a metal support can stabilise the adsorption energy of small molecules by forming covalent bonds with the transition metal doped atomic monolayer. Therefore, it is possible to alter the catalytic properties of single atom catalysts through the EAMSI model.

1.4 Iron- and Copper- containing Zeolites

Throughout the 20th century, most of the research present in this field focused on metal oxide catalysts such as vanadium and molybdenum for the partial oxidation of methane to methanol³⁵. However, there was a shift in research focus at the beginning of the 21st century from metal oxide catalysts to iron- and copper-containing zeolites such as ZSM-5 and mordenite. The change in research focus was based on the findings that these zeolites stabilise binuclear iron and copper centres in a way analogous to enzymes found in nature such as monooxygenase (MMO) enzymes⁹. These enzymes selectively convert methane into methanol at ambient temperatures³⁶.

Researchers at Cardiff University studied the efficiency of iron- and copper-containing zeolites as catalysts in the selective oxidation of methane to methanol in an aqueous medium using hydrogen peroxide as an oxidant³⁷. Initially they started by examining the activity of different zeolites such as ZSM-5, Ferrierite, Beta, Silicalite-1, and TS-1 on the selective oxidation of methane. Out of the five catalysts, the ZSM-5 zeolite exhibited remarkable activity when compared with other zeolites whilst the silicalite-1 zeolite exhibited no activity at all. Since the major difference between the two zeolites was the aluminium content, it was therefore interesting to study whether aluminium was the source of activity in the zeolite. Hammond *et al.* started by tuning the aluminium content in the ZSM-5 zeolite through post-synthesis or hydrothermal methods. The results obtained showed that the difference in aluminium content led to negligible changes in the activity concluding that Al was not the active component of the catalyst. Elemental analysis was then performed in order to determine the role played by any metal species within the zeolite. The analysis revealed trace amounts of Fe in all the zeolites except TS-1 which showed almost no activity. The amount of Fe present in the silicalite-1 was significantly lower than the other zeolites but upon introducing Fe alone into the silicalite-1 matrix, a significant increase in the activity of the catalyst was observed. These experiments proved that the presence of Fe within the MF1 material is crucial for the activity of the catalysts.

The Fe species within the Fe- silicalite-1 was then investigated in order to determine the relationship between the catalyst structure and activity. Transmission electron microscopy demonstrated the absence of Fe species on the external surface of the catalyst. Therefore, the presence of the Fe species within the zeolite micropores was

then studied using FT-IR and UV/Vis spectroscopy. The spectra obtained displayed a band at 710-700 cm^{-1} indicating the incorporation of Fe species into the tetrahedral framework sites. However, these bands disappeared upon template removal and calcination which suggests the migration of the Fe ions from the framework into the extra-framework positions. With the aid of other spectroscopic techniques, it was then concluded that there is a direct relationship between the catalytic activity and the concentration of iron in the extra-framework sites.

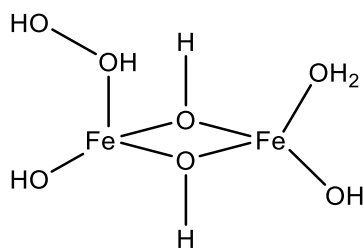


Figure 1.4: Structure of the diiron complex

Several models for the diiron complex were investigated using both EXAFS and theoretical modelling. The diiron complex that was the closest match between the two is shown in figure 1.4. The active iron site was identified as being an extra-framework binuclear core that forms a Fe-OOH intermediate upon activation with hydrogen peroxide. This species is capable of activating the carbon-hydrogen bond forming methyl hydroperoxide as the primary intermediate. The hydroperoxide may then undergo a second surface catalysed conversion to methanol through the hydrolysis of a surface bound methoxy species. This process will generate hydroxyl radicals which are responsible for the over-oxidation of methanol to formic acid. The addition of Cu^{2+} ions to the reaction was found to drastically decrease the concentration of hydroxyl radicals reducing the possibility of over-oxidation. Therefore, even though the copper is not responsible for an increase in catalytic activity, it acts as a modulator which ensures high methanol selectivity.

The reaction mechanism proposed by the group is shown in figure 1.5. Density Functional theory (DFT) calculations were run using the Vienna Ab initio Simulation Package (VASP) in order to study the mechanism of the reaction. Transition state calculations were run from species 4 to species 5 in order to determine the barrier for hydrogen abstraction from methane to form methyl hydroperoxide. The barrier determined computationally was found to be 50 kJ mol^{-1} which is in good agreement with the activation energy determined experimentally (61 kJ mol^{-1}).

EPR spectroscopy was used to confirm the validity of the model described in figure 4. The EPR spectra obtained confirmed the absence of methyl radicals indicating that the reaction does indeed go through methyl hydroperoxide as the primary intermediate. Upon its generation, the methyl hydroperoxide desorbs into the solution thereby closing the catalytic cycle^{37 38}.

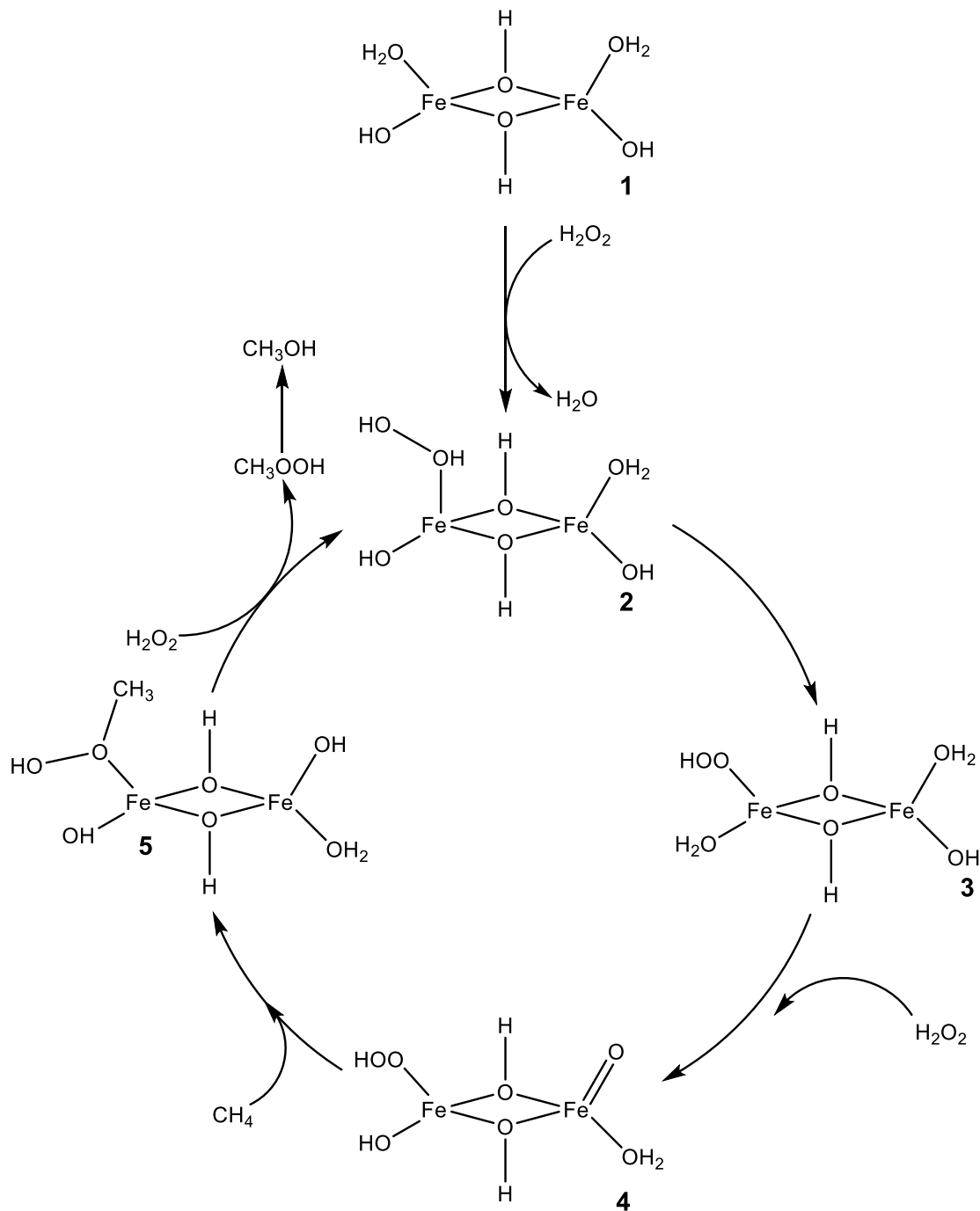


Figure 1.5: Proposed catalytic cycle for the oxidation of methane to methanol catalysed by a binuclear Fe species in ZSM-5³⁷.

Besides altering the catalyst used in this reaction, researchers have also been interested in using different oxidants as the reaction with peroxides usually involve a radical mechanism and hence has poor selectivity³⁹. As a result, other oxidants for this reaction have also been studied by other computational groups.

Another major oxidant that is normally studied for this reaction is nitrous oxide. Work performed by Mehmet Fella and Isik Onal at the Middle East Technical University in Turkey studied the direct methane to methanol oxidation on Fe- and Co-ZSM-5 clusters using N₂O as an oxidant.⁴⁰ The group used DFT as implemented in the Gaussian program to identify the mechanistic steps via which this reaction occurs. The effect of water on methanol formation was also studied.

The ZSM-5 was modelled as a cluster ((SiH₃)₄AlO₄M) where M is either Fe or Cu. The reaction mechanism proposed by the group involves the decomposition of the N₂O molecule forming an α-oxygen on Fe/Cu-ZSM-5 cluster. The second and the third step involve the abstraction of hydrogen from methane followed by the formation of a hydroxy complex (figure 1.6). The energy barrier for the hydrogen abstraction step on Fe-ZSM-5 and Cu-ZSM-5 was found to be 16 and 15 kcal mol⁻¹ respectively.

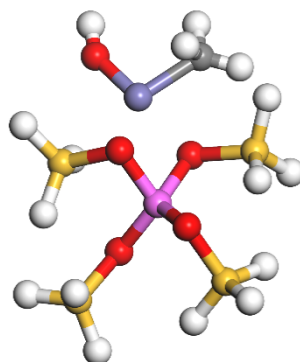


Figure 1.6: Equilibrium final geometry for C–H activation of methane and hydroxy complex formation. (Pink: Al, Yellow: Si, Red: O, Grey: C, Lilac: Fe/Cu, White: H)

Even though the activation barrier for the hydrogen abstraction step was relatively low, the methanol formation step had barriers that were significantly higher. The methanol formation step was found to be the rate determining step with activation barriers of 49 and 53 kcal mol⁻¹ for Co-ZSM-5 and Fe-ZSM-5 respectively.

The effect of water on the reaction was then studied by the group as it has been reported by Bell *et al.* that introducing water into the reaction increases methanol formation.⁴¹ The group studied the adsorption of water onto the cluster shown in figure 3. The pathway of the reaction proposed by the group is shown in equations 1.11-1.14.



The activation barriers for the methanol formation with water were then determined. The transition state barrier values were found to be 39 and 48 kcal mol⁻¹ for Co-ZSM-5 and Fe-ZSM-5 respectively. This theoretical study was one of the first to compare the reaction mechanism of methane oxidation on Co and Fe using N₂O as an oxidant. It highlighted the effect of water addition to both the reaction mechanism and the transition state barriers.

Chapter 2 Theoretical Background

2.1 The Schrödinger Equation

Classical mechanics, also known as Newtonian mechanics, aims to determine the position of a particle $x(t)$ at any given time (t). This is normally achieved by expressing Newton's second law of motion in terms of the potential energy, position, and time as shown in equation 2.1.

$$m \frac{d^2x}{dt^2} = -\frac{\partial V}{\partial x} \quad (2.1)$$

Quantum mechanics solves the same problem but using a different approach. Instead of defining the position of a particle with respect to $x(t)$, it defines it using the wave function $\Psi(x, t)$ ⁴². In order to understand the meaning of the wave function, we will start by describing the wave equation for the motion of a vibrating string.

Consider a uniform string fixed at two positions: 0 , and l as shown in figure 1. The maximum displacement of the string from its equilibrium position is defined as its amplitude $u(x, t)$.

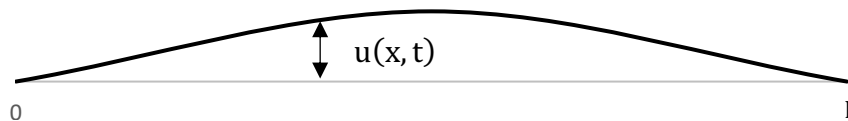


Figure 2: The amplitude of a vibrating string $u(x, t)$.

Thus, using classical mechanics, one can describe the amplitude of the vibration string $u(x, t)$ in terms of the speed v with which a disturbance moves along the string as shown in equation 2.2.

$$\frac{d^2u(x, t)}{dx^2} = \frac{1}{v^2} \frac{d^2u(x, t)}{dt^2} \quad (2.2)$$

Equation 2.2 is known as the classical wave equation and can be solved by a method known as the separation of variables. This method relies on the assumption that the variable $u(x, t)$ can be separated into a function of x ($X(x)$) multiplied by a function of t ($T(t)$) as shown in equation 2.3.

$$u(x, t) = X(x) T(t) \quad (2.3)$$

Substituting equation 2.3 into 2.2 and dividing by $u(x, t)$ results in equation 2.4 which is a function of x only on the left-hand side and a function of t only on the right-hand side.

$$\frac{1}{X(x)} \frac{d^2 X(x)}{dx^2} = \frac{1}{v^2 T(t)} \frac{d^2 T(t)}{dt^2} \quad (2.4)$$

Since $u(x, t)$ is considered to be the amplitude of the wave, it can be expressed in terms of $\psi(x)$ and $\cos(\omega t)$ as shown in equation 2.5.

$$u(x, t) = \psi(x) \cos(\omega t) \quad (2.5)$$

where $\psi(x)$ is called the spatial amplitude of the wave.

Substituting equation 2.5 into equation 2.2 and knowing that $\omega = 2\pi v$ and that $v\lambda = v$ results in an equation for the spatial amplitude $\psi(x)$:

$$\frac{d^2 \psi(x)}{dx^2} + \frac{4\pi^2}{\lambda^2} \psi(x) = 0 \quad (2.6)$$

Introducing de Broglie's equation⁴³ for the total energy of a particle as the sum of its kinetic energy and potential energy:

$$E = \frac{p^2}{2m} + V(x) \Rightarrow p = \{2m[E - V(x)]\}^{1/2} \quad (2.7)$$

$$\lambda = \frac{h}{p} = \frac{h}{\{2m[E - V(x)]\}^{1/2}} \quad (2.8)$$

Substituting equation 2.8 into equation 2.6 results in the famous Schrodinger equation⁴⁴ as shown in equation 2.9.

$$\frac{d^2 \psi}{dx^2} + \frac{2m}{\hbar^2} [E - V(x)] \psi(x) \quad (2.9)$$

where \hbar is Planck's constant (h) divided by 2π .

Equation 2.9 is often rewritten in the form shown in equation 2.10:

$$-\frac{\hbar^2}{2m} \frac{\partial^2 \psi}{\partial x^2} + V(x) \psi(x) = E \psi(x) \quad (2.10)$$

Or simply:

$$\hat{H} \psi(x) = E \psi(x) \quad (2.11)$$

where \hat{H} is defined as the Hamiltonian Operator and corresponds to the summation of the kinetic energy and the potential energy $(-\frac{\hbar^2}{2m} \frac{\partial^2}{\partial x^2} + V(x))$ ⁴².

2.2 Electron Density

Whilst the Schrödinger Equation for one electron systems can be easily solved, this is not often the case for multi-electron systems. The interaction of the electrons in multi-electron systems can lead to equations that are challenging to solve algebraically and thus require the use of numerical methods to approximate the energy of the system. As a result, several methods with varying degrees of accuracy and efficiency have been developed in order to approximate the solution of the Schrödinger Equation. These include: Hartree-Fock (HF), Møller-Plesset (MP) perturbation theory, and Density Functional Theory (DFT)⁴⁵.

The problem with methods such as Hartree-Fock and MP perturbation theory is that they rely on the wave function as the central quantity. The wavefunction is a very complicated quantity as it cannot be determined experimentally and relies on $4N$ variables (three spatial and one spin) for each of the N electrons within a system. Since the systems of interest in natural sciences consist of many electrons, any method that relies on determining the wavefunction in order to solve the Schrödinger equation will quickly become impractical⁴⁵.

Density Functional Theory aims to get around this problem by using the electron density $\rho(\vec{r})$ in order to reach a close approximation to the solution of the Schrödinger equation for a specific system. Unlike the wavefunction, the electron density can be determined experimentally (X-ray diffraction) and depends only on three spatial variables and is therefore an object in the three-dimensional space. The electron density is defined as a multiple integral over the spin coordinates of all electrons and over all but one of the spatial variables:

$$\rho(\vec{r}) = N \int \dots \int \psi(\mathbf{r}, x_2, \dots, x_N) \psi(\mathbf{r}, x_2, \dots, x_N) dx_2 \dots dx_N \quad (2.12)$$

Integrating the electron density over all space results in the total number of electrons as shown in equation 2.13.

$$\int \rho(\vec{r}) dr = N \quad (2.13)$$

The first attempt to use the electron density in order to compute the energy of a system dates back to the work of Thomas and Fermi⁴⁶ in 1927. In their model, Thomas and Fermi

express the kinetic energy for the uniform electron gas system; the jellium model, where the electron density is constant throughout the system. This combined with the classical expression for the electron-electron repulsive potential along with the nucleus-electron attraction potential results in the famous Thomas-Fermi equation (2.14) ⁴⁵.

$$E_{TF}[\rho(\vec{r})] = \frac{3}{10} ((3\pi)^2)^{2/3} \int \rho^{5/3}(\vec{r}) d\vec{r} - Z \int \frac{\rho(\vec{r})}{r} d\vec{r} + \frac{1}{2} \iint \frac{\rho(\vec{r}_1)\rho(\vec{r}_2)}{r_{12}} d\vec{r}_1 d\vec{r}_2 \quad (2.14)$$

2.3 Density Functional Theory

2.3.1 Hohenberg-Kohn Theorems

Almost 40 years after Thomas and Fermi first used the electron density to express the energy of a system, Density Functional Theory was born. In 1964, Hohenberg and Kohn⁴⁷ published a paper that proved that the electron density can indeed be used to determine the Hamiltonian operator thus allowing us to compute the energy of a system. The energy can be calculated as the sum of the kinetic energy ($T[\rho(r)]$) and the potential energies. The latter of which consists of the potential energy between the electrons and the electrons and the nuclei as shown in equation 2.15⁴⁵.

$$E[\rho(r)] = T[\rho(r)] + E_{ee}[\rho(r)] + E_{eN}[\rho(r)] \quad (2.15)$$

We can express the potential energy due to the nuclei-electron attraction in terms of the electron density where $E_{eN}[\rho(r)] = \int \rho(r) V_{eN} dr$; thus, equation 2.15 becomes:

$$E[\rho(r)] = T[\rho(r)] + E_{ee}[\rho(r)] + \int \rho(r) V_{eN} dr \quad (2.16)$$

The summation of the kinetic energy and the potential energy of the repulsion between the electrons is often referred to as the *Hohenberg-Kohn* functional $F_{HK}[\rho]$. Unfortunately, as its explicit form is unknown, this functional is often referred to as the holy grail of DFT⁴⁵. All we can do is extract the classical Coulomb interactions of the electron density $J[\rho]$ shown in equation 2.14.

$$E_{ee}[\rho] = \frac{1}{2} \iint \frac{\rho(\vec{r}_1)\rho(\vec{r}_2)}{r_{12}} d\vec{r}_1 d\vec{r}_2 + E_{ncl}[\rho] = J[\rho] + E_{ncl}[\rho] \quad (2.17)$$

$E_{ncl}[\rho]$ is the non-classical contribution to the electron-electron interaction containing the effects of self-interaction correction, and exchange and Coulomb correlation.

A variational principal similar to the one used for wave functions was also tackled using the Second *Hohenberg-Kohn* Theorem. The theorem states that for any electron density ρ' , the energy $E[\rho'(r)]$ cannot be less than the real ground state energy E_0 :

$$E[\rho'(r)] \geq E_0 \quad (2.18)$$

2.3.2 Kohn-Sham Approach

A year after the remarkable discovery of the *Hohenberg-Kohn* theorems, Kohn and Sham published a paper⁴⁸ which detailed an approach to the approximation of the kinetic energy term present in equation 2.16. In order to compute a major fraction of the kinetic energy, Kohn and Sham treated their system as a system of non-interacting fermions with a Hamiltonian in which an effective local potential $V_s(\vec{r})$ has been introduced as shown in equation 2.19. Thus, by choosing an effective potential V_s , we can alter the value of \hat{H}_S such that the summation of the moduli of the square of the orbitals equals the ground state density of the real system of interacting electrons.

$$\hat{H}_S = -\frac{1}{2} \sum_i^N \nabla_i^2 + \sum_i^N V_s(\vec{r}) \quad (2.19)$$

Since the Hamiltonian in equation 2.19 does not contain any electron-electron interactions, its ground state wave function can be represented by a Slater determinant similar to the one used in HF theory. Where the spin orbitals, φ_i , are given by:

$$\hat{f}^{KS} \varphi_i = \varepsilon_i \varphi_i \quad (2.20)$$

where \hat{f}^{KS} is known as the one-electron Kohn-Sham operator and is defined as:

$$\hat{f}^{KS} \varphi_i = -\frac{1}{2} \nabla^2 + V_s(\vec{r}) \quad (2.21)$$

In order to express the universal functional as accurately as possible, Kohn and Sham decided to use the kinetic energy expression for the non-interacting fermions in order to approximate the kinetic energy component of the functional. Thus, the revised universal functional $F[\rho(\vec{r})]$ becomes

$$F[\rho(\vec{r})] = T_S[\rho(\vec{r})] + J[\rho(\vec{r})] + E_{XC}[\rho(\vec{r})] \quad (2.22)$$

where $T_S[\rho(\vec{r})]$ is defined as the kinetic energy of a fictitious system of N *non-interacting* electrons. E_{XC} is defined as the exchange-correlation energy and is expressed as:

$$E_{XC}[\rho] = (T[\rho] - T_S[\rho]) + (E_{ee}[\rho] - J[\rho]) = T_C[\rho] + E_{ncl}[\rho] \quad (2.23)$$

Thus, the residual part of the true kinetic energy is expressed as $T_C[\rho]$ and is simply added to the non-classical electrostatic contributions $E_{ncl}[\rho]$.

The energy of our interacting real system can thus be expressed as shown in equation 2.24.

$$\begin{aligned}
E[\rho(\vec{r})] &= T_S[\rho] + J[\rho] + E_{XC}[\rho] + E_{Ne}[\rho] \quad (2.24) \\
&= T_S[\rho] + \frac{1}{2} \iint \frac{\rho(\vec{r}_1)\rho(\vec{r}_2)}{r_{12}} d\vec{r}_1 d\vec{r}_2 + E_{XC}[\rho] + \int \rho(r) V_{Ne} dr \\
&= -\frac{1}{2} \sum_i^N \langle \varphi_i | \nabla^2 | \varphi_i \rangle + \frac{1}{2} \sum_i^N \sum_j^N \iint |\varphi_i(\vec{r}_1)|^2 \frac{1}{r_{12}} |\varphi_j(\vec{r}_2)|^2 d\vec{r}_1 d\vec{r}_2 \\
&\quad - \sum_i^N \int \sum_A^M \frac{Z_A}{r_{1A}} |\varphi_i(\vec{r}_1)|^2 d\vec{r}_1 + E_{XC}[\rho]
\end{aligned}$$

where N and M represent the number of electrons and nuclei respectively.

Using the variational principal, we can determine the condition that the orbitals φ_i must fulfil to minimise the energy. This leads to equation 2.25.

$$\begin{aligned}
\left(-\frac{1}{2} \nabla^2 + \left[\int \frac{\rho(\vec{r}_2)}{r_{12}} d\vec{r}_2 \right] - \sum_A^M \frac{Z_A}{r_{1A}} + V_{XC}(\vec{r}_1) \right) \varphi_i \quad (2.25) \\
= \left(-\frac{1}{2} \nabla^2 + V_{eff}(\vec{r}_1) \right) \varphi_i = \varepsilon_i \varphi_i
\end{aligned}$$

V_{XC} is the potential due to the exchange-correlation energy E_{XC} which cannot be explicitly expressed. It is evident that equation 2.25 resembles the one-particle equation from the non-interacting reference system (equation 2.20).

$$V_S \equiv V_{eff} = \left[\int \frac{\rho(\vec{r}_2)}{r_{12}} d\vec{r}_2 \right] - \sum_A^M \frac{Z_A}{r_{1A}} + V_{XC}(\vec{r}_1) \quad (2.26)$$

Thus, V_{XC} is expressed as the functional derivative of E_{XC} with respect to the electron density as shown in equation 2.27.

$$V_{XC}(\vec{r}_1) = \frac{\delta E_{XC}[\rho]}{\delta \rho} \quad (2.27)$$

2.3.3 Approximations of the Exchange-Correlation Functional

As explained in the earlier section, the exact format of the exchange-correlation functional is unknown and thus needs to be approximated. Several approximations for the E_{XC} functional have been made with the simplest being the Local Density Approximation (LDA)⁴⁵. The LDA model uses the uniform electron gas model in order to approximate the exchange-correlation functional. The model is based on the assumption that the E_{XC} functional can be expressed as:

$$E_{XC}^{LDA}[\rho] = \int \rho(\vec{r}) \varepsilon_{XC}(\rho(\vec{r})) d\vec{r} \quad (2.28)$$

where $\varepsilon_{XC}(\rho(\vec{r}))$ is the exchange-correlation energy per particle of a uniform electron gas of density $\rho(\vec{r})$. The quantity $\varepsilon_{XC}(\rho(\vec{r}))$ can then be split into its respective exchange and correlation contributions as shown in equation 2.29.

$$\varepsilon_{XC}(\rho(\vec{r})) = \varepsilon_X(\rho(\vec{r})) + \varepsilon_C(\rho(\vec{r})) \quad (2.29)$$

The exchange component $\varepsilon_X(\rho(\vec{r}))$ of equation 2.29 represents the exchange energy of an electron in a uniform electron gas and has been determined by Slater in his approximation of HF theory as shown in equation 2.30. This, however, is not the case for the correlation part $\varepsilon_C(\rho(\vec{r}))$ of equation 2.29.

$$\varepsilon_X = -\frac{3}{4} \sqrt{\frac{3\rho(\vec{r})}{\pi}} \quad (2.30)$$

Based on highly accurate Monte-Carlo simulations performed by Ceperly and Alder⁴⁹ in 1980 for the homogenous electron gas, several representations for the $\varepsilon_C(\rho(\vec{r}))$ have been explored. The most recent and accurate representation of the correlation energy was developed by Perdew and Wang in 1992⁵⁰.

The moderate accuracy of LDA is certainly insufficient for most of the applications in chemistry and thus until the birth of the Generalised Gradient Approximation (GGA), the use of LDA was mostly employed by theoretical and solid-state physicists. The Generalised Gradient Approximation does not only rely on the density $\rho(\vec{r})$ at a particular point (\vec{r}) but also uses information about the gradient of the charge density $\nabla\rho(\vec{r})$ in order to consider the non-homogeneity of the true electron density⁴⁵. Thus, GGA uses the local density approximation as the firm term of a Taylor expansion of the

uniform density and extends the series with the next lowest term in order to better approximate the E_{XC} functional:

$$E_{XC}^{GGA}[\rho(\vec{r})] = \int \rho(\vec{r}) \varepsilon_{XC} \rho(\vec{r}) d\vec{r} + \int F_{XC}[\rho(\vec{r}), |\nabla\rho(\vec{r})|] \quad (2.31)$$

The exact function $F_{XC}[\rho(\vec{r}), |\nabla\rho(\vec{r})|]$ varies for every functional and is determined by parameters based on experimental observations over a set of molecules.

One of the most popular GGA functionals is the PBE functional developed by Perdew, Burke, and Ernzerhof in 1996⁵¹. The work in this thesis uses the PBE functional as implemented within the VASP software. Previous work has shown that the use of the PBE functional to study the interaction of organic compounds on transition metal surfaces to be a good representative of adsorption energies and transition states^{52,53,}

54,55.

2.4 Plane Wave Basis Functions

Since the work in this thesis is concerned with modelling periodic extended surfaces, Plane Wave Basis Functions are used instead of ordinary basis sets that are constructed from atomic orbitals. The outer valence electrons in metals such as Au and Pd tend to behave like free electrons and thus the idea of using the solutions for the free electron as basis functions emerged⁵⁶. The solutions to the free electron in one-dimension Schrödinger equation is often expressed in terms of complex exponential functions as shown in equations 2.32.

$$\begin{aligned}\phi(x) &= Ae^{ikx} + Be^{-ikx} \\ \phi(x) &= A\cos(kx) + B\sin(kx)\end{aligned}\tag{2.32}$$

$$E = \frac{\hbar^2}{2m} k^2$$

where A and B are constants and x is the position of the electron.

In infinite systems, the energy spacing between distinct energy levels vanishes and thus the molecular orbitals merge into bands. The electrons within these bands can be described by orbitals expanded in a basis set of plane waves.

In order to fully understand plane wave basis functions, Bloch's theorem needs to be introduced. In solid structures such as metals and ionic compounds, the system of interest is translationally invariant in all three spatial directions. Bloch's theorem uses this translational symmetry in order to accurately express the wave function for infinite systems. Bloch's theorem therefore states that, for a given wave function $\psi(\mathbf{k}, \mathbf{r})$ that fulfils the Schrödinger equation, there exists a vector \mathbf{k} such that translation by a lattice vector \mathbf{T} is equivalent to multiplication by a phase factor⁵⁶:

$$\psi(\mathbf{k}, \mathbf{r} + \mathbf{T}) = e^{i\mathbf{k}\mathbf{T}} \psi(\mathbf{k}, \mathbf{r})\tag{2.33}$$

The wave vector \mathbf{k} in equation 2.33 must have the dimension of an inverse length and thus belongs to the reciprocal space. In order to understand the meaning of the reciprocal space, we will start by introducing a real space vector \mathbf{R} which is made of a linear combination of three basic vectors \mathbf{a}_1 , \mathbf{a}_2 , and \mathbf{a}_3 ⁵⁷:

$$\mathbf{R} = n_1\mathbf{a}_1 + n_2\mathbf{a}_2 + n_3\mathbf{a}_3 = \mathbf{a}\tag{2.34}$$

Similarly, the reciprocal lattice vector \mathbf{k} is made of a linear combination of three reciprocal basis vectors $\mathbf{g}_1, \mathbf{g}_2, \text{ and } \mathbf{g}_3$:

$$\mathbf{k} = m_1\mathbf{g}_1 + m_2\mathbf{g}_2 + m_3\mathbf{g}_3 = \mathbf{g} \quad (2.35)$$

The two space vectors are related by orthogonality relations as shown in equation 2.36.

$$\begin{aligned} \mathbf{g}_1 &= \frac{2\pi}{V} (\mathbf{a}_2 \times \mathbf{a}_3) \perp \mathbf{a}_2, \mathbf{a}_3 \\ \mathbf{g}_2 &= \frac{2\pi}{V} (\mathbf{a}_3 \times \mathbf{a}_1) \perp \mathbf{a}_1, \mathbf{a}_3 \\ \mathbf{g}_3 &= \frac{2\pi}{V} (\mathbf{a}_1 \times \mathbf{a}_2) \perp \mathbf{a}_1, \mathbf{a}_2 \end{aligned} \quad (2.36)$$

where the volume $V = \mathbf{a}_1 \cdot (\mathbf{a}_2 \times \mathbf{a}_3)$

This means that for each vector in reciprocal space, there are multiple planes in real space to which that vector is perpendicular. Therefore, instead of defining a lattice plane in real space, it would be easier to define it in reciprocal space. This is where Miller Indices come into action: The Miller indices $\{h, k, l\}$ of a lattice plane are defined as the coordinates of the shortest reciprocal lattice vector normal to that plane and thus are proportional to the inverses of the intercepts of the plane⁵⁷:

$$h = \frac{1}{x}; k = \frac{1}{y}; l = \frac{1}{z} \quad (2.36)$$

Therefore, having a miller index of zero means that there is no intersection point with the lattice vector i.e. the intercept is at infinity.

2.5 Pseudopotentials

In order to express all the electrons in a system using plane waves, enormous basis set sizes are required which would drastically increase computational cost. In order to solve this problem, pseudopotentials are used. Since in many of the chemical and physical processes, valence electrons are the ones that are directly involved, the core electron states are assumed to be fixed. This means that a pseudopotential can be constructed in order to account for the interactions between the nucleus and the core electrons. The valence orbitals are substituted by nodeless pseudo-wavefunctions which in turn reduces the basis set size required⁵⁶.

This approach does not just decrease computational cost but also takes care of the rapid oscillations of the atomic wave functions around the nucleus. The only disadvantage of this however is that since the local environment around the nucleus is not properly expressed, important information such as electric field gradients or hyperfine parameters is not accessible to the user⁵⁸.

In order to model the core electrons, the pseudopotentials are characterised by a core radius r_c . Depending on the size of r_c , the pseudopotential will require a certain number of plane wave basis functions i.e. a small r_c (“hard” pseudopotential) requires more plane wave basis sets than a large r_c (“small” pseudopotential). Therefore, a compromise between the size of the pseudopotential and the accuracy of the calculated results need to be met; while keeping in mind that having an r_c that is too large will affect the quality of the calculated results.

The pseudopotentials for distances less than r_c are determined using analytical functions, typically a polynomial, with the condition that the pseudo wavefunctions along with its first and second derivatives must match the reference wavefunction at r_c . In 1979, Hamann, Schlüter, and Ching⁵⁹ proposed a set of norm-conserving pseudopotentials that not only require the previously mentioned criterion but that also that the integral of the square of the pseudo wave and the reference from 0 to r_c must agree. This was a problem for 3d transition metals as it required hard pseudopotentials with a large energy cut off for the planewaves⁵⁶. Thus, Vanderbilt proposed to relax this requirement by introducing the so-called *ultrasoft pseudopotentials*⁶⁰.

The pseudopotentials used in this thesis are known as the Project Augmented Wave (PAW) pseudopotentials. The PAW valence wavefunction is expressed as a valence term

expanded into a plane wave basis set with a contribution from the core region of every nucleus. Near the nucleus, partial waves, similar to atomic orbitals, are added and subtracted to the plane wave part in order to feature the nodal structure of the true wavefunctions⁵⁸. Thus, the PAW potentials are more accurate than the ultrasoft potentials for two reasons:

- (i) The cutoff radii used in the PAW potentials are smaller (“harder”) than the ultrasoft potentials.
- (ii) The PAW method incorporates the nodes present in the core region in its valence wavefunction.

2.6 Vibrational Frequency Calculations

In order to understand how vibrational frequency calculations are performed using DFT, we will start by examining the vibrations of a diatomic molecule (AB)⁶¹. The energy for the stretching of a chemical bond between A and B is given by the Taylor expansion:

$$E = E_0 + (b - b_0) \left[\frac{dE}{db} \right]_{b=b_0} + \frac{1}{2} (b - b_0)^2 \left[\frac{d^2E}{db^2} \right]_{b=b_0} + \dots \quad (2.37)$$

where b is defined as the difference between the position of the two atoms A and B and b_0 is the equilibrium bond length.

The first derivative term is zero as the expansion is evaluated at the energy minimum and thus for small displacements about the equilibrium bond length, the energy of the system is defined as:

$$E = E_0 + \frac{\alpha}{2(b - b_0)^2} \quad (2.38)$$

where α is defined as the second derivative of the energy with respect to b ; $\left[\frac{d^2E}{db^2} \right]_{b=b_0}$.

Equation 2.38 is known as the harmonic approximation. By treating the nuclei of A and B as particles, we can use Newton's second law of motion in order to model the motion for the overall bond length:

$$\frac{d^2b(t)}{dt^2} = -\alpha \left(\frac{m_A + m_B}{m_A m_B} \right) (b(t) - b_0) \quad (2.39)$$

Equation 2.39 is a second order differentiable equation which can be solved by the method of separation of variables. The solution to the equation is:

$$b(t) = b_0 + a \cos \omega t \quad (2.40)$$

where a is an arbitrary constant and $\omega = \sqrt{\alpha \frac{m_A + m_B}{m_A m_B}}$

The vibrational frequency is related to ω in the following fashion:

$$\nu = \frac{\omega}{2\pi} = \frac{1}{2\pi} \sqrt{\alpha \frac{m_A + m_B}{m_A m_B}} \quad (2.41)$$

Most of the calculations of interest in DFT are not just made of a simple diatomic molecule but rather of multiple atoms that are interacting with a support or a surface.

Thus, we would need to expand the above derivation of the frequency to a set of N atoms.

Let's start by defining a set of N atoms where the cartesian coordinates of each atom is expressed as a single vector with $3N$ components, $\mathbf{r} = (r_1, \dots, r_{3N})$. Assuming the local minimum energy is found at r_0 , then the new coordinates can be defined with respect to r_0 where $x = r - r_0$. Thus, the Taylor expansion in equation 2.38 becomes:

$$E = E_0 + \frac{1}{2} \sum_{i=1}^{3N} \sum_{j=1}^{3N} \left[\frac{\partial^2 E}{\partial x_i \partial x_j} \right]_{x=0} x_i x_j \quad (2.42)$$

We can now define the second derivative component of equation 2.38 as a $3N \times 3N$ Hessian matrix:

$$H_{ij} = \left[\frac{\partial^2 E}{\partial x_i \partial x_j} \right]_{x=0} \quad (2.43)$$

These second derivatives can be estimated using finite-difference approximations:

$$H_{ij} = \left[\frac{\partial^2 E}{\partial x_i \partial x_j} \right]_{x=0} \cong \frac{E(\delta x_i, \delta x_j) - 2E_0 + E(-\delta x_i, -\delta x_j)}{\delta x_i \delta x_j} \quad (2.44)$$

Once all the elements of the Hessian are calculated, a mass-weighted Hessian matrix is defined. Upon diagonalisation of this matrix, eigenvalues ω are reproduced. Equation 2.41 can then be used to calculate the frequencies⁶¹.

VASP, the main software used in this work, can determine the Hessian matrix by defining IBRION=5 in the INCAR file. In this thesis, vibrational frequency calculations were used to (i) Confirm Transition States: A transition state was confirmed as a structure with the calculated gradient on all atoms lower than the geometry optimisation criteria and with a single imaginary frequency mode (negative force constant). The motion along the eigenvector of the negative frequency was visualised to confirm that it corresponded to the expected bond breaking/forming process (ii) Obtain IR spectra by calculating the derivative of the dipole moment with respect to the atomic Cartesian displacement.

2.7 Nudged Elastic Band and Dimer Method

Determining activation energy barriers is considered to be of central importance in the field of catalysis. In order to determine the energy barrier, it is important to identify the lowest energy pathway for the rearrangement of a group of atoms from one stable configuration to another. This path is often referred to as the “minimum energy path” (MEP). The potential energy maximum along the MEP gives us the saddle point energy allowing us to determine the activation energy barrier⁶².

One of the main methods used in order to find the minimum energy path is the Nudged Elastic Band (NEB) method. This method works by optimising a number of intermediate images along the reaction pathway. However, the optimisation is a constrained optimisation where each image finds the lowest energy possible while maintaining equal spacing to the neighbouring images. This is achieved by adding spring forces along the band between the images. The minimisation of the elastic band is achieved by projecting out the perpendicular component of the spring force and the parallel component of the true force. Thus, the total force acting on the image is:

$$F_i = F_i^S|_{\parallel} - \nabla E(R_i)|_{\perp} \quad (2.45)$$

where $\nabla E(R_i)|_{\perp}$ is the true force and is given by:

$$\nabla E(R_i)|_{\perp} = \nabla E(R_i) - \nabla E(R_i) \cdot \hat{\tau}_i \quad (2.46)$$

where E is the energy of the system and $\hat{\tau}_i$ is the normalised local tangent at image i .

The spring force $F_i^S|_{\parallel}$ is given by the following equation:

$$F_i^S|_{\parallel} = k(|R_{i+1} - R_i| - |R_i - R_{i-1}|)\hat{\tau}_i \quad (2.47)$$

where k is the spring constant.

An optimisation algorithm is used to move the images along the reaction pathway according to the force calculated in equation 2.45. Most of the time however, none of the images end up at or close to the saddle point and thus the saddle point energy needs to be estimated using interpolation. Therefore, the activation energy obtained is subject to a large uncertainty.

In order to resolve this problem, a slight modification was applied to the standard NEB method. The climbing image NEB⁶³ uses the same method to determine the minimum energy pathway but a stricter convergence criterion to the saddle point is used. The climbing image NEB requires two sets of calculations: (i) the regular NEB is run in order

to identify the image with the highest energy i_{max} (ii) The force on the image with the highest energy is not calculated using equation 2.45 but rather using the full force due to the potential with the elastic band component inverted as shown in equation 2.48. As a result, the energy along the band is maximised but minimised in all other directions.

$$\begin{aligned} F_{i_{max}} &= -\nabla E(R_{i_{max}}) + 2\nabla E(R_{i_{max}})|_{\parallel} \\ &= -\nabla E(R_{i_{max}}) + 2\nabla E(R_{i_{max}}) \cdot \hat{\tau}_{i_{max}} \hat{\tau}_{i_{max}} \end{aligned} \quad (2.48)$$

The Dimer method that has been developed by Henkelman and Jónsson^{64,65} can also be used to find transition states. This method is a lot less computationally demanding as it only relies on two images instead of the 7-10 images required by the NEB. The two images have almost the same set of $3n$ coordinates but are slightly displaced from each other in order to depict the dimer direction. The initial dimer direction is usually provided by the user. In our case, this was normally either guessed if the transition state is simple such as the motion of oxygen cleavage or an NEB is first run, and if the frequency calculation at the highest point does not correspond to a transition state, this is then used to calculate the dimer direction as the difference between the coordinates of the highest image and the image before or after. Once the initial dimer direction is provided, the curvature along the axis is computed using finite differences. The saddle point algorithm involves the movement of the dimer uphill which is done in two parts: rotation and translation. Each time a translation step is performed, the dimer has to be rotated to find the lowest curvature mode. The minimum and maximum magnitude of the rotational force is defined by the user. Thus, minimising the energy with respect to the rotational force ensures that the dimer is aligned with the lowest curvature mode. The saddle point is then defined as the maximum along the lowest curvature direction.

2.8 Density of States

Density of states provides us with useful information with regard to the distribution of electron states with respect to the energy for a given material. It is defined as the number of electron states per unit volume per unit energy:

$$g(E) = \frac{1}{\Omega_g} \frac{dN}{dE} \quad (2.49)$$

where Ω_g is the volume of the reciprocal space.

The density of state for simple metals can be calculated for most of the energy band using equation 2.50:

$$g(E) = \frac{1}{2\pi^2} \left(\frac{2me}{\hbar^2} \right)^2 E^{1/2} \quad (2.50)$$

Within a Density of States plot, there are two characteristic bands: the valence band and the conduction band. The valence band is below the Fermi level and contains all occupied states whilst the conduction band is above it and has unoccupied states. In a way, the top of the valence band corresponds to the Highest Occupied Molecular Orbital (HOMO) and the bottom of the conduction band corresponds to the Lowest Unoccupied Molecular Orbital (LUMO).

In order to understand the meaning of the Fermi level, we will start by introducing the Fermi function. The Fermi function $f(E)$ determines the probability that an available state at an energy E will be occupied by an electron under equilibrium conditions. Thus, the Fermi function is a probability distribution function:

$$f(E) = \frac{1}{1 + e^{\frac{E-E_F}{kT}}} \quad (2.51)$$

where E_F is the Fermi Energy, k is the Boltzmann constant, and T is the temperature in Kelvin.

As T approaches zero:

If $E < E_F$, the value of the Fermi function is 1 which means that the probability of finding an electron for all energy levels less than the Fermi level is 100%.

If $E > E_F$, the value of the Fermi function is zero indicating that there are no electrons present above the Fermi level.

Catalytic reactions over metal surfaces normally occur through the creation and breaking of bonds between the frontier orbitals of adsorbates and the electrons of the valence band close to the Fermi level of the atoms on the surface. Thus, the valence

electron density of states close to the Fermi-level is one of the factors that determines the catalytic activity of metals such as Au and Pd⁶⁶. One of the important characteristics of a DOS plot that influences the catalytic activity and selectivity of metal surfaces is the position of the d-band centre relative to the Fermi-level. The d-band centre is calculated as the first moment of the projected d-band density of states with reference to the Fermi level⁶⁷.

2.9 Implementation of DFT

In this thesis, we use Density Functional Theory as implemented in the VASP (Vienna *ab initio* Simulation Package)^{68 69 70 71} code. The implementation of Kohn-Sham equations discussed in section 2.3 is performed using an iterative matrix-diagonalization scheme which is implemented using three main algorithms: Conjugate gradient, block Davidson, and a Residual Minimisation Scheme-Direct Inversion in the Iterative Subspace (RMM-DIIS)^{72 73 74 75}. In this work, a mixture of the Davidson and the RMM-DIIS algorithms are used. The Broyden Mixing method is also used for the mixing of the charge density⁷⁶.

A standard job calculation within VASP requires four input files: POSCAR, INCAR, KPOINTS, and POTCAR. The POSCAR file contains the lattice geometry and the ionic positions; these can be represented as either fractional or cartesian coordinates. Selective dynamics can be activated which gives the user the option to control which atoms are free to move and which are to remain fixed. Upon optimisation, a new file is generated which is called CONTCAR; this is similar in structure to a POSCAR file but contains the updated optimised ionic positions. This is normally used as the new POSCAR when a job does not converge within the allocated wall time. The INCAR file is the central input file of VASP which allows to the user to decide the kind of job that needs to be run and what parameters to activate. A standard optimisation INCAR file used in this thesis, is shown below.

```
ISTART = 1      # 0: New job, 1: Continuation job
PREC = Accurate
GGA = PE       # Use the PBE functional
ENCUT = 400    # Set planewave cutoff by hand
ICHARG = 2     # Initiate charge as superposition of atomic charges
NSW = 2000     # Maximum number of ionic steps
IBRION = 1     # 1: Quasi NR, 2: Conjugate gradient
EDIFF = 1E-4   # Electronic relaxation threshold, 1E-4 is default
EDIFFG= -1E-2  # Electronic relaxation threshold, 1E-3 is default
               # negative implies use forces rather than energy change
ISIF = 2      # Calculate forces and stress tensor but only relax
ions
```

```
ISYM=0          # Switch off symmetry
# Settings for speed
ALGO = Fast     # RMM-DIIS algorithm for electrons
LREAL = .FALSE. # evaluate projection operators in real space
NSIM = 4        # blocked algorithm update, four bands at a time
NPAR = 4
ISPIN = 2
IVDW = 11      #D3-dispersion correction
VDW_S6 = 0.75  #D3-dispersion correction
# Recommended option for preventing force noise
#
LDIPOL=.TRUE.   #Dipole correction
IDIPOL=3        #Dipole correction in the Z-direction
```

The KPOINTS file contain the *k*-point coordinates and the mesh size for creating the *k*-point grid. The POTCAR file contains the pseudopotential for each of the atoms used in the calculations. The order of the atoms in the POTCAR has to match the order of the atoms in the POSCAR.

Once all of these files are present within the same directory, a job script is then used to run the calculation. These are run on CPU resources provided by Supercomputing Wales(HAWK) and Materials Chemistry Consortium (ARCHER and THOMAS). The number of cores per node differ by machine (HAWK = 40 cores, ARCHER & THOMAS = 24 cores) and thus benchmarking needs to be performed in order to determine the number of nodes needed. For example, a standard surface optimisation calculation would require 1 node on Hawk but two nodes on ARCHER or THOMAS. However, more resources are required for adsorption calculations or frequency jobs. The most time-consuming calculations used in this work were the Nudged-Elastic Bands calculations discussed in section 2.7. These normally require about 10 images per job, and thus 5 nodes were required for NEB calculations on HAWK (20 cores per image) or 10 nodes on THOMAS and ARCHER.

Chapter 3 Partial Oxidation of Methane to Methanol on Au and Pd Surfaces

The aim of this chapter is to use Au and Pd surfaces to study their reactivity for the partial oxidation of methane to methanol using H₂O₂ and molecular O₂ as oxidants. Previous experimental work has demonstrated the superior activity of the 50:50 Au:Pd alloy system over the pure metals for the partial oxidation of methane to methanol. Here, we explore the performance of the pure metals at each of the steps of the reactions mechanism by calculating adsorption energies of intermediate species and energy barriers for each of the steps.

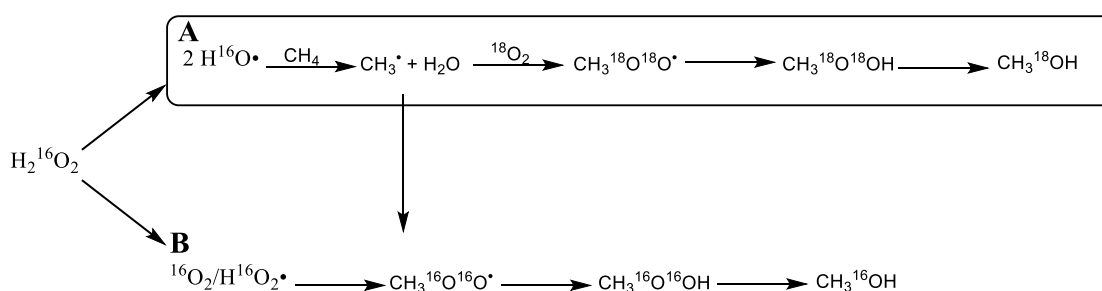
3.1 Introduction

As discussed in section 1.3.1, various Au- and Pd-containing catalysts have been studied for the partial oxidation of methane to methanol. One of the main oxidants used in activating methane for this reaction is hydrogen peroxide^{28,31}. However, the main problem with hydrogen peroxide is its commercial expense which is higher than that of methanol making the entire process economically unviable. Moreover, as reported in the work of Agarwal *et al.*,³¹ the use of hydrogen peroxide with Au:Pd colloids supported on titania resulted in a high decomposition rate of the hydrogen peroxide (72%) which hindered the formation of any products. Interestingly, the rate of decomposition was significantly less on the unsupported alloy colloids (38%) with substantially more products being formed with the methyl hydroperoxide being the primary product.

These factors have led the group of researchers to investigate the role played by hydrogen peroxide in the reaction. The Methyl hydroperoxide intermediate was the first and the major product observed under the reaction conditions which implies a primary termination step of the methyl radical with either a hydroperoxyl radical or molecular oxygen (Scheme 1) originating from the decomposition of hydrogen peroxide. Since the reaction of methyl radicals with molecular oxygen has been previously reported to take place at high rates⁷⁷, the effect of adding molecular oxygen to the reaction mixture was investigated.

The addition of 5 bar of molecular oxygen in the presence of a 1000 μmol of hydrogen peroxide resulted in an increase in the product yield from 15.7 μmol to 26.8 μmol with a high selectivity of 95% to the primary oxygenates (methanol, methyl hydroperoxide, and formic acid)³¹. As previously explained in section 1.3.1 of the introductory chapter,

isotope labelled experiments confirmed that the source of oxygen in the primary oxygenates was indeed molecular oxygen. However, no oxygenated products were observed in the absence of hydrogen peroxide suggesting that hydrogen peroxide is essential for initiating the series of radical reactions. Interestingly, decreasing the amount of hydrogen peroxide whilst maintaining the same pressure of molecular oxygen resulted in an increase in the product yield with a reduction in the amount of hydrogen peroxide consumed. This observation means that, once there are enough hydroxyl radicals in the reaction mixture to activate methane, molecular oxygen can then be used to form the methyl hydroperoxide intermediate which can then be converted to methanol (scheme 1A). The monometallic Au and Pd colloidal nanoparticles showed no activity for methane oxidation thus suggesting that the synergistic effect of the alloy affects the reactivity and stability of this reaction. The proposed reaction mechanism in the presence and absence of molecular oxygen is shown in scheme 1.



Scheme 1: Proposed reaction scheme of the partial oxidation of methane to methanol **(A)** in the presence of molecular oxygen and hydrogen peroxide **(B)** in the presence of only hydrogen peroxide.

In this chapter, we aim to use Density Functional Theory in order to rationalise the poor performance of the monometallic colloids in comparison to the alloy. By modelling low index surfaces of Au and Pd, we study the reaction mechanism in scheme 1**(A)** by studying the adsorption of intermediate species and the energy barriers for each of the elementary steps in the reaction mechanism. We then use these data in order to explain why the alloy is needed for this reaction.

We split the catalytic cycle into three main steps (figure 3.1): (1) the initiation reaction *i.e.* the activation of hydrogen peroxide (structure 1) and the formation of hydroxyl radicals (structure 2) (2); the formation of the primary intermediate, methyl

hydroperoxide (structures **2-6**) (**3**); and the cleavage of the methyl hydroperoxide to form methanol (structures **7** and **8**).

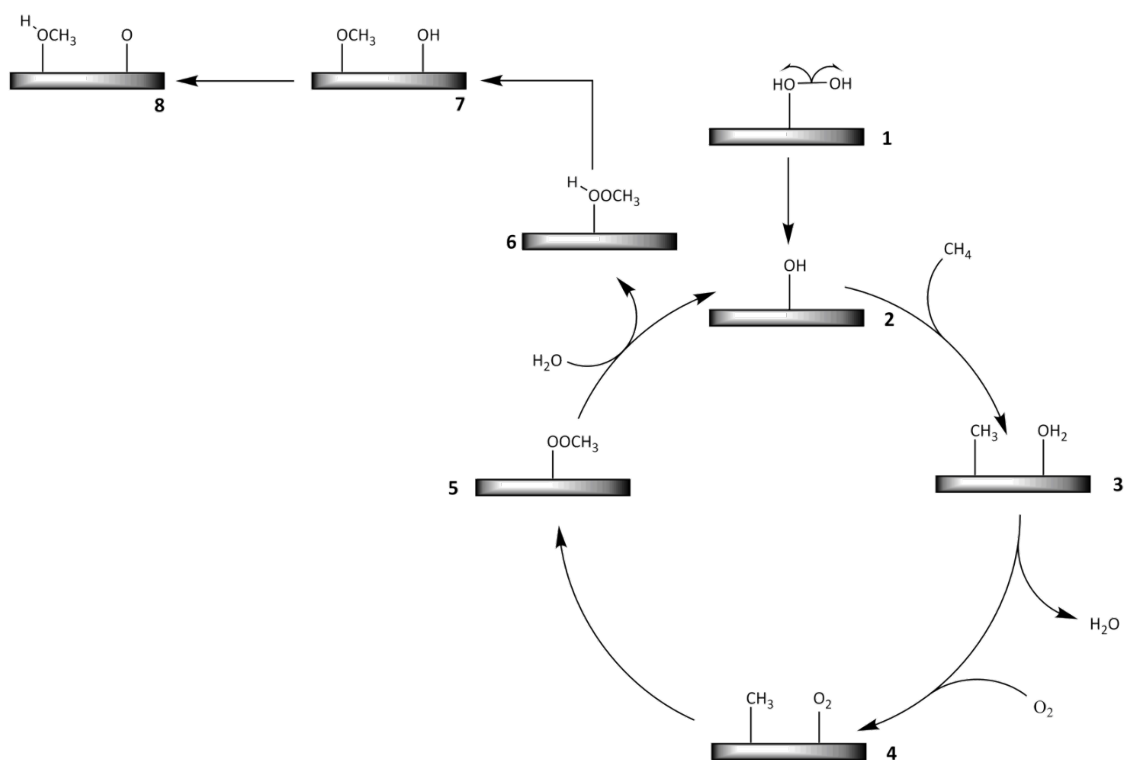


Figure 3.1: The catalytic cycle for the formation of methanol

3.2 Computational Details

As discussed in Chapter (2), we use Density Functional Theory (DFT) as implemented within the VASP (Vienna Ab initio Software Package) code^{68,69,70,71}. The Perdew-Burke-Ernzerhof (PBE) exchange-correlation functional^{51,78} is employed to account for the exchange and correlation effects with the projector augmented-wave (PAW) method used to represent core states^{79,80}. Previous work has shown that the use of the PBE functional to study the interaction of organic compounds on transition metal surfaces to be a good representative of adsorption energies and transition states^{52,53, 54,55}.

The convergence criteria for the energy cut off and the electronic self-consistent field (SCF) threshold were set to 400 eV and 10^{-4} eV respectively. Calculations were also set to converge when the forces are less than 0.01 eV \AA^{-1} for adsorption calculations and $0.001 \text{ eV \AA}^{-1}$ for bulk and surface optimisation calculations.

Dispersion corrections were included to account for van der Waals interactions using Grimme's empirical DFT -D3 model⁸¹. Dipole correction along the z-direction of the slab was also applied in all calculations. 5-layered (111) and (100) surfaces were cut from the optimised bulk. The number of atoms in the (111) surfaces was set to 80 atoms. As for the (100) surfaces, two different slab sizes were used: 40- and 90- atom slabs. The use of the larger slab was needed in order to avoid interactions between the adsorbates in the periodically repeated slabs in the x- and y-directions. The 90-atom slab was used to model: the hydrogen abstraction from methane, the formation of the methyl peroxy intermediate, and the activation of methane by an oxygen atom.

In each of the surfaces, the bottom three layers were fixed with the top two layers free to move. In order to avoid interactions between the periodically repeated slabs, a vacuum layer of 13 \AA is introduced above the surface. A Monkhorst-Pack grid was used to sample the Brillouin zone.⁸² For optimisation calculations, the number of k-points used was $7 \times 7 \times 7$ for the bulk, and $7 \times 7 \times 1$ for the surfaces. As for the adsorption calculations, $3 \times 3 \times 1$ k-points were used. These parameters were benchmarked and are reported in the supplementary information.

The energy of adsorption was calculated as:

$$E_{ads} = (E_{ad+sl} - E_{sl} - E_{ad}) \quad (1)$$

where E_{ad+sl} is the electronic energy of the adsorbed structure, E_{sl} is the energy of the slab, and E_{ad} is the energy of the adsorbate in gas phase.

The Nudged Elastic Band (NEB) method was used to find the transition states. Transition states were then confirmed using frequency calculations. A transition state was confirmed as a structure with the calculated gradient on all atoms lower than the geometry optimisation criteria and with a single negative (imaginary force constant) mode. The motion along the eigenvector of the negative mode was visualised to confirm that it corresponded to the expected bond breaking/forming process.

It is usually possible for the adsorbate on a surface to have more than one configuration and we would expect the lowest energy configuration to have the greatest population of adsorbates. Our nomenclature defines the possible configurations with respect to the position of the atoms of the adsorbate relative to the positions of the nearest metal atoms. This is defined in figure 3.2. The adsorbate atoms can be in a top (over a metal atom as shown by the triangle in figure 3.2(a)), bridge (between two metal atoms as shown by the circle in figure 3.2(a)), or hollow (between three metal atoms as shown by the rectangle in figure 3.2(a)) position. On the (111) surface there are also two types of hollow sites commonly referred to as hcp-hollow (grey rectangle) and fcc-hollow (white rectangle). Figure 3.2(b) shows an example of a hollow-top configuration.

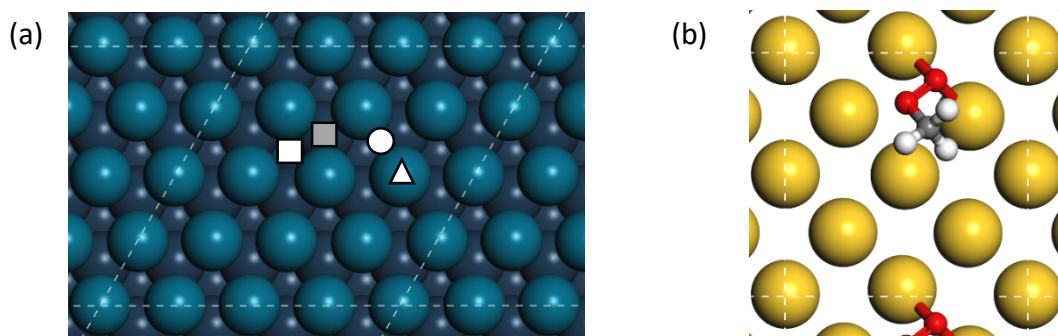


Figure 3.2: (a) The position of the atoms in top (triangle), bridge (circle), and hollow (rectangle/ grey rectangle) configurations (b) Example of a Hollow-Top configuration on the Au(100) surface. (Colour code: Gold: Au, Blue: Pd, Red: O, Grey: C, and White: H)

3.3 Methodology

The face centred cubic (fcc) bulk structures of both Au and Pd were initially optimised using the ISIF = 3 command which allows us to alter all three degrees of freedom (position of the atoms, cell shape, and cell volume). Once optimised, two different low index surfaces of Au and Pd were then cut as shown in figure 3.3. Since structural examination of the Au-Pd alloy colloids revealed that the nanoparticles produced experimentally have mostly icosahedral structures with some cuboctahedral characteristics, we modelled the (111) and the (100) surface facets. Figure 3.3 shows the structure of the surfaces used.

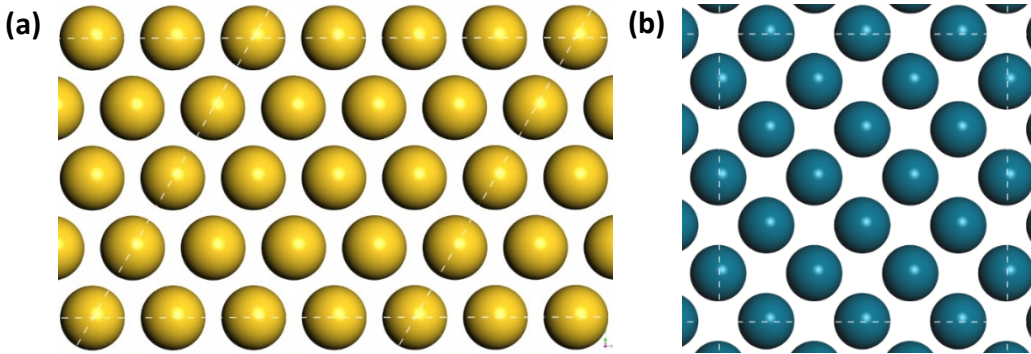


Figure 3.3: Structure of the (a) Au(111) and (b) Pd(100) surfaces.

(Colour code: Gold: Au, Blue: Pd)

In order to avoid interactions between adjacent slabs, a sufficient vacuum gap has to be introduced above the highest layer. Therefore, the vacuum thickness needs to be increased until the value of the surface energy becomes constant. The surface energy was computed using the following formula:

$$E_{surf} = \frac{E_{slab} - (n \times E_{bulk})}{2 \times S.A.} \quad (3.1)$$

where E_{slab} is the electronic energy of the slab, n is the ratio of the number of atoms in the slab to the number of atoms in the bulk, E_{bulk} is the electronic energy of the bulk and $S.A.$ is the surface area of the surface.

As shown in figure 3, the shape of the (100) surface is a square and thus the surface area is equal to the square of the lattice constant. Whilst the area of the (111) surface can be calculated as the area of a parallelogram and thus is equal to:

$$S. A_{(111)} = a \times b \times \sin \theta \quad (3.2)$$

where a and b correspond the dimensions of the surface and θ is the angle between the two vectors.

The benchmarking for the vacuum gap was performed without D3-dispersion. Table 3.1 shows the surface energy for the different vacuum gaps tested.

It is evident from table 3.1, that there is very little variation in the surface energy with respect to the varying size of the vacuum gap thickness. Even though the surface energy is constant, the vacuum gap needs to be large enough in order to accommodate the adsorbate and avoid Van der Waals interactions between the periodically repeated slabs in the z -direction. Thus, throughout this chapter, a vacuum gap size of 13 Å was used. As expected, the surface energy of the (111) surface for both metals is lower than the (100) surface suggesting that the (111) surface is more stable. This is expected as the number of neighbouring atoms for each atom in the (111) surface is greater than that in the (100).

Table 3.1: Surface energy with varying vacuum gap sizes without D3-dispersion.

| Vacuum gap size | Au(111) $E_{surf}/$ $J m^{-2}$ | Au(100) $E_{surf}/$ $J m^{-2}$ | Pd(111) $E_{surf}/$ $J m^{-2}$ | Pd(100) $E_{surf}/$ $J m^{-2}$ |
|------------------------|---|---|---|---|
| 7 | 0.694 | 0.851 | 1.328 | 1.540 |
| 8 | 0.695 | 0.850 | 1.328 | 1.541 |
| 9 | 0.695 | 0.848 | 1.328 | 1.540 |
| 10 | 0.695 | 0.848 | 1.327 | 1.540 |
| 11 | 0.694 | 0.847 | 1.327 | 1.540 |
| 12 | 0.694 | 0.847 | 1.326 | 1.540 |
| 13 | 0.693 | 0.846 | 1.325 | 1.539 |
| 14 | 0.693 | 0.846 | 1.325 | 1.539 |
| 15 | 0.693 | 0.846 | 1.325 | 1.538 |

Once the size of the vacuum gap was determined, it was essential to benchmark the number of relaxed layers needed for this study. The surfaces shown in figure 3 are 5-layer surfaces and thus in order to reduce the computational time needed for optimisation, one can determine which layers are allowed to move and which are to remain fixed by introducing the “selective dynamics” tag in the input (POSCAR) file. Thus, to ensure that the upper surface of the slab model is relaxed while retaining the bulk character of the lower layers, benchmark structural optimisation calculations with a

varying number of relaxed layers were performed. Once again, the surface energy calculated using equation 3.1 was used to determine the number of fixed layers needed. Moreover, in order to determine the effect of dispersion correction on the surface energy, the benchmarking was performed with the D3-dispersion tag included in the INCAR file. Table 3.2 shows the surface energy variation for the four surfaces.

Table 3.3.2: Surface energy variations with varying number of relaxed layers

| No. of relaxed layers | Au(111) $E_{\text{surf}}/\text{J m}^{-2}$ | Au(100) $E_{\text{surf}}/\text{J m}^{-2}$ | Pd(111) $E_{\text{surf}}/\text{J m}^{-2}$ | Pd(100) $E_{\text{surf}}/\text{J m}^{-2}$ |
|-----------------------|--|--|--|--|
| 1 | 1.427 | 1.548 | 2.122 | 2.300 |
| 2 | 1.414 | 1.548 | 2.112 | 2.300 |
| 3 | 1.413 | 1.548 | 2.112 | 2.300 |
| 4 | 1.409 | 1.545 | 2.109 | 2.299 |
| 5 | 1.409 | 1.545 | 2.109 | 2.299 |

As shown in table 2, there is very little variation in the surface energy with respect to number of relaxed layers (figure 3.4). Most of the surface energy fluctuation is in the third decimal place, with the surface energy becoming constant at 3 relaxed layers. Based on this, we decided to model the reaction in scheme 1 with the top two layers relaxed and the bottom three fixed.

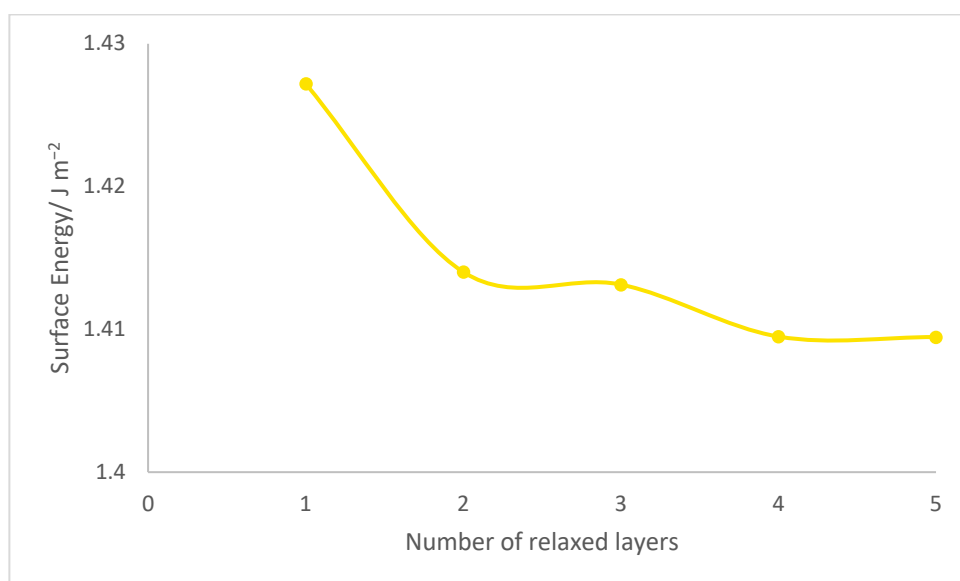


Figure 3.4: Surface energy variation with respect to the number of relaxed layers for the Au(111) surface

Another interesting observation that can be made from the results in tables 1 and 2 is that dispersion correction has a significant effect on the surface energy. This is because local and semi-local density functions such as PBE are unable to correctly describe Van

der Waals interactions resulting from dynamical correlations between fluctuating charge distributions⁸³, and thus a dispersion correction factor is needed to correct that. As expected, the surface energy calculated with the D3-dispersion correction is closer in magnitude to the surface energy reported experimentally (1.5 J m⁻² for Au and 2.0 J m⁻² for Pd)⁸⁴.

As discussed in section 2.7, DOS can be used to study and compare the reactivity of catalysts. Figure 3.5 (a) and 3.5(b) show the DOS plot of the top layer of the Au(111) and Pd(111) surface respectively. The d-band centre of Au and Pd is located at -2.961 eV and -1.497 eV respectively. Thus, the fully occupied 5d-band of Au is positioned well below the Fermi level making the 5d-valence electrons less accessible for bonding with the adsorbate. The 4-d band of Pd on the other hand, extends through the Fermi-level with the d-band centre a lot closer to the Fermi-level than in the case of Au making the 4d-valence electrons a lot more accessible for the formation of chemisorption bonds. This means that we would expect Pd to be a lot more catalytically active than Au which is demonstrated by the significantly higher adsorption energies that are observed with Pd than Au throughout this work.

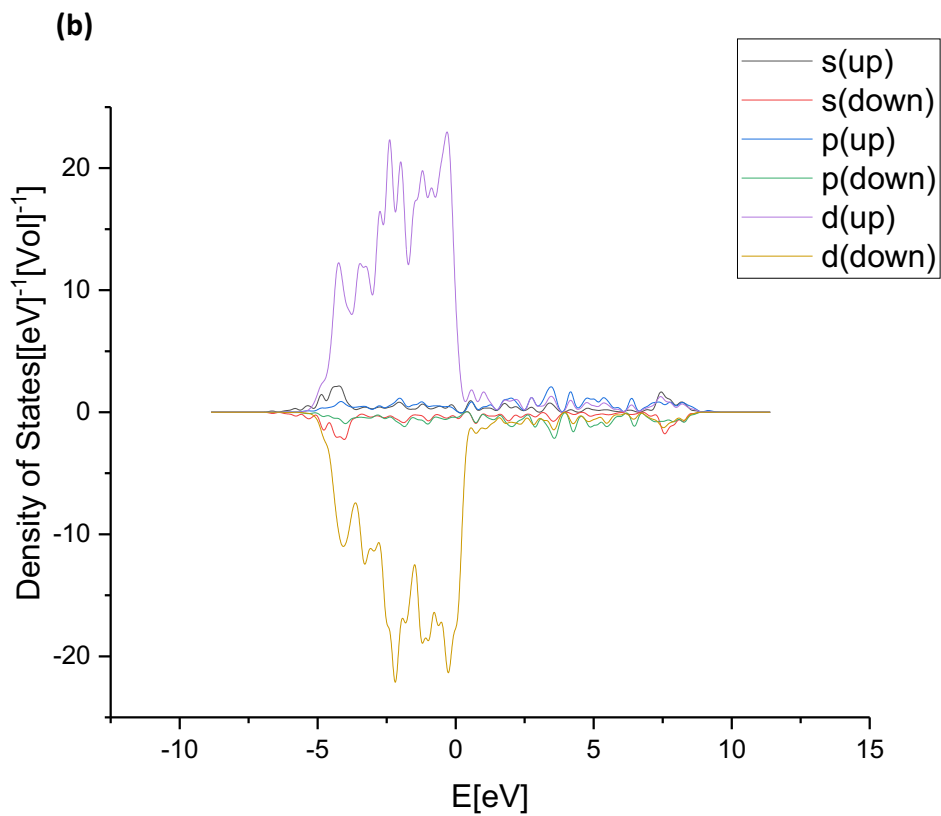
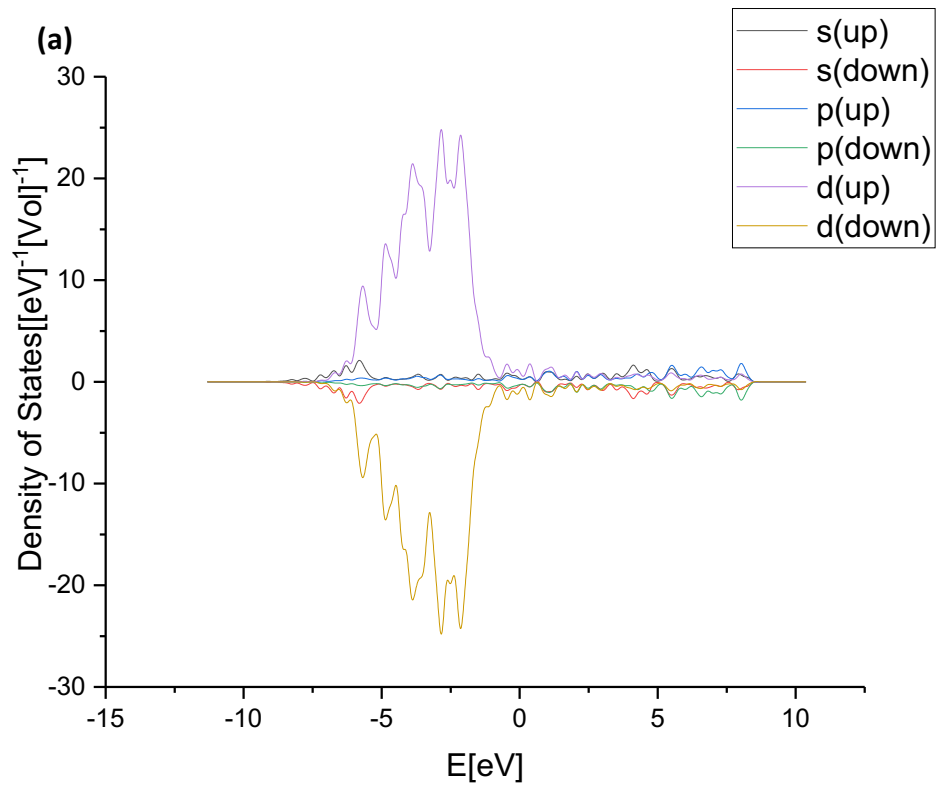


Figure 3.5: Density of States plot of: (a) Au(111) surface and (b) Pd(111) surface

3.4 Results and Discussion

3.4.1 Adsorption and cleavage of hydrogen peroxide on the surface

The first step in the catalytic cycle in figure 3.1 involves the cleavage of hydrogen peroxide on the surface in order to form hydroxyl radicals. The adsorption of the hydrogen peroxide was, therefore, studied first followed by transition state calculations in order to determine the energy barrier for the HO—OH bond cleavage.

Table 3.3 summarises the adsorption energy of hydrogen peroxide on the different surfaces, the M—O distance, and gives a graphical image of the corresponding configurations. In all the configurations examined, one of the oxygen atoms of the hydrogen peroxide molecule was in a hollow position with the other being in a top position. The hydrogen atom bonded to the oxygen atom in the hollow position also pointed towards the surface so that the oxygen atom at this position does not directly interact with metal atoms. As this configuration of the hydrogen peroxide is unexpected, we decided to test whether the pointing of the hydrogen towards the surface is a result of the dispersion correction contribution included in our calculations. However, no change in the geometry was observed on optimising the structure on the Pd(100) surface without the dispersion parameter.

The adsorption energies for hydrogen peroxide on the Pd surfaces is around 14 kJ mol^{-1} more negative than that on the most stable form on the Au(100) surface, which gives a more favourable adsorption energy than Au(111) by about 2.6 kJ mol^{-1} . The M—O distance for the oxygen at the top site is correspondingly shorter for the Pd surfaces than it is for the Au surfaces.

In order to form hydroxyl radicals on the different surface, hydrogen peroxide must cleave; therefore, cleaved structures of H_2O_2 were optimised on the different surfaces. For example, on the Au(111) surface, three configurations for the cleaved structure were examined as shown in figure 3.6. The least stable configuration was found to be the one where the two hydroxyl radical are sharing one of the Au atoms (inset top left) with an adsorption energy of $-10.1 \text{ kJ mol}^{-1}$. The configuration where the two hydroxyl radicals are adsorbed in a bridge position forming a hydrogen bond was found to be more stable than the one where the two hydroxyl radicals are pointing towards each other (inset top right) by about 20 kJ mol^{-1} . In all the configurations tested, both hydroxyl radicals relaxed to bridge positions. The most stable configuration was also found to have one of the

hydrogen atoms of one hydroxyl group orientated towards the oxygen of the other hydroxyl group (with hydrogen bonding) as shown in figure 3.6 (inset bottom middle).

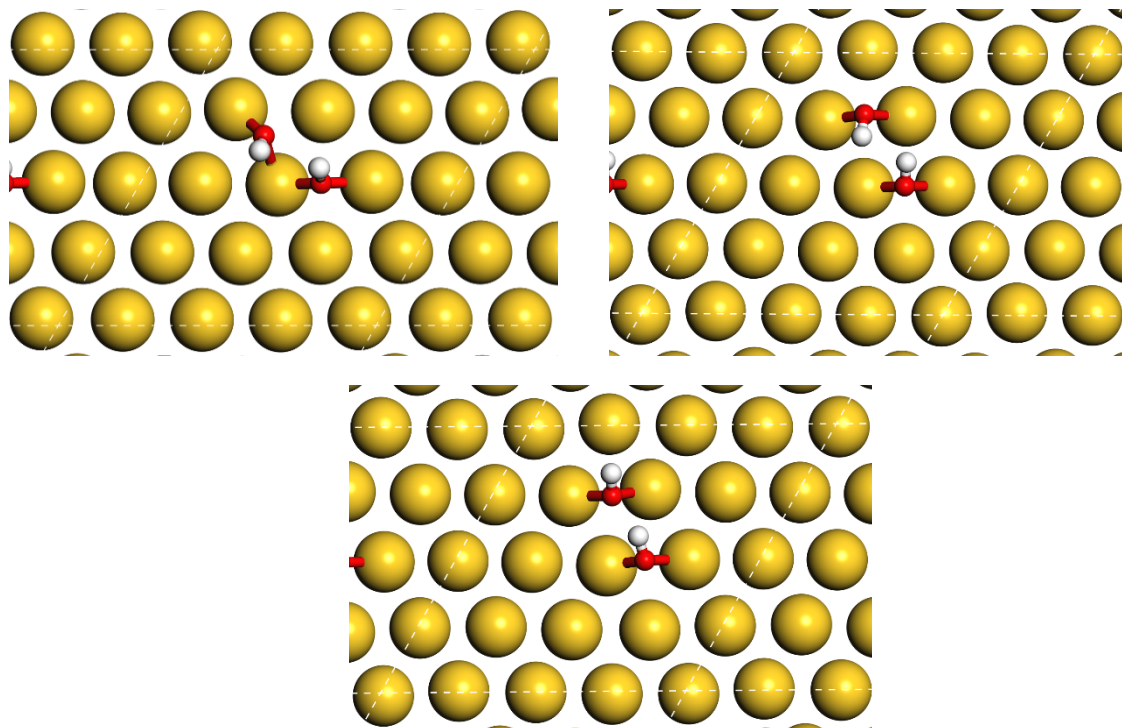


Figure 3.6: Different adsorption configurations for the adsorption of the hydroxyl radicals on the Au(111) surface. (Colour code: Gold: Au, Red: O, Grey: C, and White: H)

The dissociation energy for the different surfaces was also computed as:

$$E_{dis} = E_{cl} - E_{st} \quad (3.3)$$

where E_{cl} and E_{st} are the energies of the dissociated and the molecularly adsorbed structures respectively and Table 3.3 also shows the dissociation energy for H_2O_2 over each of the surfaces studied based on the most stable adsorption energies in each case. For both Pd and Au surfaces, the dissociation reaction is exothermic and the two hydroxyl radicals are more stabilised by the (100) surface than by the (111) surface, by around 78 kJ mol^{-1} for Pd and 88 kJ mol^{-1} for Au, which is probably due to the high stability of the (111) surfaces resulting in them being less reactive than the (100). We also note that the two hydroxyl radicals bind more strongly to the Pd surfaces than the Au surfaces with the Pd(100) giving an adsorption energy of $-316.1 \text{ kJ mol}^{-1}$ with reference to the gas phase H_2O_2 molecule.

Table 3.3: The adsorption and cleavage of hydrogen peroxide on different surfaces of Au and Pd (Colour code: Gold: Au, Blue: Pd, Red: O, Grey: C, and White: H)

| Surfaces | E_{ads} / kJ mol^{-1} | M—O / \AA | E_{dis} / kJ mol^{-1} | OH...O(H) / \AA | Configuration |
|-----------------|--|-----------------------|--|-----------------------------|---------------|
| Au (111) | -44.6 | 2.769 | -97.5 | 1.837 | |
| Au (100) | -47.2 | 2.662 | -185.8 | 1.788 | |
| Pd (111) | -61.1 | 2.342 | -176.1 | 1.933 | |
| Pd (100) | -62.1 | 2.328 | -254.0 | 1.752 | |

In order to determine the energy barrier for the cleavage of hydrogen peroxide on the different surfaces, transition state calculations were performed using the configurations in Table 3.3 as start points to determine the barrier for the HO—OH bond cleavage.

As discussed in section 3.2, the Nudged Elastic Band method was used to find the transition states. The start and end points of the NEB corresponded to the hydrogen peroxide structure on the surface and two adsorbed hydroxyl radicals respectively. 10 images were used to depict the cleavage of the hydrogen peroxide on the surface.

Figure 3.7 compares the potential energy surface critical points for H₂O₂ cleavage on all four surfaces. The cleavage of the hydrogen peroxide proceeds with relatively low barriers in all cases. The barriers for the cleavage of H₂O₂ on the Au(100) and Au(111) surfaces were found to be 38.3 kJ mol⁻¹ and 57.3 kJ mol⁻¹, respectively, which suggests that the barrier is early in the reaction co-ordinate, as it is not strongly influenced by the much stronger adsorption of the OH radicals to the Au(100) surface in the final state. By examining the transition state of both the (111) and the (100) surfaces, we conclude that the (111) surface is more effective at stabilising the two hydroxyl groups by forming an Au—O bond (≈ 2.252 Å) to one of the hydroxyl radicals with the other hydroxyl radical on top of a Au atom 2.559 Å away. On the other hand, on the Au(100) surface, only one of the hydroxyl radicals is stabilised by the surface with a Au—O bond of 2.307 Å, which explains why the barrier on the Au(100) surface is smaller than the Au(111).

Determination of the barriers for the cleavage of the hydrogen peroxide on the Pd surfaces was more challenging. On the Pd (100) surface, the rotation of the OH in the hollow position, resulted in cleavage of the hydrogen peroxide. This is demonstrated by the structure of the transition state in figure 3.8 which closely resembles the unclevaed hydrogen peroxide structure. As a result, the activation energy for the cleavage of hydrogen peroxide on the Pd (100) corresponds to the rotation of the hollow site OH hydroxyl group of the molecule which requires only 4.5 kJ mol⁻¹. The same behaviour was observed for the Pd (111) surface where the rotation of the hydroxyl group results in bond cleavage. The barrier required for the hydrogen rotation in this case was found to be 21.7 kJ mol⁻¹.

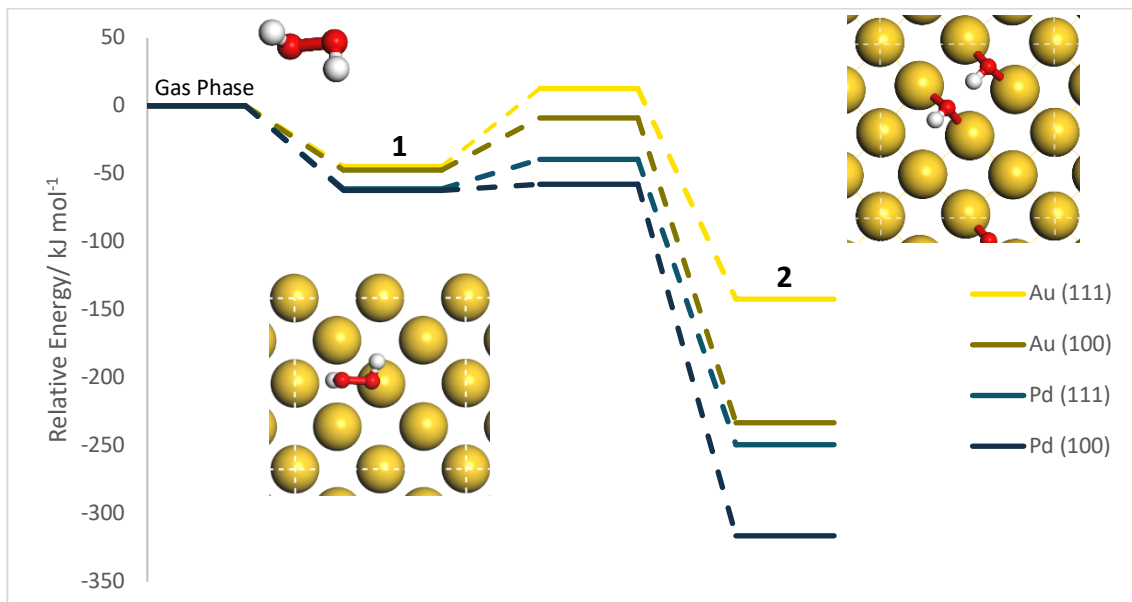


Figure 3.7: Potential Energy Landscapes of the cleavage of H_2O_2 on the different surfaces relative to the hydrogen peroxide in gas phase (Step 1-2) (Colour code: Gold: Au, Red: O, Grey: C, and White: H)

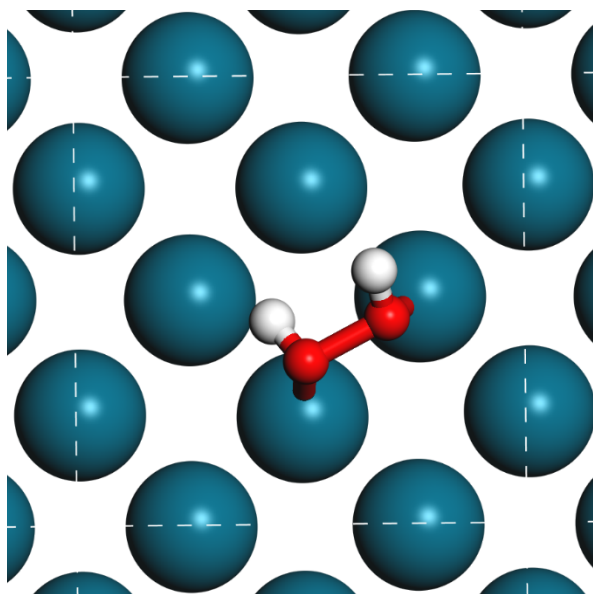


Figure 3.8: Structure of the transition state for the cleavage of the hydrogen peroxide on the Pd(100) surface (Colour code: Blue: Pd, Red: O, Grey: C, and White: H)

Thus, the transition from structure **1** to structure **2** in figure 3.1 is relatively easy to accomplish on all four surfaces with the Pd surfaces exhibiting a higher affinity than Au for the adsorption of the hydrogen peroxide resulting in almost barrierless activation energies.

3.4.2 Hydrogen abstraction from Methane

The second step of the reaction mechanism in figure 3.1 involves the abstraction of hydrogen from methane by hydroxyl radicals. As previously discussed in section 1.2.1, this step is considered to be the most energetically demanding in the conversion of methane to methanol due to the stability of the C—H bond.

Configurations of methane and hydroxyl groups were optimised on the different surfaces. As shown in section 3.4.1, the hydroxyl radical prefers to bind on the surfaces in a bridge position and thus this was kept in mind when studying the adsorption of methane and the hydroxyl radical on the surface. Upon optimisation, the hydroxyl group remained in a bridge position with the hydrogen of the hydroxyl group pointing away from the methane molecule. The pointing of the hydrogen away from the methane was essential as this would provide a suitable end point for the NEB where water is produced upon hydrogen abstraction. The position of the methane on the surface shows very little variation with site and thus since the methyl radical prefers to bind to surface in a top position, the methane was placed in a top position which upon optimisation remained in a top position 3-3.5 Å away from the closest metal atom.

Upon hydrogen abstraction from methane, a methyl radical and water are produced. Both species are stabilised by adsorption at top sites in the optimised structures with the methyl group directly bonding to a metal atom. Table 3.4 gives the difference in the calculated energies, ΔE , between the methane molecule and OH surface radical reactant and the methyl surface radical and water product of the reaction along with the length of the M-C bond to the methyl radical. Regarding the overall energy profile, ΔE is negative (ie exothermic) for the (111) surfaces and small but positive (ie endothermic) on the (100) surface, indicating there is a stronger driving force for hydrogen abstraction on the (111) surface than the (100) surface with the driving force on Au being higher than that on Pd. The more negative ΔE for the (111) surfaces suggests that the (111) surfaces are more effective at stabilising the methyl radical than the more active (100) surfaces. In order to rationalise this behaviour, the adsorption energies of hydroxyl and methyl radicals were calculated (see Table 3.5). Interestingly, these energies show that the adsorption of both species is stronger on the (100) surfaces compared to the (111) surfaces. However, the difference in adsorption energies between the two surfaces is less significant in the case of the methyl radical with the

difference being 11.0 kJ mol⁻¹ for the Au surfaces and only 0.6 kJ mol⁻¹ for the Pd surfaces, which means that the higher (endothermic) energies observed for the (100) surfaces are largely a result of the higher adsorption energy of a hydroxyl radical on these surfaces.

Table 3.4: ΔE of hydrogen abstraction from methane by hydroxyl radicals. M corresponds to a metal atom

| Surfaces | ΔE / kJ mol ⁻¹ | M—C / Å | M—O / Å |
|-----------------|-----------------------------------|---------|---------|
| Au (111) | -35.8 | 2.120 | 2.961 |
| Pd (111) | -25.2 | 2.044 | 2.409 |
| Au (100) | +5.5 | 2.102 | 2.710 |
| Pd (100) | +5.6 | 2.033 | 2.451 |

Table 3.5: Comparison of the adsorption energies of the hydroxyl and methyl radical on the different surfaces

| Surfaces | E_{ads} of OH / kJ mol ⁻¹ | E_{ads} of CH ₃ / kJ mol ⁻¹ |
|-----------------|---|--|
| Au (111) | -202.8 | -148.3 |
| Pd (111) | -264.0 | -193.7 |
| Au (100) | -248.5 | -159.3 |
| Pd (100) | -299.6 | -194.3 |

Based on the M—C distances in table 3.4, it is evident that the methyl radical is being stabilised by all four surfaces. The interaction of the product water molecule with the surfaces is minimal with bond distances of about 2.7-3 Å in the case of the Au surfaces. Moreover, visualisation of the charge densities at an iso-surface of 0.05 |e| showed no interaction between the water molecule and the different surfaces.

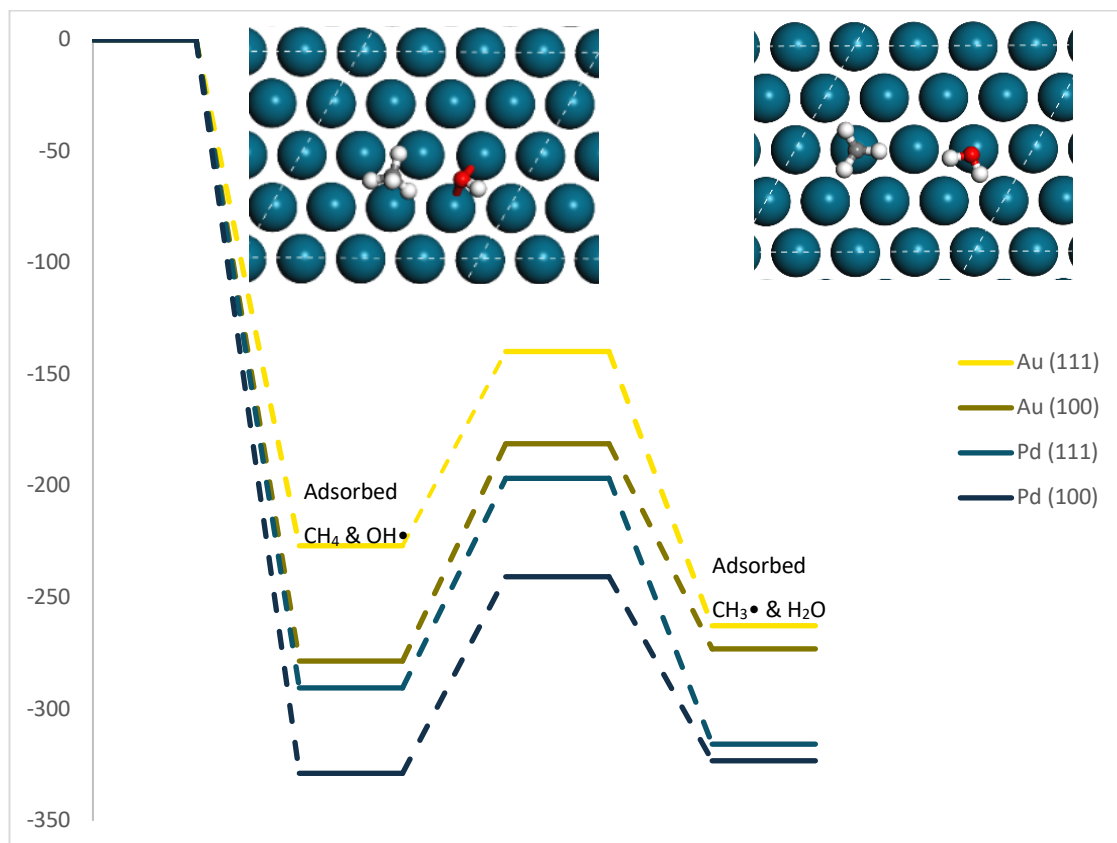


Figure 3.9: Potential Energy Landscapes of the hydrogen abstraction from methane on the different surfaces relative to the adsorbed hydroxyl radical on the surface and methane and oxygen in gas phase (intermediate 2). (Colour code: Blue: Pd, Red: O, Grey: C, and White: H)

Transition state calculations were then performed to determine the activation energy of the hydrogen abstraction reaction. As shown in figure 3.9, the barriers for the abstraction of hydrogen from methane on the Au(111), Au(100), Pd(111), and Pd(100) were found to be 87.1 kJ mol^{-1} , 97.4 kJ mol^{-1} , 93.9 kJ mol^{-1} , and 88.1 kJ mol^{-1} , respectively. The activation energy to abstract a hydrogen from methane on the Au(111) surface is, therefore, lower than on the Au(100) surface. However, an opposite trend is observed on the Pd surfaces where the activation energy for the hydroxyl radical to abstract a hydrogen from methane is lower on the Pd (100) surface. The structures of the transition states show that, for Pd surfaces (figure 3.10), the hydroxyl radical remains in a bridge configuration, with the methyl radical being strongly stabilised by the surface ($\text{Pd}-\text{C} \approx 2.2 \text{ \AA}$). Comparison of the starting structure of the NEB with the transition state for the Pd (100) surface, shows a very minor increase in the Pd—O distance (from 2.1 \AA to 2.2 \AA), whereas over the Pd (111) surface, one of the Pd—O was elongated to 2.3 \AA at the transition state. However, for both Au surfaces, the hydroxyl radical moves away

from the bridge configuration identified for adsorbed OH on the surfaces and switches to a top position at the transition state. Since the adsorption of the hydroxyl group is stronger on the (100) surface than on the (111) (table 3.5), the hydrogen abstraction step is easier on the (111) surface.

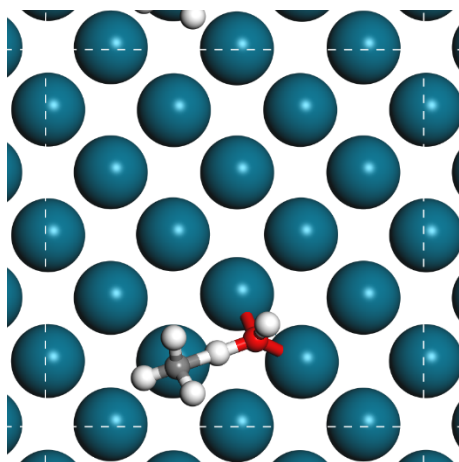


Figure 3.10: Structure of the transition state of the hydrogen abstraction from methane by a hydroxyl radical on the Pd(100) surface (Colour code: Blue: Pd, Red: O, Grey: C, and White: H)

The next step in the reaction mechanism is the formation of methyl hydroperoxide, the primary intermediate observed experimentally in this reaction³¹. This is a key step as it will determine the ability of molecular oxygen to bind to the methyl radical to form the methyl peroxy intermediate ($\text{CH}_3\text{OO}\bullet$).

3.4.3 Formation of the Methyl Peroxyl Intermediate

The formation of the methyl peroxy radical involves the reaction of the methyl radical produced in the earlier step with molecular oxygen. To study this step using the NEB approach, adsorbed configurations of molecular oxygen and a methyl radical were optimised on the four metal surfaces to provide starting points. End point structures were also optimised based on the adsorption of a methyl peroxy radical.

Three different configurations were found for the methyl radical and molecular oxygen on the Au(100) surface as shown in figure 3.11. In all three cases, the methyl radical was in a top position but with different orientations of the oxygen molecule. The most stable configuration (b) has the oxygen molecule in a bridge position with each oxygen atom directly bonded to two gold atoms. The least stable configuration (c) has one of the oxygen atoms in a bridge position with the other not interacting with the surface. The O—O bond distance calculated for O₂ in the triplet state in gas phase is 1.234 Å and thus as shown by the O—O bond distances in table 3.6, configurations in which both oxygen atoms are in a bridge position are more activated by the surface, explaining their higher energy of adsorption. Configuration C was studied as in separate calculations, this was lowest energy configuration (bridge-hollow) for the adsorption of the CH₃OO• intermediate on the Au(100) surface. Thus, the process by which the CH₃OO• intermediate on the Au (100) surface is formed involves the breaking of two Au—O bonds of one of the oxygen atoms in order to accommodate the methyl radical.

The two most stable configurations of the adsorbed methyl radical and molecular oxygen from the Au(100) surface were constructed and optimised on the Pd(100) surface. Once again, the structure with molecular oxygen adsorbed in a bridge-bridge configuration was found to be more stable than that with the molecule in a top-top configuration. The oxygen adsorbed in a bridge-bridge position also has an O—O bond which is more activated. The adsorption of the methyl peroxy radical on the Pd(100) resulted in cleavage of the O—O bond without a barrier, forming a surface bound CH₃O and an oxygen atom.

Bridge-Bridge configurations for the CH₃ and O₂ structures were harder to attain on the (111) surfaces. Configurations that were constructed with molecular oxygen arranged top-top on the Pd (111) surface, switched to top-bridge upon optimisation. On the Au (111) surface, on the other hand, both top-top and top-bridge configurations were

stable. The top-bridge configuration was found to be more stable than the top-top configuration.

On the Pd (111) surface, the preferred configuration for the adsorption of the methyl peroxy radical was found to be a bridge-top configuration (table 3.7). A top-top configuration was also attainable but was found to be less stable. In both structures, the O—O bond was found to be activated by the surface. When the methyl peroxy radical is in a top-top configuration, the Pd (111) surface activates the O—O bond (1.463 Å) to a similar extent to the more open (100) surface (O-O = 1.433 Å). The O—O bond distance for the optimised bridge-top configuration had a value of 1.667 Å, suggesting that the molecule has dissociated into a methoxy radical and an oxygen atom.

As for the Au (111) surface, the lowest energy mode of adsorption of the CH₃OO• was found to be a top-hollow position. Top-top configurations were investigated but these switched to a top-hollow position upon optimisation. Figure 3.12 shows the different configurations of the CH₃OO• on the Au (111), Au (100), and Pd (111) surfaces.

Table 3.6: Adsorption of CH₃ & O₂ on the different surfaces relative to the adsorbed hydroxyl radical on the surface and methane and oxygen in gas phase.

| Surfaces | CH ₃ & O ₂ | M—O ₁ | M—O ₂ | O—O | C—M |
|-----------------------------|---|------------------|------------------|-------|-------|
| Au (100) | E _{ads} / kJ mol ⁻¹ | Å | Å | Å | Å |
| Top-Top (A) | -7.67 | 2.173 | 2.172 | 1.345 | 2.099 |
| Bridge-Bridge (B) | -27.7 | 2.286 2.294 | 2.311 2.290 | 1.423 | 2.099 |
| Bridge-Hollow (C) | +18.8 | 2.330 2.360 | - | 1.302 | 2.094 |
| Pd (100) | | | | | |
| Top-Top | -99.4 | 2.002 | 2.013 | 1.341 | |
| Bridge-Bridge | -147.9 | 2.100 2.107 | 2.100 2.102 | 1.433 | |
| Au (111) | | | | | |
| Top-Top | +22.0 | 2.293 | 2.277 | 1.323 | 2.040 |
| Bridge-Top | +1.08 | 2.611 2.417 | 2.235 | 1.335 | 2.037 |
| Pd (111) | | | | | |
| Bridge-Top | -111.7 | 2.141 2.135 | 2.022 | 1.376 | 2.056 |

Table 3.7: Adsorption of the $\text{CH}_3\text{OO}\bullet$ intermediate on the different surfaces relative to the adsorbed hydroxyl radical on the surface and methane and oxygen in gas phase.

| Surfaces | $\text{CH}_3\text{OO}\bullet$ | $\text{M}-\text{O}_1$ | $\text{M}-\text{O}_2$ | $\text{O}-\text{O}$ |
|----------------------|---------------------------------------|-----------------------|-----------------------|---------------------|
| Au (100) | $E_{\text{ads}} / \text{kJ mol}^{-1}$ | Å | Å | Å |
| Bridge-Hollow | -105.5 | 2.260 2.240 | - | 1.467 |
| Au (111) | | | | |
| Top-Hollow | -97.8 | 2.149 | - | 1.454 |
| Pd (111) | | | | |
| Bridge-Top | -121.5 | 2.060 2.054 | 2.198 | 1.667 |
| Top-Top | -118.2 | 2.008 | 2.309 | 1.463 |

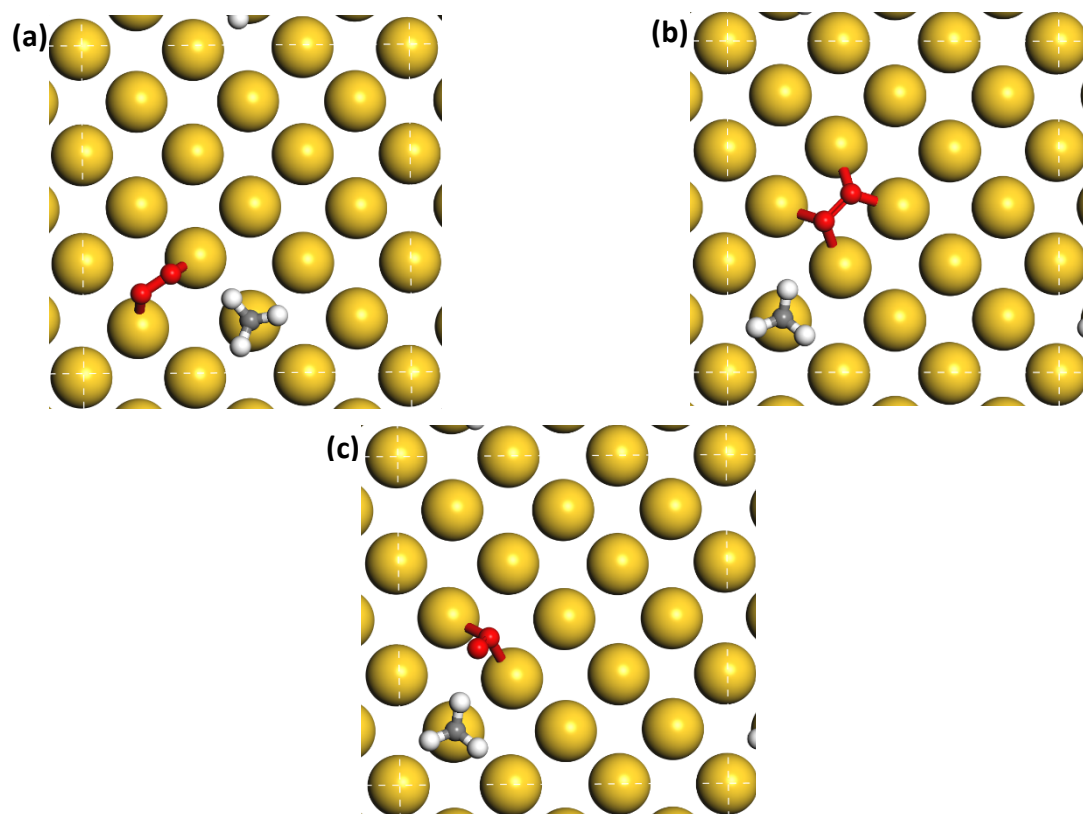


Figure 3.11: Different configurations for the adsorption of methyl radical and molecular oxygen on the Au (100) surface: (a) oxygen in top-top (b) oxygen in bridge-bridge and (c) oxygen in bridge-hollow (Colour code: Gold: Au, Red: O, Grey: C, and White: H)

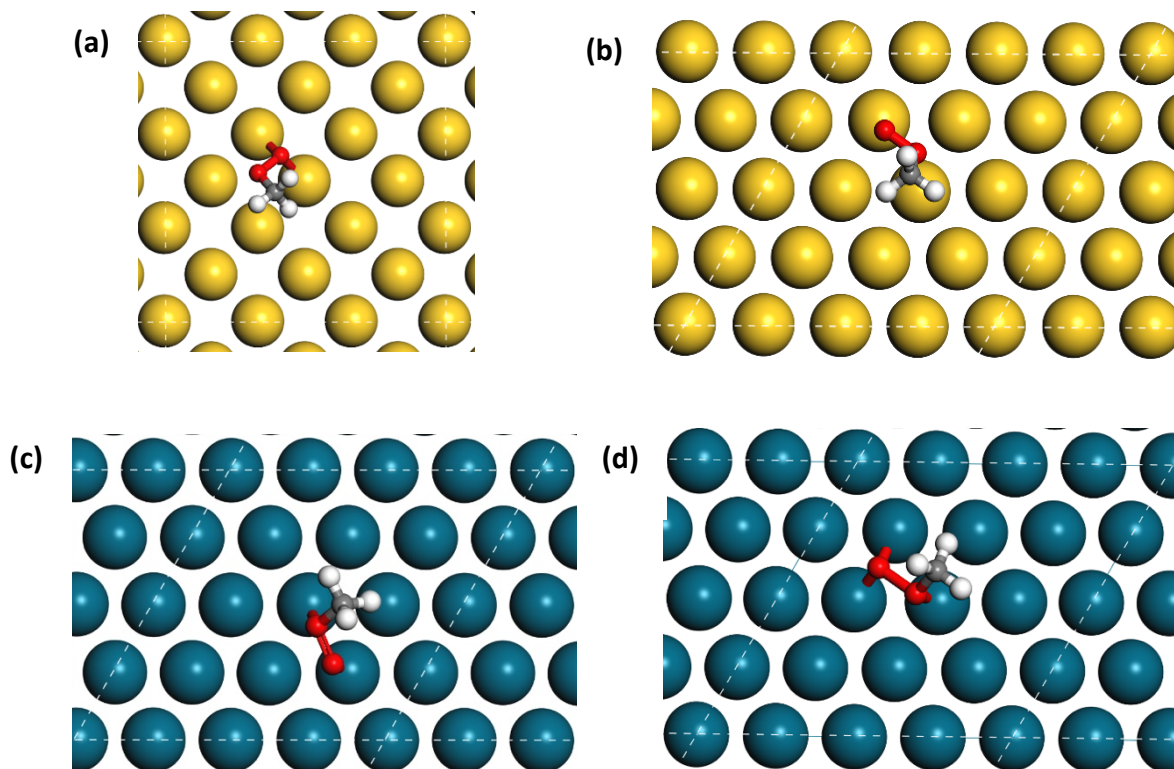


Figure 3.12: Adsorption of the methyl peroxy radical on (a) Au(100) surface (b) Au(111) surface (c) top-top configuration on the Pd(111) surface (d) bridge-top configuration on the Pd(111) surface (Colour code: Gold: Au, Blue: Pd, Red: O, Grey: C, and White: H)

NEB calculations were then run to determine the barrier for the formation of the methyl peroxy radical on the Au surfaces. The structure of the transition state on the Au(100) surface showed that the bridge-bridge position of the oxygen molecule was maintained with a slight elongation of all four Au—O bonds with the bond of the oxygen atom that is strongly interacting with the methyl group stretching from 2.286 Å to 2.572 Å and 2.294 to 2.430 Å. Similarly, the bridge-top position of the oxygen molecule was maintained for the Au(111) surface with the elongation of the Au—O bond of the oxygen in top position from 2.235 Å to 2.243 Å. Significant elongation of the Au—O bond that is strongly interacting with the methyl radical from 2.417 Å to 2.824 Å was also observed with the shortening of the other bond from 2.611 Å to 2.589 Å.

Since the structure of the methyl peroxy radical on the Pd(111) surface is strongly activated but not completely cleaved, we ran transition state calculations on the surface in order to determine the energy barrier for its formation. The structure of the transition state obtained is very similar in geometry to the one obtained on the Au(111) surface

but with a shorter Pd—C (2.315Å vs 2.515Å) suggesting that the stabilisation of the methyl radical on the Pd(111) surface is stronger. Moreover, the oxygen molecule moved to a top-top configuration with Pd—O bond distances of 2.024 Å and 2.162 Å. The barriers for the formation of the methyl peroxy radical relative to the adsorbed methyl and oxygen on the Au(111), Au(100), and Pd(111) surfaces were found to be 64.0 kJ mol⁻¹ , 105.2 kJ mol⁻¹ and 127.8 kJ mol⁻¹. The structure of the transition states along with the energy barriers are shown in figures 3.13 and 3.14, respectively. As noted above, the methyl peroxy radical appears to be unstable on the Pd (100).

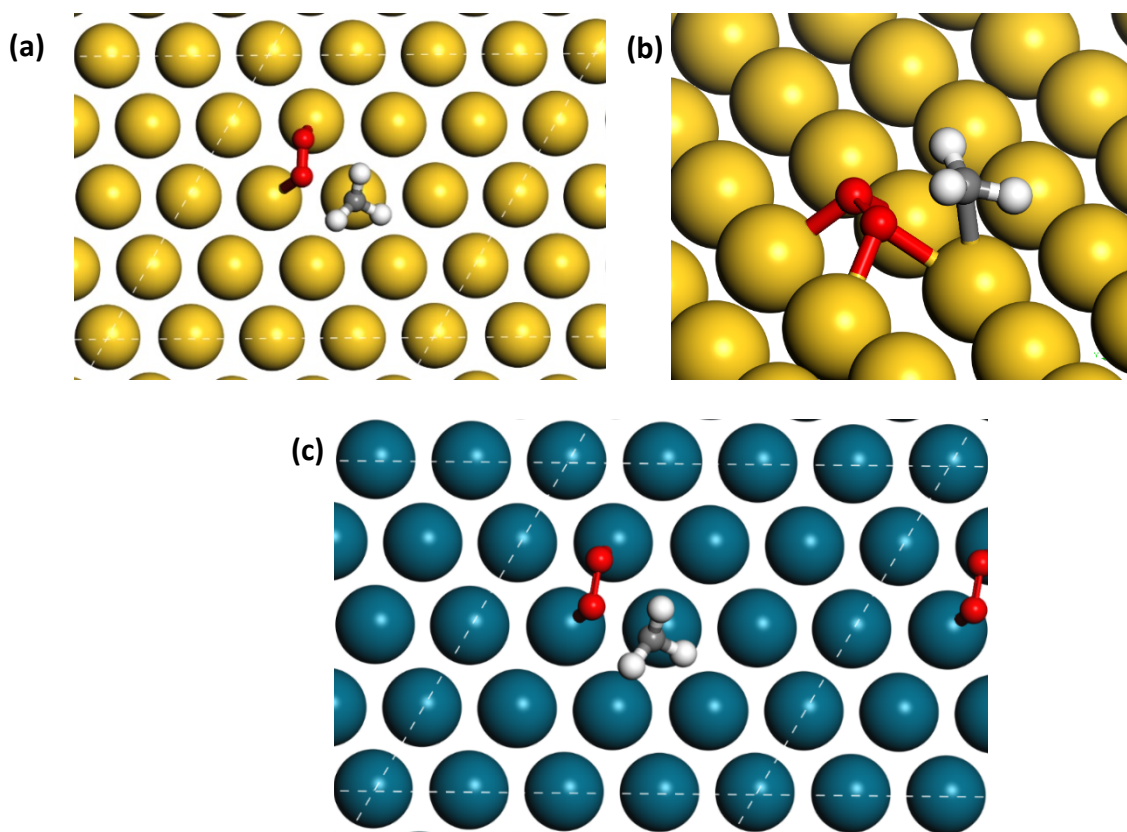


Figure 3.13: Transition state structures of the formation of the methyl peroxy radical on the (a) Au(111) surface (b) Au(100) surface and (c) Pd(111) surface. (Colour code: Gold: Au, Blue: Pd, Red: O, Grey: C, and White: H)

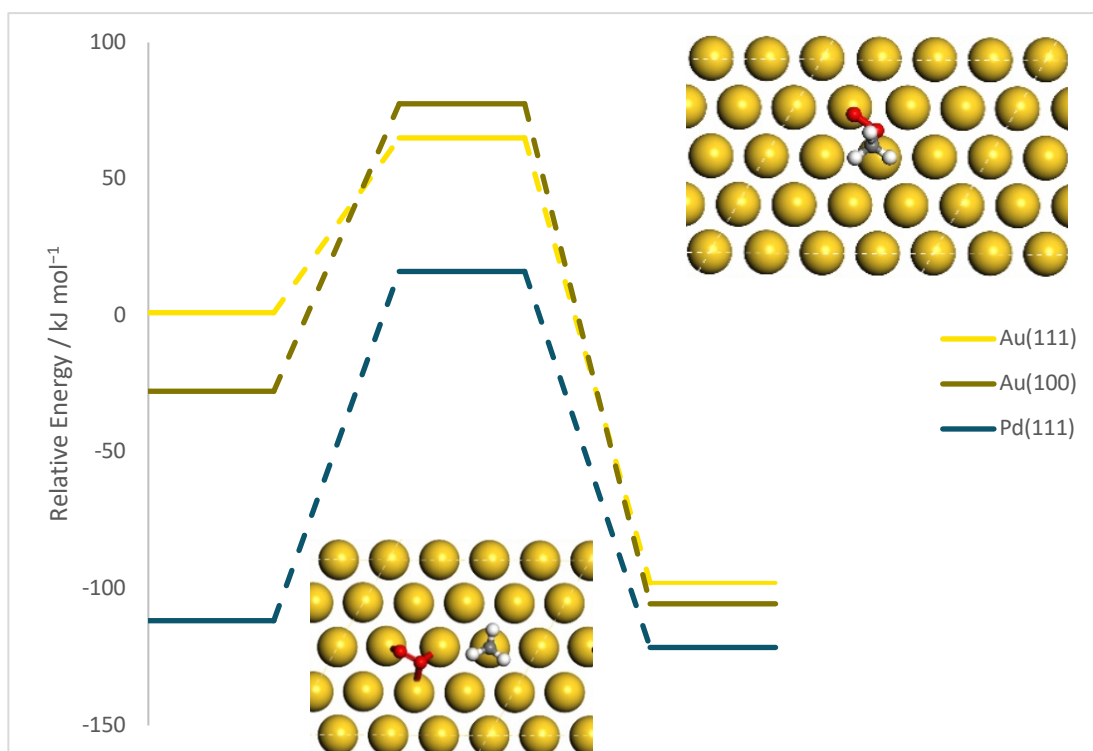


Figure 3.14: Potential Energy Landscapes for the formation of the $\text{CH}_3\text{OO}\bullet$ on the Au surfaces relative to the adsorbed hydroxyl radical on the surface and methane and oxygen in gas phase (intermediate 2). (Colour code: Gold: Au, Red: O, Grey: C, and White: H)

Since the methyl peroxy radical is strongly activated on the Pd surfaces, this means that the barrier for its dissociation is probably very small which means that the methyl peroxy radical is more likely to dissociate than form the methyl hydroperoxide intermediate. Since this is the major product observed experimentally, there must be some modification to the Pd surface that takes place under reaction conditions that prevents the dissociation of the methyl hydroperoxide intermediate. One such modification that was tested is the oxidation of the Pd surface. Thus, we decided to investigate the stability of the intermediate on a highly oxidised Pd(111) surface. Pd (111) surfaces with a monolayer coverage of atomic oxygen were constructed and optimised with varying number of oxygen atoms. Corresponding to the dimensions of our unit cell, a highly oxidised Pd surface had 7 oxygen atoms. The oxygen atoms were positioned in hollow positions such that each oxygen atom can interact with 3 Pd atoms. The hollow positions of the two Pd atoms interacting with the methyl hydroperoxyl radical were left vacant. After the adsorption of the methyl peroxy radical on the 7-

oxygen-atom surface was optimised, random oxygen atoms were removed, one at a time, until the surface was completely deoxidised leaving only the methyl peroxy radical on the surface (figure 3.16). The adsorption energies of the methyl peroxy radical as a function of oxygen coverage were computed and tabulated in table 3.8. Whilst there is little variation in the energy of adsorption with respect to the oxygen coverage, it is evident that there is a clear trend regarding the O—O bond length. As the surface becomes more oxidised, the bond length contracts suggesting that methyl peroxy radical becomes more stable with respect to dissociation on the surface. The different adsorption configurations are shown in figure 3.16. In order to determine the stability of the radical, transition state calculations for the cleavage of the O—O bond on the fully oxidised surface were performed. The energy barrier was found to be around 14 kJ mol^{-1} (figure 3.15). These results highlight that even when the surface is completely oxidised, the Pd surface remains active as only a small barrier needs to be overcome for the radical to cleave on the surface.

Table 3.8: Adsorption energies and O—O bond lengths of the methyl peroxy radical on the oxidised Pd (111) surfaces

| Number of oxygen atoms | O-O bond length/ Å | $E_{\text{ads}} / \text{eV}$ |
|------------------------|--------------------|------------------------------|
| 7 | 1.480 | -1.534 |
| 6 | 1.486 | -1.576 |
| 5 | 1.490 | -1.583 |
| 4 | 1.494 | -1.567 |
| 3 | 1.501 | -1.605 |
| 2 | 1.502 | -1.586 |
| 1 | 1.506 | -1.584 |
| 0 | 1.667 | |

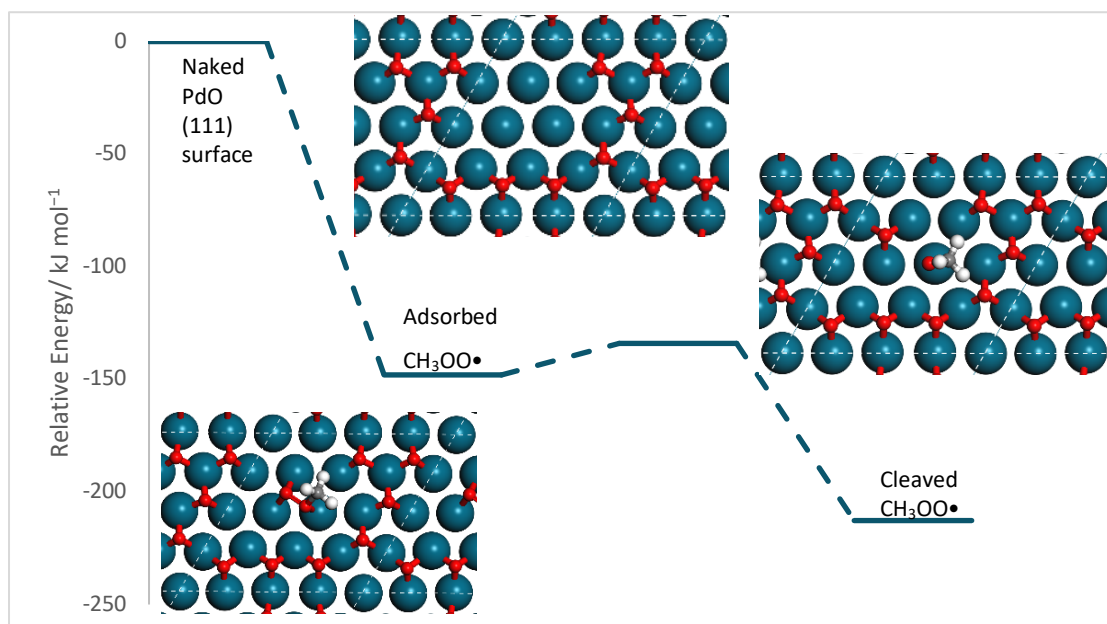


Figure 3.15: Potential Energy Landscape for the cleavage of the O—O bond of the methyl peroxy radical on the fully oxidised Pd(111) surface. (Colour code: Blue: Pd, and Red: O)

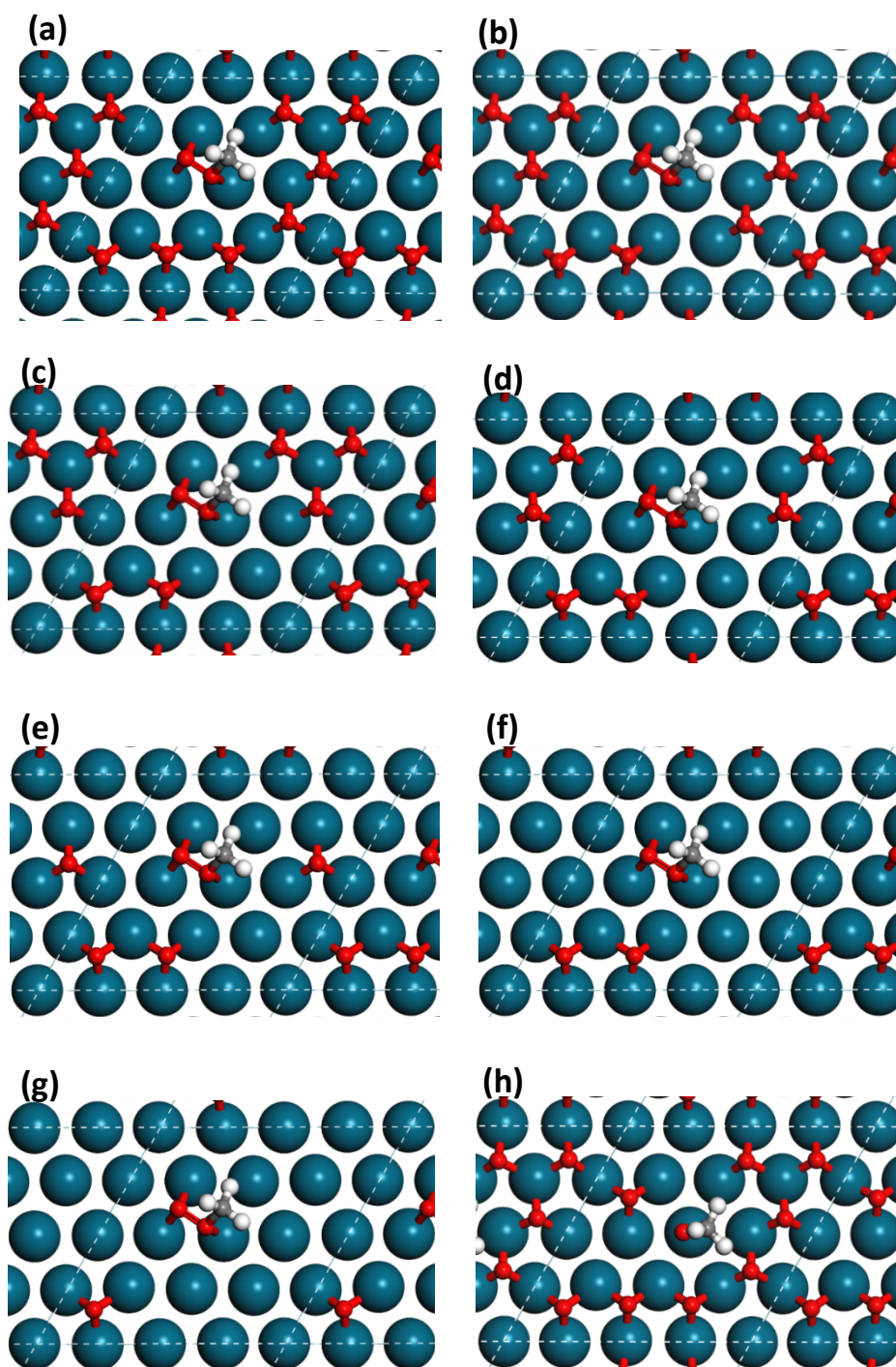


Figure 3.16: Adsorption of the methyl peroxy radical on (a) 7-oxygen-atom monolayer coverage Pd(111) surface (b) 6-oxygen-atom monolayer coverage Pd(111) surface (c) 5-oxygen-atom monolayer coverage Pd(111) surface (d) 4-oxygen-atom monolayer coverage Pd(111) surface (e) 3-oxygen-atom monolayer coverage Pd(111) surface (f) 2-oxygen-atom monolayer coverage Pd(111) surface (g) 1-oxygen-atom monolayer coverage Pd(111) surface. (h) Cleaved methyl peroxy radical on a 7-oxygen-atom monolayer coverage Pd(111) surface. (Colour code: Blue: Pd, and Red: O)

This marks the end of the second step of the catalytic cycle in figure 3.1. In order to compare the different energy barriers for the different steps, the total energy profile relative to the adsorbed hydroxyl radical on the surface and methane and oxygen in gas phase is plotted in figure 3.17.

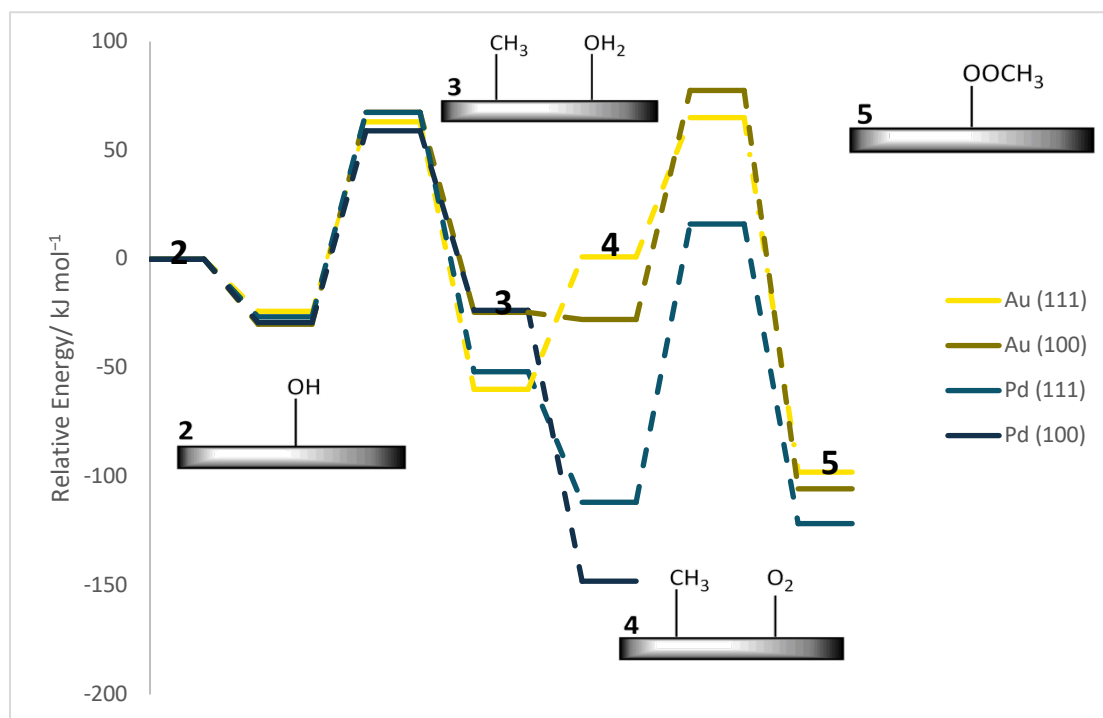


Figure 3.17: Energy profile for methane abstraction and the formation of the methyl peroxy radical on the different surfaces relative to the adsorbed hydroxyl on the respective surfaces, and methane and oxygen in gas phase.

Based on figure 3.17, it is evident that the energy barrier for methane activation is similar across all four surfaces with the energy varying from 87-97 kJ mol⁻¹ and with the Au(111) surface having the smallest barrier. Interestingly, it appears that structure 4 on the Au(111) surface has a lower energy than structure 3 suggesting that the binding of water on the surface is stronger than that of molecular oxygen. In order to consider this effect in more detail, the adsorption energy of water (ΔE_{H_2O}) and molecular oxygen (ΔE_{O_2}) in the presence of a methyl radical, and the energy difference for the displacement of water by oxygen ($\Delta E_{O_2} - \Delta E_{H_2O}$) were computed for the different surfaces (table 3.9).

Table 3.9: Energy required for the desorption of water, adsorption of oxygen, and the energy difference.

| Surfaces | ΔE_{H_2O} / kJ mol ⁻¹ | ΔE_{O_2} / kJ mol ⁻¹ | $\Delta E_{O_2} - \Delta E_{H_2O}$ / kJ mol ⁻¹ |
|-----------------|---|--|--|
| Au (111) | -34.8 | +26.0 | +60.8 |
| Pd (111) | -42.5 | -102.5 | -60.0 |
| Au (100) | -34.2 | -37.5 | -3.3 |
| Pd (100) | -49.3 | -173.7 | -124.4 |

It is evident from table 3.9, that the adsorption of water is favourable on all surfaces with a small energy difference between the Au surfaces and a 6.8 kJ mol⁻¹ energy difference between the Pd surfaces. The energy required to adsorb molecular oxygen is highly favourable on the Pd surfaces with the Pd(100) surface showing a higher affinity for adsorption. The adsorption of molecular oxygen on the Au(111) surface is endothermic, making it thermodynamically unfavourable for molecular oxygen to displace water, which would result in the accumulation of methyl radicals and water molecules on the surface hindering the formation of the methyl peroxy intermediate. As for the Au(100) surface, there is a small energy difference albeit exothermic for the displacement of water by molecular oxygen and it is, therefore, possible for molecular oxygen to displace water on the Au(100) surface. However, the relatively high energy barrier of 105.2 kJ mol⁻¹ for the reaction of methyl radical and molecular oxygen will probably hinder the formation of the methyl peroxy radical.

Since both Pd surfaces exhibited a high affinity for oxygen adsorption, the cleavage of molecular oxygen was studied on the Pd surfaces. On the Pd(111) surface, the activation energy barrier for the dissociation of molecular oxygen was found to be +62.8 kJ mol⁻¹ which is almost half the energy barrier needed for the formation of the methyl peroxy radical from methyl radicals and molecular oxygen (+127.8 kJ mol⁻¹). This result suggests that it is highly likely that molecular oxygen will cleave on the surface before it combines with the methyl radical needed to form the methyl peroxy intermediate. An even smaller barrier of +8.9 kJ mol⁻¹ was observed for the dissociation of oxygen on the Pd(100) surface suggesting that the Pd(100) surface will be completely oxidised upon introducing molecular oxygen into the reaction mixture.

This means that it is highly unlikely that the methyl peroxy radical will form on any of the surfaces. The high affinity of the Pd to molecular oxygen will result in the cleavage of molecular oxygen on the surfaces resulting in the formation of a PdO surface. The low

affinity of the Au surfaces to molecular oxygen will result in the accumulation of water molecules on the surface thus preventing a reaction between the surface-stabilised methyl radical and molecular oxygen.

Since the presence of a PdO layer is very likely on the Pd surfaces, it was interesting to see whether the process of methanol formation is likely to happen via a route involving methane activation by oxygen on the surface. Therefore, hydrogen abstraction from methane by an adsorbed oxygen atom on the surface was studied followed by methanol formation as a result of the reaction of the methyl radical and hydroxyl radical formed. Optimised structures of (CH_4 & O) and ($\bullet\text{CH}_3$ & $\bullet\text{OH}$) were, therefore, modelled on the Pd surfaces. The preferred mode of adsorption for the oxygen atom was a hollow position whereby each oxygen atom was binding to three Pd atoms in the case of the (111) surface and to four Pd atoms in the case of the Pd (100) surface. In both cases, the methane was in a top position with very minimal interaction with the surface.

NEB calculations for the hydrogen abstraction step were then run and the activation energy barriers were computed. In order for the oxygen atom to abstract a hydrogen atom from methane, a movement of the oxygen atom from hollow to bridge position was observed. This results in the formation of a hydroxyl radical which, as demonstrated before, binds more strongly in a bridge configuration with the hydrogen of the hydroxyl radical pointing away from the methyl radical. Figure 3.18 shows the energy barriers for methane activation by oxygen on the different surfaces.

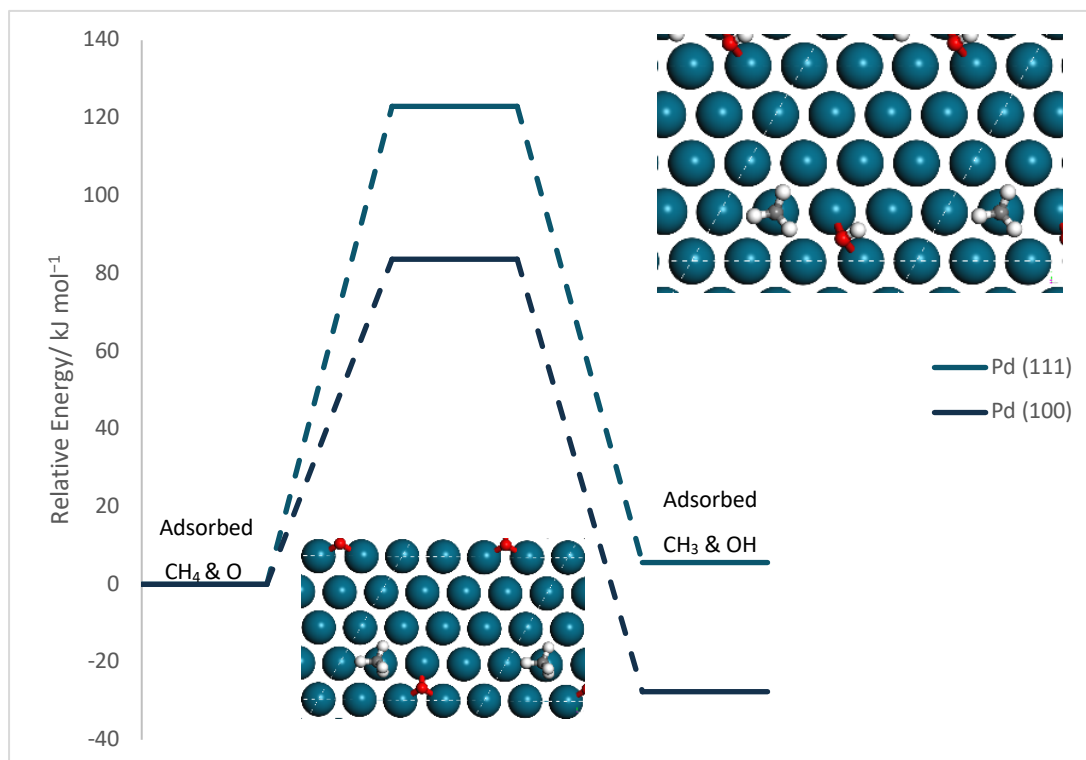


Figure 3.18: Potential Energy landscape for the activation of methane by an oxygen atom relative to the adsorbed methane and oxygen on the respective surfaces.

(Colour code: Blue: Pd, Red: O, Grey: C, and White: H)

The barriers for the hydrogen abstraction from methane by an oxygen atom for the Pd (111), and Pd (100) were found to be $123.0 \text{ kJ mol}^{-1}$ and 83.7 kJ mol^{-1} respectively. In order to rationalise the difference in the energy barrier between the two surfaces, the difference in adsorption energy between an oxygen atom adsorbed in a hollow position and an oxygen atom adsorbed in a bridge position was computed (table 3.10). As shown in table 3.10, more energy is required to move an oxygen atom from a hollow to a bridge position on the (111) surface than on the (100) surface making it a lower energy process for an oxygen atom to abstract a hydrogen from methane on the (100) surface. Moreover, on the (100) surface, it is a less activated process for an oxygen atom (83.7 kJ mol^{-1}) to abstract a hydrogen from methane than it is for a hydroxyl radical (88.1 kJ mol^{-1}). To explain this observation, the energy of reaction for both processes on both surfaces was computed. As highlighted by the data in table 3.11, ΔE_{O} for hydrogen abstraction by an oxygen atom on the (100) surface is exothermic as opposed to the slightly endothermic ΔE_{OH} indicating that there is a stronger driving force for hydrogen abstraction from methane by an oxygen atom as opposed to a hydroxyl radical on the

(100) surface. The opposite trend is observed on the (111) surface where methane abstraction by a hydroxyl radical is thermodynamically favoured over an oxygen atom.

Table 3.10: Adsorption energy of an oxygen atom adsorbed in hollow (O_H) and bridge (O_B) positions on the Pd surfaces relative to half the energy of oxygen in gas phase and the energy difference.

| Surfaces | O_H / kJ mol^{-1} | O_B / kJ mol^{-1} | $O_H - O_B$ / kJ mol^{-1} |
|-----------------|---------------------------------|---------------------------------|---------------------------------------|
| Pd (111) | -112.8 | -83.4 | -29.4 |
| Pd (100) | -132.2 | -108.9 | -23.4 |

Table 3.11: Comparison of the energy of reaction for methane activation by a hydroxyl radical (ΔE_{OH}) and an oxygen atom (ΔE_O) on the Pd surfaces

| Surfaces | ΔE_{OH} / kJ mol^{-1} | ΔE_O / kJ mol^{-1} |
|-----------------|---|--|
| Pd (111) | -25.2 | +5.6 |
| Pd (100) | +5.6 | -27.6 |

The reaction of the methyl and hydroxyl radicals generated in the previous step was then studied. The barriers for methanol formation on the (111) and (100) surface relative to the adsorbed methyl and hydroxyl radical were found to be $+148.6 \text{ kJ mol}^{-1}$ and $+154.6 \text{ kJ mol}^{-1}$ respectively. Since the activation energy of both barriers is relatively high, it is highly unlikely that methanol will ever form on the pure Pd surface via a PdO route. Moreover, the very low barrier for the oxygen cleavage on the Pd(100) surface means that the surface will be rapidly oxidised leaving no vacant sites on which the methyl radical can adsorb.

These results explain why the primary intermediate observed experimentally is methyl hydroperoxide and not methanol. The activation barrier for the formation of the methyl peroxy radical via a methyl radical and molecular oxygen is smaller than the formation of methanol via a methyl radical and a hydroxyl radical making the latter route kinetically unfavourable.

3.4.4 Formation and Adsorption of the methyl hydroperoxide on the surface

Whilst, as discussed above, the formation of the methyl hydroperoxide in significant quantities is unlikely on all four pure metal surfaces, it is still important to study its activation on these surfaces, which will provide us with important insights into its behaviour on the alloyed surfaces.

The methyl peroxy radical generated in the earlier step will need to abstract a hydrogen atom from one of the chemical species in the reaction mixture in order to form the methyl hydroperoxide intermediate. The two possible sources of hydrogen in the reaction mixture are H_2O , and H_2O_2 . Since experimentally, the amount of water present in the reaction mixture is more than the amount of hydrogen peroxide, the most likely process is the abstraction of a hydrogen from water in order to regenerate the hydroxyl radicals needed to activate methane along with the methyl hydroperoxide intermediate. In order to determine the feasibility of this reaction, different configurations of ($\text{CH}_3\text{OO}\cdot$ & H_2O) and (CH_3OOH & OH) were optimised on the Au surfaces. Upon optimisation of the $\text{CH}_3\text{OO}\cdot$ & H_2O on the Au (100) surface, the $\text{CH}_3\text{OO}\cdot$ remained in its preferred mode of adsorption (bridge-hollow) with one of the hydrogen atoms of the water molecule forming a hydrogen bond (1.740 \AA) to the oxygen of the $\text{CH}_3\text{OO}\cdot$ in bridge position. The adsorption of CH_3OOH & OH resulted in the loss of the hydrogen atom from the CH_3OOH and the reformation of the water molecule. Reoptimisation of the two structures with the CH_3OOH physisorbed on the surface was also investigated. This resulted in the reformation of the bond between the CH_3OOH and the surface followed by a hydrogen transfer to the OH group to form water. However, it is likely that the hydrogen transfer might occur in the presence of multiple water molecules or during the desorption of the CH_3OO from the surface.

Since the energy barrier for the hydrogen transfer could not be modelled, we computed ΔE of the reaction by calculating the difference in energy between the products (CH_3OOH & OH) and the reactants ($\text{CH}_3\text{OO}\cdot$ & H_2O). ΔE for the Au (100) surface and the Au(111) surface was found to be $+16.8 \text{ kJ mol}^{-1}$ and $+17.3 \text{ kJ mol}^{-1}$ indicating the equilibrium is slightly towards the left side of the reaction. However, it is important to note that this value does not take into account the presence of copious amounts of water molecules around the slab. In the experimental work performed by Agarwal *et*

*al.*³¹ the amount of H₂O₂ used was as low as 50 μmol and thus since the amount of water in the reaction mixture is a lot more than the amount of H₂O₂, the reaction equilibrium will shift to the right in order to increase the consumption of water (Le Chatelier's principle).

Moreover, based on the adsorption calculations and the small energy barriers for the cleavage of hydrogen peroxide, it is highly likely that the barrier for the cleavage of hydrogen peroxide is much smaller than the barrier for the formation of a hydroperoxyl radical. Work performed by Plauk *et al.* have shown that the barrier for the cleavage of the O-H bond in hydrogen peroxide is eight times higher than the barrier for the cleavage of the O-O on the Pd(100) surface and 3.5 times on the Pd(111)⁸⁵.

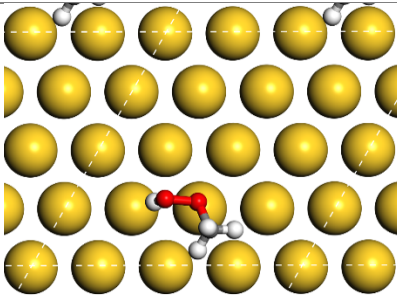
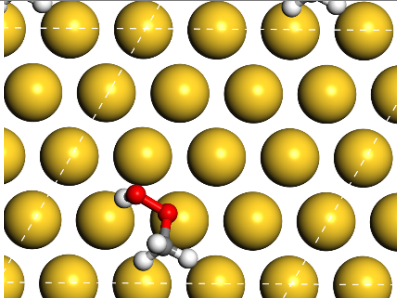
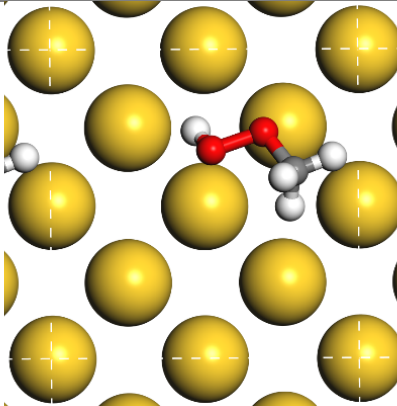
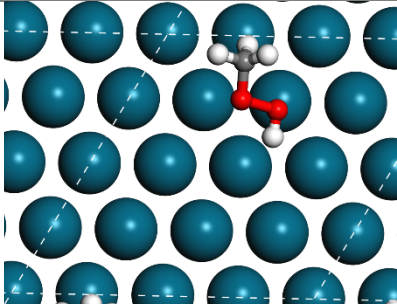
Once formed, the methyl hydroperoxide will need to adsorb and cleave in order to form methanol. In order to understand how the different surfaces, activate the methyl hydroperoxide, different adsorption configurations of the primary intermediate were adsorbed on the four surfaces and the energy barrier for the cleavage of the O—O bond was studied.

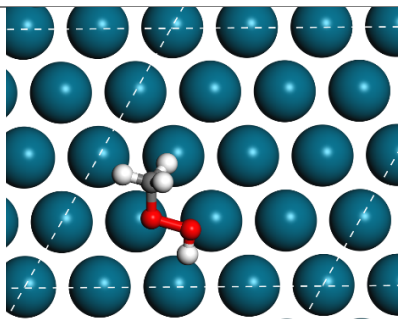
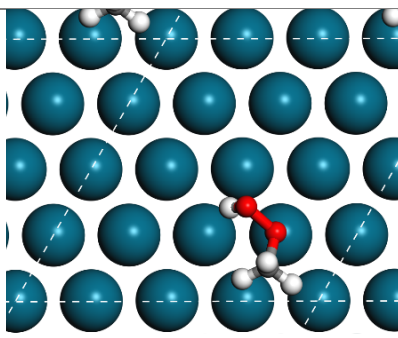
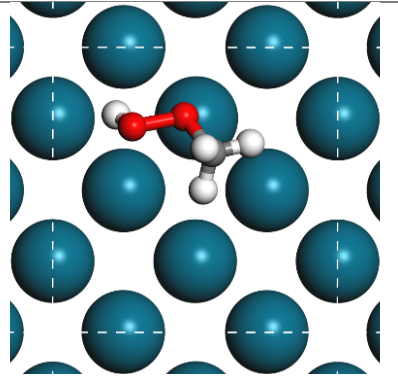
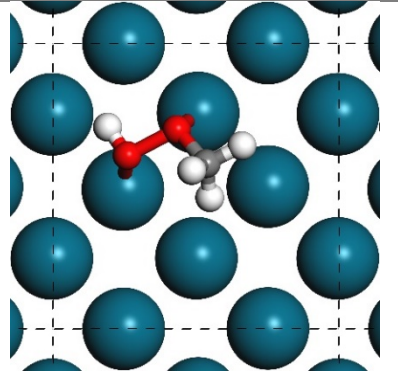
We started by examining top-top configurations as these have been previously suggested to be the most likely mode of adsorption of the methyl hydroperoxide on the alloy surface²⁹. However, difficulties are encountered as the O—O bond distance is much smaller than the Pd—Pd (~2.7 Å) and the Au—Au (~2.9 Å) bond distance. Indeed, in most of the adsorption simulations, there was a slight increase in the O—O bond distance upon adsorption when compared with the distance in the gas phase. The closest orientation that could be obtained for a top-top configuration was obtained on the Pd(100) surface. In that case, the O—O bond distance was increased to 1.55 Å upon optimisation. Another interesting observation is that upon optimising bridge-bridge or hollow-hollow configurations, one of the oxygen atoms switched into a top configuration and thus it was impossible to obtain configurations where at least one of the oxygen atoms is not in a top position. It is also evident that the location of the adsorbate has very little effect on the adsorption energies. In most cases, as long as one of the oxygens is on top of a metal atom, the adsorption energies are similar. The different configurations are shown in table 3.12. In order to avoid interactions between the adsorbates in the periodically repeated slabs in the x- and y-directions, the configurations shown in table 3.12 for the (100) surfaces were reoptimised on the 90-atom slab. On the Au(100) surface, there is very little variation in the adsorption energy

of the methyl hydroperoxide which changes from $-55.5 \text{ kJ mol}^{-1}$ on the 40-atom slab to $-56.0 \text{ kJ mol}^{-1}$ on the 90-atom slab indicating that there were no periodic interactions on the 40-atom slab. However, the difference in adsorption energy of the cleaved structure is more prominent with the adsorption energy changing from $-180.1 \text{ kJ mol}^{-1}$ on the 40-atom slab to $-193.4 \text{ kJ mol}^{-1}$ on the 90-atom slab; a difference of about 13 kJ mol^{-1} . The barrier for the cleavage of the methyl hydroperoxide also changes from $+29.7 \text{ kJ mol}^{-1}$ to $+23.1 \text{ kJ mol}^{-1}$. The same was then repeated on the 90-atom Pd(100) surface. However, upon optimisation, the top-top configuration shown in table 3.12 cleaves thus preventing us from calculating an adsorption energy for the structure. Thus, for the sake of consistency, the data on the 40-atom surface is reported below. The effect of periodic interactions between the adsorbates in the periodically repeated slabs is explored further in section 3.4.5.

According to figure 3.1, the methyl hydroperoxide intermediate will need to cleave on the surface in order to form methanol. Therefore, the cleavage of the O—O bond of the methyl hydroperoxide on the four surfaces was studied.

Table 3.12: The adsorption of the methyl hydroperoxide on the different surfaces.
 (Colour code: Gold: Au, Blue: Pd, Red: O, Grey: C, and White: H)

| Au(111) adsorption sites | $E_{ads} / \text{kJ mol}^{-1}$ | Au—O/ Å | Configuration |
|---------------------------|--------------------------------|---------|--|
| Bridge-Top | -52.5 | 2.771 |  |
| Hollow-Top | -53.1 | 2.864 |  |
| Au (100) adsorption sites | | | |
| Hollow-Top | -55.5 | 2.747 |  |
| Pd (111) adsorption sites | | | |
| Top-Bridge | -69.3 | 2.308 |  |

| | | | |
|----------------------------------|-------|-------------|---|
| Bridge-Top | -66.1 | 2.574 |  |
| Hollow-Top | -70.0 | 2.409 |  |
| Pd (100) adsorption sites | | | |
| Hollow-Top | -68.5 | 2.344 |  |
| Top-Top | -69.8 | 2.360-2.399 |  |

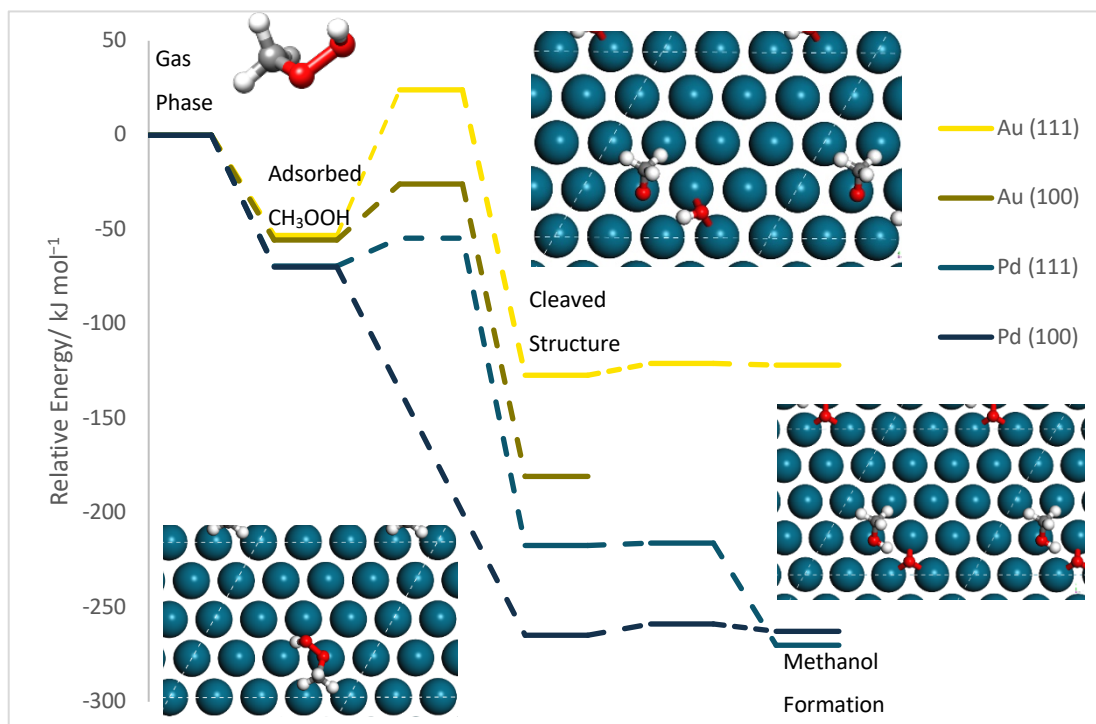


Figure 3.19: Potential energy landscape for the cleavage of the methyl hydroperoxide on the different surfaces followed by hydrogen transfer to form methanol relative to the methyl hydroperoxide in gas phase. (Colour code: Blue: Pd, Red: O, Grey: C, and White: H)

As shown in figure 3.19, the methyl hydroperoxide cleaves without an activation barrier upon adsorption on the Pd (100) surface *i.e.* dissociative adsorption, which is probably due to the top-top configuration obtained for the Pd(100) surface whereby the interaction of both oxygen atoms with the surface results in an immediate cleavage of the intermediate. The barrier for the cleavage of the adsorbate on the Pd (111), Au(111), and Au(100) was found to be 14.7 kJ mol^{-1} , 77.1 kJ mol^{-1} , and 29.6 kJ mol^{-1} respectively, which agrees well with the results obtained for the adsorption of the methyl hydroperoxyl radical on the different surfaces whereby the Pd surfaces strongly activate the intermediate resulting in its cleavage.

In order to form methanol, there would need to be a hydrogen transfer from the hydroxyl radical left on the surface to the methoxy radical. This is also likely to take place from water molecules surrounding the slab. In order to determine the facility of this step, NEB calculations were performed in order to determine the energy barrier. The barriers for the hydrogen transfer step for the Au (111), Pd (111), and Pd (100) were found to be 6.3 , 1.3 , and 6.0 kJ mol^{-1} . These small barriers for the hydrogen protonation

along with the energy barriers for the cleavage step conclusively prove that once the methyl hydroperoxide intermediate is formed, the process of methanol formation is spontaneous on the Pd surfaces. As for the Au (100) surface, it was impossible to model the energy barrier for the hydrogen transfer step as the optimisation of structure **8** (CH₃OH & O) resulted in the immediate transfer of the hydrogen back to the oxygen atom regenerating the hydroxyl radical.

The high energy barrier observed for the cleavage of the methyl hydroperoxide on the Au(111) surface along with the inability of the methoxy radical to abstract a hydrogen from the hydroxyl radical on the Au(100) surface suggest that Au is not a good catalyst for this step.

3.4.5 Role of the oxygen atom on the surface

Upon the formation of methanol, an oxygen atom is left on the surface as shown in figure 3.19. Since an oxygen atom binding on the surface has been shown to be a good candidate for hydrogen abstraction from methane on the Pd surfaces (section 3.4.3), we were interested in investigating whether this is the case on the Au surfaces as well.

Optimised structures of (CH_4 & O) and ($\bullet\text{CH}_3$ & OH) were, therefore, modelled on the Au surfaces. On the Au (111) surface, the preferred mode of adsorption for the oxygen atom was a hollow position whereby each oxygen atom was binding to three Au atoms. In the case of the (100) surface however, the hollow position obtained on the Pd(100) surface was unattainable; hollow oxygen configurations switched to bridge upon optimisation. In both cases, the methane was in a top position with very minimal interaction with the surface.

NEB calculations for the hydrogen abstraction step were then run and the activation energy barriers were computed. As observed on the Pd(111) surface, the oxygen atom in a hollow position on the Au(111) surface had to move to a bridge position in order to abstract a hydrogen from methane. This movement of the oxygen atom from a hollow to a bridge position resulted in a significant increase in the height of the energy barrier. Since the oxygen atom adsorbed on the Au(100) surface was already in a bridge position, the barrier on the Au (100) surface is the smallest amongst all four surfaces. Figure 3.20 shows the energy barriers for methane activation by oxygen on all four surfaces.

The barriers for the hydrogen abstraction from methane by an oxygen atom for the Au (111), Au (100), Pd (111) (sect. 3.4.3), and Pd (100)(sect. 3.4.3) were found to be 92.8 kJ mol^{-1} , 60.5 kJ mol^{-1} , $123.0 \text{ kJ mol}^{-1}$, and 83.7 kJ mol^{-1} respectively. As observed with the Pd(100) surface in section 3.4.3, it is a less activated process for an oxygen atom to abstract a hydrogen from methane on the Au(100) than it is for a hydroxyl radical. From a kinetics point of view, this means that oxygen on its own could be used to activate methane provided that the O–O bond cleaves on the surfaces to form oxygen atoms bound to surface. However, since no products were observed experimentally when molecular oxygen was used on its own without hydrogen peroxide, this means that either molecular oxygen does not cleave in the early phase of the reaction or that it rapidly cleaves forming an oxidised surface. In fact, as discussed in section 3.5, both scenarios are likely, depending on the surface. On Pd (100), the barrier for oxygen

cleavage is too small (8.9 kJ mol^{-1}) which means that the surface will be rapidly oxidised leaving no vacant sites on which methane can adsorb. On the Au surfaces, the low affinity to molecular oxygen will hinder its adsorption on the surface preventing the formation of oxygen-atom species bound to the surface.

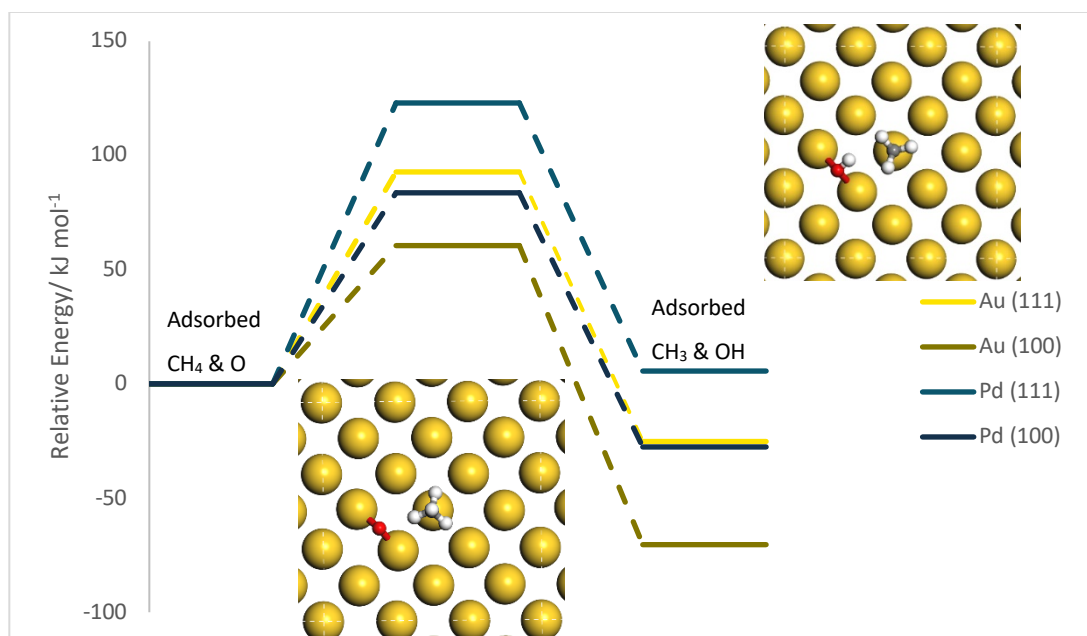


Figure 3.20: Potential Energy landscape for the activation of methane by an oxygen atom relative to the adsorbed methane and oxygen on the respective surfaces. (Colour code: Gold: Au, Red: O, Grey: C, and White: H)

3.4.6 Effect of periodic interactions on adsorption energies and activation barriers

As discussed in section 3.2, two different (100) surfaces were used in this study. For adsorbates as small as hydrogen peroxide, the 40-atom surface was enough to avoid any Van der Waal interactions between the periodically repeated regions of the slab surfaces in the x- and y- directions. This, however, was not the case for calculations where more than one species are interacting on the surface and thus a switch from a 40-atom surface to a 90-atom surface was made.

Since calculations run on the 90-atom surface were computationally demanding, we decided to first run the calculations using the 40-atom surface and then use the optimised structures on the 90-atom surface. This was particularly useful in determining transition states as it allowed us to take the structure of the transition state on the 40-atom surface and then use the dimer method in order to find the structure of the transition state on the 90-atom surface with substantially less computational resources. This is because a 10-image NEB calculation requires at least 5 nodes of 40 cores each, whereas with a dimer that already has a good guess of the transition state, only 2 nodes would suffice. In this section, we compare the results obtained for both slabs in order to quantitatively determine the effect of the interaction of the adsorbates between the periodically repeated slabs.

Figure 3.21 shows the adsorption of a methane and a hydroxyl radical on a 40-atom and a 90-atom Pd(100) surface. The hydrogen atom of the hydroxyl radical in figure 3.21(a) is only 3.967 Å away from one of the hydrogen atoms of the methane molecule in the slab right adjacent to it and thus opens the possibility of Van der Waal interactions between the two species. This, however, is no longer a problem on the 90-atom surface as the methane molecule in the adjacent slab is at least 7.633 Å away.

One interesting observation made is that the switch between the two surfaces had very little effect on the geometry. For example, the distance between the hydrogen atom of the methane molecule pointing towards the oxygen and the oxygen of the hydroxyl radical changed from 2.408 Å to 2.410 Å only upon switching from the 40-atom surface to the 90-atom surface; a difference in the third decimal place.

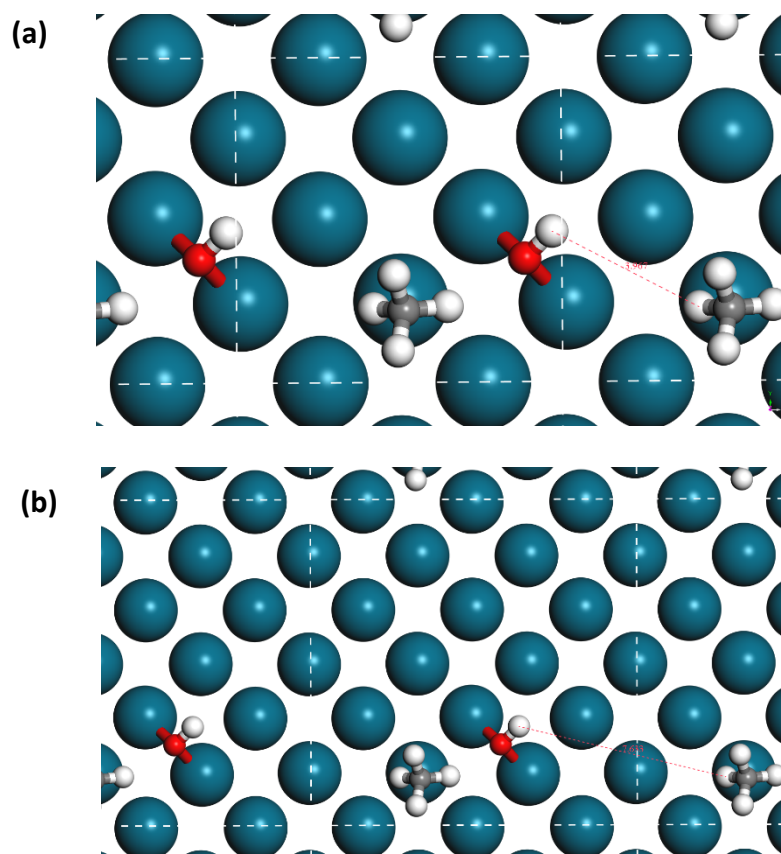


Figure 3.21: Adsorption of methane and a hydroxyl radical on (a) 40-atom (100) surface (b) 90-atom (100) surface. (Colour code: Blue: Pd, Red: O, Grey: C, and White: H)

The difference in adsorption and activation energy, however, was more prominent. Table 3.13 shows the difference in the adsorption energies and the activation energies for the hydrogen abstraction from methane between the two slabs. In both, the energy of adsorption of the starting point and the transition state, the structures are more stabilised by the 90-atom surface with an energy difference of 8.5 kJ mol⁻¹ and 17.7 kJ mol⁻¹ respectively. This means that, the smaller surface overestimates the energy barrier for hydrogen abstraction from methane by 9.2 kJ mol⁻¹.

Table 3.13: Energy of adsorption of the starting point ($E_{ads}SP$) of the NEB (methane and hydroxyl radical) and the transition state ($E_{ads}TS$) along with the energy barrier ($E_{AH_{abs}}$) for methane activation by a hydroxyl radical.

| Surfaces | $E_{ads}SP$ / kJ mol^{-1} | $E_{ads}TS$ / kJ mol^{-1} | $E_{AH_{abs}}$ / kJ mol^{-1} |
|--------------------------------|---------------------------------------|---------------------------------------|--|
| 40-atom Pd(100) surface | -320.2 | -222.9 | +97.3 |
| 90-atom Pd(100) surface | -328.7 | -240.6 | +88.1 |

Whilst the energy difference is not huge, it is still significant and should not be ignored as it would result in the misinterpretation of the data between the (111) and the (100) surfaces. For example, the energy barrier for hydrogen abstraction from methane on the Pd(111) surface is 93.9 kJ mol^{-1} which is less than the barrier for hydrogen abstraction on the 40-atom Pd(100) surface. This might lead us to think that hydrogen abstraction is easier on the (111) surface; this is however not the case as evidenced by the data in table 3.13.

The data in table 3.13 were obtained using a $3 \times 3 \times 1$ K -points mesh for both surfaces. However, it is important to note that large surfaces normally require a smaller K -points mesh and thus the difference in adsorption and activation energies between the two surfaces shown in table 3.13 is not only a result of the periodic interactions but also partly due to the size of the K -points mesh used which affects the accuracy. In order to quantify this, the adsorption of methane and the hydroxyl radical and the pure surface was optimised using a smaller $1 \times 1 \times 1$ K -points mesh, and the adsorption energy was computed. The energy of adsorption changed from $-328.7 \text{ kJ mol}^{-1}$ to $-326.7 \text{ kJ mol}^{-1}$; a difference of only 2 kJ mol^{-1} or 0.02 eV . Thus, about 2 kJ mol^{-1} of the overestimated 9.2 kJ mol^{-1} energy barrier is due to the use of the same size of K -points for the two surfaces.

3.5 Conclusions

In this chapter, we investigated the performance of Au and Pd surfaces for the partial oxidation of methane to methanol using hydrogen peroxide and molecular oxygen as oxidants. We studied the performance of the surfaces at each of the steps of the reaction mechanism proposed by the experimental group in order to rationalise why the monometallic catalysts are not active for this reaction whilst the colloids Au-Pd alloy nanoparticles are.

Calculations of adsorption energies of intermediary species and activation barriers for the different steps of the reaction mechanism show that both metals struggle at forming the primary intermediate in this reaction: methyl hydroperoxide. Whilst both metals have no problem activating hydrogen peroxide and methane, once molecular oxygen is introduced the reaction mixture, the reaction comes to a halt. On the Pd surfaces, the affinity for molecular oxygen is so high that once oxygen is introduced into the reaction mixture, the cleavage of molecular oxygen is expected to happen resulting in the formation of an oxidised surface, which since oxygen is more soluble in water than methane, is expected to happen even prior to methane activation, leaving no vacant sites on which the methyl radical can adsorb. On the other hand, with the Au(111) surface, oxygen adsorption is endothermic and thus, even though the methyl radicals do form on the surface, the displacement of water by molecular oxygen is hindered by the endothermic nature of oxygen adsorption. The displacement of water by oxygen on the Au(100) surface is slightly exothermic but the formation of the methyl peroxy radical is hindered by the high energy barrier of the reaction of the methyl radical with molecular oxygen. With this background to the difficulties associated with the use of the pure metals, we now explore the doped systems in the next chapter.

Chapter 4 Doped Au and Pd Surfaces

The aim of this chapter is to use doped Au and Pd surfaces in order to demonstrate how the alloy is likely to tackle the difficulties encountered with the monometallic surfaces which have been highlighted in chapter 3. We study the adsorption and cleavage of molecular oxygen on the Pd surfaces in order to determine whether the presence of a single Au atom in a Pd environment can reduce the activity of the surface. We then study the effect of the dopant on the formation of the methyl peroxy radical.

4.1 Introduction

As discussed in the introductory chapter, Au-Pd alloy nanoparticles have been shown to be effective catalysts for many reactions including: the direct synthesis of hydrogen peroxide^{86, 26}, oxidation of primary alcohols to aldehydes²⁷, oxidation of glycerol⁸⁷, and oxidation of cyclohexane to cyclohexanol⁸⁸.

In these studies, the bimetallic catalysts demonstrate a superior activity when compared with the monometallic catalysts. For example, in a study by Edwards *et al.*⁸⁶ on the direct synthesis of hydrogen peroxide from hydrogen and oxygen using support Au-Pd catalysts, the alloy has demonstrated a far superior activity for the production of hydrogen peroxide than the pure monometallic catalysts. In this study, carbon was investigated as a support for the alloy after having examined other supports such as titania, alumina, and iron oxide (section 1.3.1). In the case of the pure 5 wt% Au catalyst supported on carbon, hydrogen peroxide was produced but at low rates, not enough to determine the hydrogen selectively to an accurate level. The pure 5 wt% Pd catalyst was significantly more active than the pure Au catalyst with a hydrogen peroxide formation rate of $55 \text{ mol h}^{-1} \text{ kg}_{\text{cat}}^{-1}$ (vs. $1 \text{ mol h}^{-1} \text{ kg}_{\text{cat}}^{-1}$ for the pure Au) and a hydrogen selectivity of 34%. However, the addition of Pd to Au to give a catalyst comprising of 2.5 wt% of each of Au and Pd resulted in a significant increase in the catalytic performance of the synthesis of hydrogen peroxide with the rate of formation doubling in magnitude from $55 \text{ mol h}^{-1} \text{ kg}_{\text{cat}}^{-1}$ to $110 \text{ mol h}^{-1} \text{ kg}_{\text{cat}}^{-1}$ and a hydrogen selectivity of 80%. The rate of hydrogen peroxide formation was also significantly higher than that observed using the other supports discussed in section 1.3.1.

In studies that have examined the performance of both the alloy and the monometallic catalysts, the monometallic catalysts were active for the reaction but with the alloy exhibiting an enhanced catalytic performance. However, in the work of Agarwal *et al.*³¹

on the partial oxidation of methane to methanol using hydrogen peroxide and molecular oxygen as oxidants, the monometallic catalysts showed no activity for methane oxidation at all thus suggesting that the bimetallic colloidal NPs are the active catalyst for this reaction.

In chapter 3, we provided a detailed explanation on how the monometallic catalysts fail at producing the primary intermediate (methyl hydroperoxide) observed experimentally. In this chapter, we explore the effect of doping the modelled pure surface on the reaction mechanism in order to understand how the alloy catalyses this reaction.

4.2 Computational Details and Methodology

All calculations used the plane wave DFT methods discussed in chapters 2 and 3. To form the doped surfaces, the pure (111) and (100) surfaces of Au and Pd that were modelled for chapter 3 were used. The doped surfaces were formed by replacing one of Au/Pd atoms in the top layer by a Pd/Au atom. Due to symmetry, all the atoms in the top layer are equivalent and thus the choice of which atom to replace is of little significance.

Once replaced, the surfaces were optimised using the VASP code. The convergence criterion for the energy cut off and the electronic self-consistent field (SCF) threshold was set to 400 eV and 10^{-4} eV respectively. Calculations were set to converge when the forces are less than $0.001 \text{ eV \AA}^{-1}$ for the surfaces and 0.01 eV \AA^{-1} for the adsorption calculations. Dispersion corrections were included to account for van der Waals interactions using Grimme's empirical DFT -D3 model. Dipole correction along the z-direction (perpendicular to the surface) of the slab was also applied in all calculations.

Like the pure surfaces, the bottom three layers were fixed with the top two layers free to move. In order to avoid interactions between the periodically repeated slabs, a vacuum layer of 13 \AA is introduced above the surface. A Monkhorst-Pack grid of $3 \times 3 \times 1$ was used to sample the Brillouin zone. Figure 4.1 shows the optimised Au-doped Pd(111) (4.1(a)) and the Pd-doped Au(100) (4.1(b)) surfaces that were modelled. Since the atomic radius of Au is greater than Pd, the Au atom in the Au-doped Pd(111) surface takes up more space and thus appears to be higher than the surrounding Pd atoms.

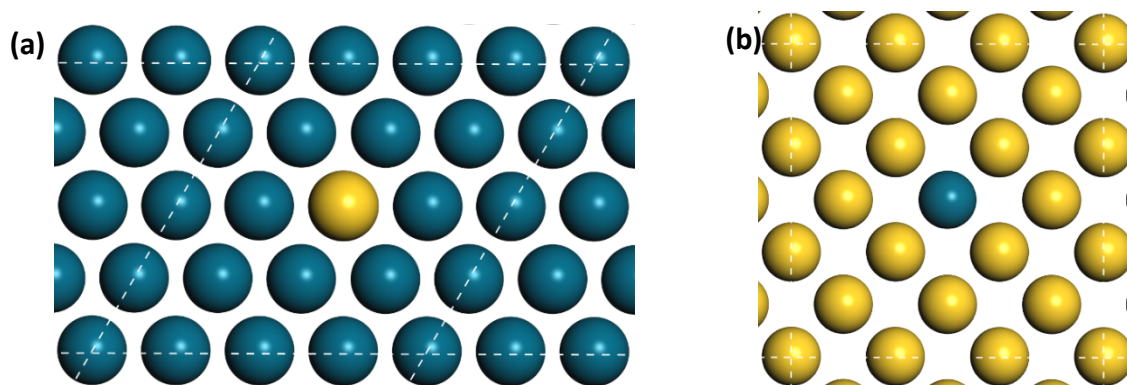


Figure 4.1: Optimised (a)Au-doped Pd(111) surface and (b)Pd-doped Au(100) surface.

(Colour code: Blue: Pd, and Gold: Au)

In order to then understand the effect of the dopant on the reactivity of the two surfaces, the DOS was plotted for the doped surfaces. Figure 4.2 (a) and 4.2 (b) show the DOS plot of the top layer of the Pd-doped Au(111) surface and Au-doped Pd(111) surface. The two plots look very similar in shape to the pure surfaces' plots shown in figure 3.5 in chapter 3. In the Pd-doped Au(111) surface (figure 4.2(a)), an extra peak is observed after the Fermi-level which belongs to the doped Pd atom present on the surface as confirmed by plotting the DOS for the doped atom on its own as shown in figure 4.3. The effect of doping the two surfaces on the d-band centre was also examined. The d-band centre of the Pd-doped Au(111) surface changed from -2.961 eV to -2.813 eV; thus moving closer to the Fermi-level making the surface more reactive. An opposite trend was observed on the Au-doped Pd(111) surface, where the d-band centre changed from -1.497 eV to -1.582 eV thus making the surface less reactive.

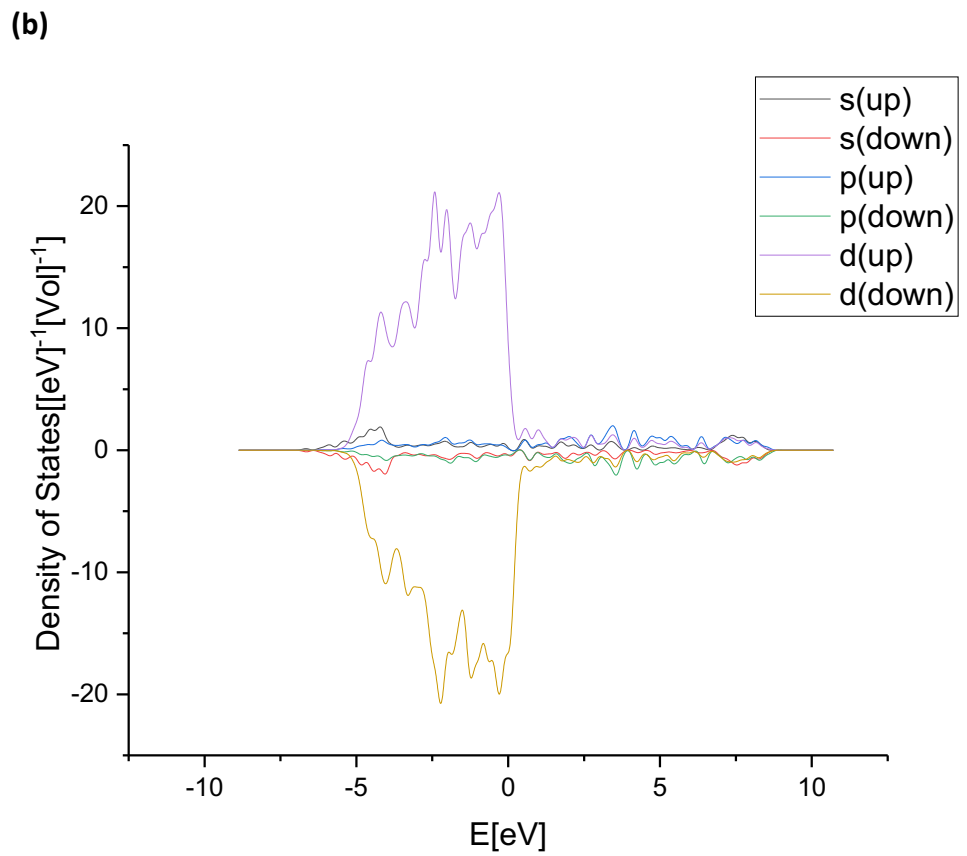
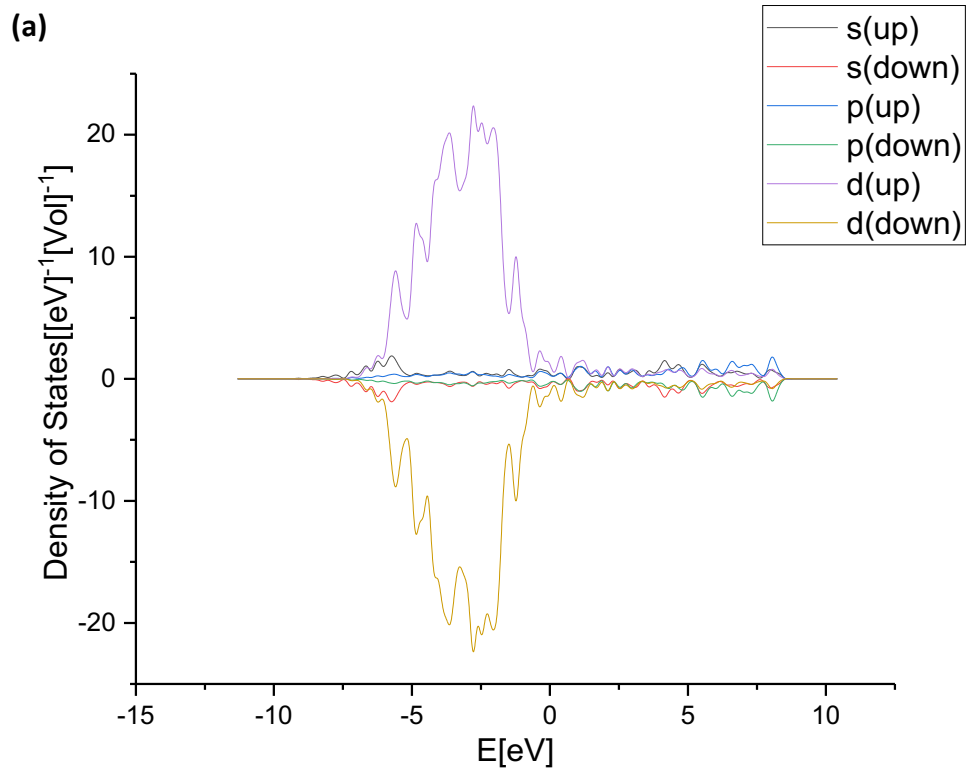


Figure 4.2: DOS plot of (a) Pd-doped Au(111) surface and (b) Au-doped Pd(111)

Surface

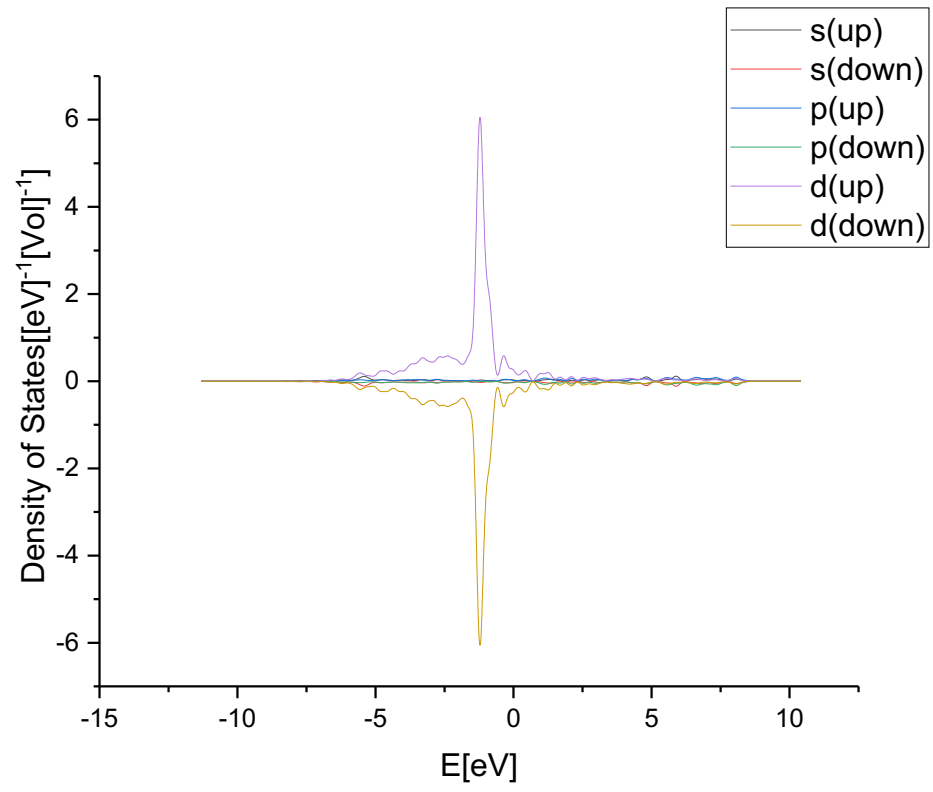


Figure 3.3: DOS plot of the dopant on the Pd-doped Au(111) surface

4.3 Results and Discussion

4.3.1 Oxygen Adsorption and Cleavage

As discussed in chapter 3, the primary issue with the Pd surfaces is their high affinity to molecular oxygen. Thus, it was particularly interesting to study the effect of doping the Pd surfaces with Au on the barrier of the oxygen cleavage.

The adsorption of molecular oxygen on the doped surfaces was first studied. The bridge-bridge configuration of molecular oxygen observed on the pure Pd(100) was maintained but with the oxygen atom preferentially binding to the Pd over the Au (2.087 Å vs 2.407 Å). On the doped Pd(111) surface, two bridge-top configurations were examined: one where the oxygen in the top position is binding to the dopant and a bridge-top configuration where the oxygen in the bridge position is binding to the dopant and a Pd atom. On optimisation, the latter switched to a top-top configuration with both oxygen atoms binding to Pd atoms. The top-top configuration was found to be more stable than the top-bridge configuration by 48.6 kJ mol⁻¹. Table 4.1 shows the adsorption energies of molecular oxygen on the pure and doped Pd surfaces. On both surfaces, the adsorption of molecular oxygen is stronger on the pure surfaces than on the doped surfaces suggesting a decrease in the affinity to molecular oxygen on the Pd surfaces upon doping with Au. An interesting observation is that the adsorption of molecular oxygen in a top-bridge configuration on the doped Pd(111) surface is less stable than the top-top configuration. This suggests that even in a Au-doped environment, the preferred mode of adsorption of molecular oxygen is with Pd.

Table 4.1: Adsorption energy of molecular oxygen on the pure (E_{adsPR}) and doped (E_{adsDP}) surfaces of Pd along with the energy barrier for the cleavage.

| Surface | $E_{\text{adsPR}} /$ kJ mol ⁻¹ | $E_{\text{adsDP}} /$ kJ mol ⁻¹ | O—O barrier / kJ mol ⁻¹ | |
|------------------------|--|--|---------------------------------------|----------------|
| | | | Pd | Au-doped Pd |
| Pd(100) | -176.9 | -127.7 | +8.9 | +18.1 |
| Pd(111) – (bridge-top) | -100.1 | -40.0 | +62.8 | +73.7 |
| Pd(111) – (top-top) | -96.4 | -88.7 | | +122.4 |

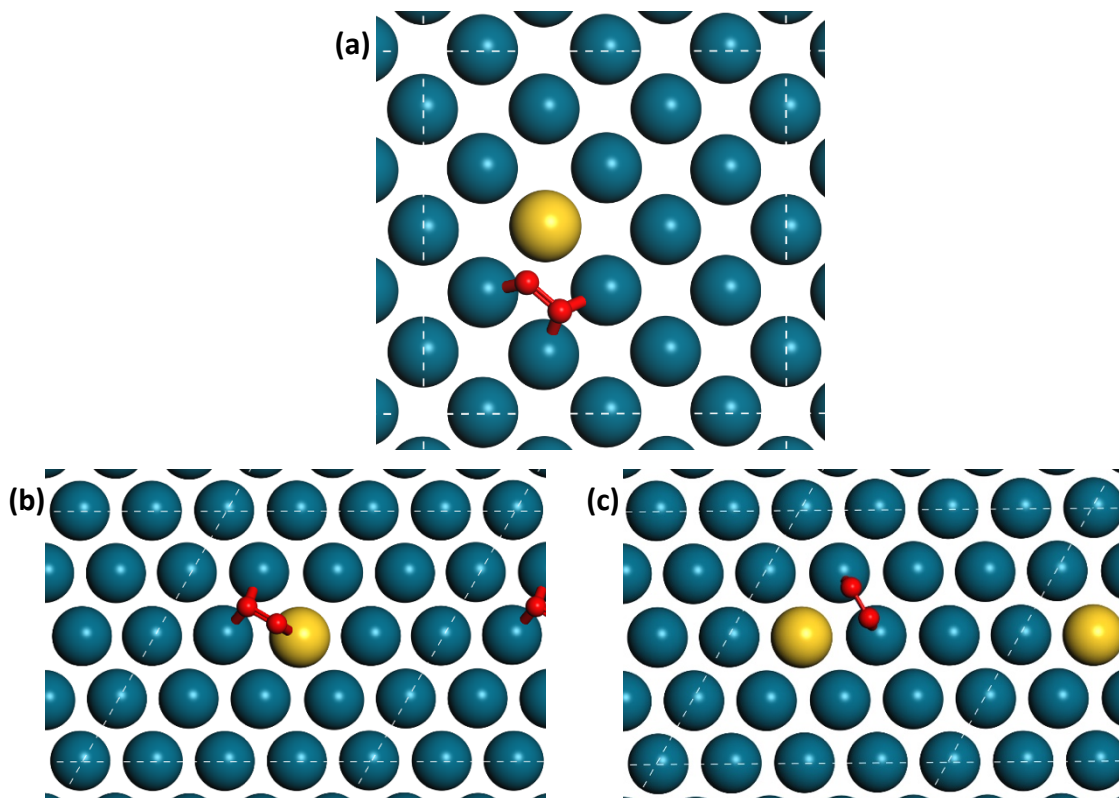


Figure 4.4: Adsorption of molecular oxygen on the Au-doped Pd surfaces in a: (a) bridge-top configuration on the Au-doped Pd(100) surface (b) bridge-top configuration on the Au-doped Pd(111) surface, and (c) top-top configuration on the Au-doped Pd(111) surface. (Colour code: Blue: Pd, Gold: Au, Red: O, Grey: C, and White: H)

Since we are mainly interested in the effect of the dopant atom on the reaction, only reaction barriers that lead to one of the O atoms remaining in contact with the Au dopant in the Pd surfaces have been considered. Thus, the cleaved structure corresponds to the two oxygen atoms binding in a bridge configuration with one of the oxygen atoms binding to the dopant and a Pd atom. This means that for the two adsorption configurations of molecular oxygen on the Pd(111) surface shown in figure 4.4(b) and 4.4(c), the starting point of the MEP is different, but the transition state and the end point is the same.

Based on the adsorption energies and energy barriers, it is evident that doping a Pd surface with Au can strongly influence the reactivity of the surface. The adsorption of oxygen on the pure surface is significantly stronger than on the doped surface with a difference of around 50 kJ mol^{-1} and 60 kJ mol^{-1} for the Pd(100) and Pd(111) surfaces respectively. Due to the significantly higher adsorption energy of the top-top

configuration than the bridge-top, the barrier for the oxygen cleavage on the (111) surface doubles in magnitude from 62.8 kJ mol^{-1} to $122.4 \text{ kJ mol}^{-1}$ which is similar in value to the energy barrier for the formation of methyl peroxy radical ($127.8 \text{ kJ mol}^{-1}$) on the pure Pd(111) surface. An increase of about 10 kJ mol^{-1} for the barrier of the oxygen cleavage is also observed on the Pd doped (100) surface. These results suggest that even the introduction of a single Au atom to a Pd system can decrease the high affinity of the Pd surfaces to molecular oxygen thus decreasing the likelihood of the formation of a PdO surface.

4.3.2 Formation of the Methyl Peroxy Radical

Since the formation of a PdO surface on the (111) surface is now unlikely, we move on to determine the effect of the dopant on the formation of the methyl peroxy radical on the surface. In order to ensure comparability between the barriers on the doped and pure surface, the starting point of the NEB was the same for both transition state calculations whereby the oxygen was in a top-bridge position interacting with three Pd atoms and the methyl was on top of a Pd atom. As shown in figure 4.5, the oxygen on the doped surface is first neighbours with the dopant with the methyl radical being second neighbours with the dopant. This is because as demonstrated in table 3.5 of section 3.4.2, the methyl radical prefers to bind to Pd over Au.

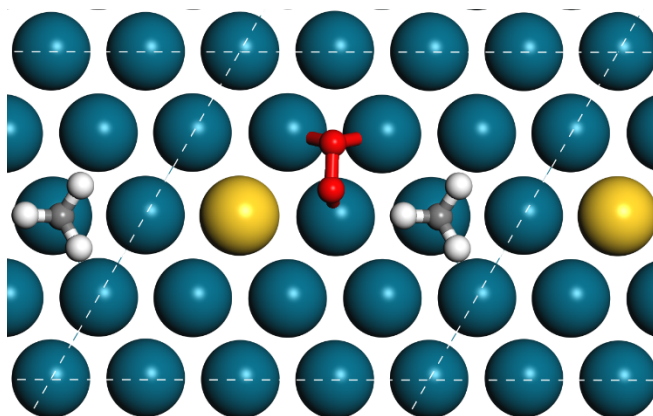


Figure 4.5: The adsorption of the methyl radical and molecular oxygen on the Au-doped Pd(111) surface. (Colour code: Blue: Pd, Gold: Au, Red: O, Grey: C, and White: H)

The dopant had very little effect on the geometry of the transition state as it closely resembled the transition state on the pure surface where the oxygen molecule switched into a top-top position with the carbon of the methyl radical pointing towards the oxygen as shown in figure 3.13 in section 3.4.3. For example, the Pd–C distance of the

methyl radical, changed from 2.315 Å on the pure surface to 2.320 Å on the doped. As for the activation energy, the dopant lowered the energy barrier from +127.8 kJ mol⁻¹ on the pure surface to +119.9 kJ mol⁻¹; a difference of about 8 kJ mol⁻¹. These results highlight the improved reactivity of the doped system, whereby the introduction of a single Au atom has a significant effect on the oxygen cleavage and the formation of the methyl peroxy radical.

The problem encountered with the pure Au(111) surface was the higher affinity of the surface to water over molecular oxygen thus hindering the displacement of water by oxygen on the surface. In order to understand how the alloy would overcome this problem, a Pd-doped Au(111) surface was optimised and the energy of reaction of the displacement of water by molecular oxygen in the presence of a methyl radical was computed. Since we are interested in studying the effect of the doped surface on the water displacement reaction, the methyl radical was on top of a Au atom with the O₂/H₂O directly interacting with the dopant. The top-bridge configuration of molecular oxygen observed on the pure Au(111) surface, with the oxygen in bridge position interacting with both Au and Pd, was optimised. On optimisation, the oxygen in the bridge position moved into a top position thus interacting only with the Pd with the other oxygen atom in a bridge position 2.809 Å away from the Au atom. The optimisation of the (•CH₃& H₂O) was as expected with both species in top positions.

As shown in table 4.2, the effect of doping the Au(111) surface on the adsorption of water and molecular oxygen in the presence of a surface-stabilised methyl radical is significant. Both molecules interact more strongly with the doped surface with molecular oxygen changing from endothermic to exothermic adsorption. This strong interaction of the oxygen with the doped surface results in the reduction of the energy of the displacement reaction from +60.8 kJ mol⁻¹ on the pure surface to +2.20 kJ mol⁻¹ on the doped, which although slightly endothermic, shows a big change caused by only a low concentration of Pd when compared with the pure surface, suggesting that only a modest increase in the Au to Pd ratio is needed in order to shift the equilibrium towards oxygen adsorption.

We next investigate the effect of the Au dopant on the energy barrier for the formation of the methyl peroxy radical. Two different transition states were examined: One where the methyl radical attacks the oxygen in bridge position (over a Au atom) and another where the attack happens on the oxygen in top position (over a Pd atom). The barrier

for the latter was found to be 115.6 kJ mol⁻¹, 28.1 kJ mol⁻¹ higher in energy than the transition state where the Pd is not directly participating in the attack (87.5 kJ mol⁻¹). Examining the two transition states reveals that in the configuration involving the attack of the methyl group at the oxygen binding to the Pd, the Pd—O bond was stretched from 2.130 Å to 2.351 Å in order to accommodate the methyl radical, which as a result is less stable. As for the transition state where the dopant is not directly participating in the attack, the binding of the Pd to the oxygen was not affected. Both barriers are higher in energy than that for the pure Au(111) surface (64.0 kJ mol⁻¹), which is expected as the binding of the oxygen to the Pd is stronger than the Au. The 87.5 kJ mol⁻¹ energy barrier, however, is a reasonable compromise to the increased affinity to molecular oxygen as it is only 23.5 kJ mol⁻¹ higher in energy than the pure surface but with an increased affinity to molecular oxygen.

The same process was then repeated for the doped Au(100) surface. Since molecular oxygen adsorbs in a bridge-bridge position on the pure (100) surface, two different configurations were examined on the Pd-doped Au(100) surface for the adsorption of molecular oxygen in the presence of a surface-stabilised methyl radical. The two configurations were identical but with the dopant atom acting as a first and second neighbour to the methyl radical as shown in figure 4.6. The configuration where the methyl radical was adsorbed to a metal atom acting as a first neighbour to the dopant was found to be more stable by 3 kJ mol⁻¹. As shown in table 4.2, in both configurations, the affinity of the surface to both water and oxygen is enhanced, with configuration **(a)** having a higher affinity to molecular oxygen than configuration **(b)**. In both cases, the energy of the reaction for the displacement of water by molecular oxygen is more exothermic than the pure surface.

Table 4.2: ΔE for the displacement of water by molecular oxygen on the pure and doped Au(111) surface

| Surfaces | ΔE_{H_2O} / kJ mol ⁻¹ | ΔE_{O_2} / kJ mol ⁻¹ | $\Delta E_{O_2} - \Delta E_{H_2O}$ / kJ mol ⁻¹ |
|------------------------------------|---|--|--|
| Au (111) | -34.8 | +26.0 | +60.8 |
| Pd-doped Au(111) | -45.6 | -43.4 | +2.20 |
| Au(100) | -34.2 | -37.5 | -3.3 |
| Pd-doped Au(100) (Fig 4.6a) | -47.3 | -58.4 | -11.1 |
| Pd-doped Au(100) (Fig 4.6b) | -47.3 | -55.4 | -8.2 |

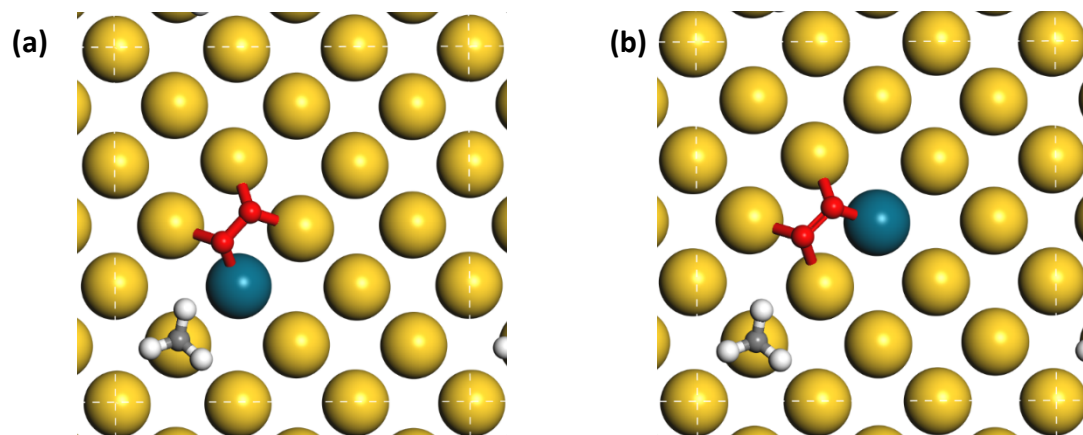


Figure 4.6: Adsorption of the methyl radical and molecular oxygen on the Pd-doped Au(100) surface: (a) dopant acting as a first neighbour to the methyl radical (b) dopant acting as a second neighbour to the methyl radical. (Colour code: Blue: Pd, Gold: Au, Red: O, Grey: C, and White: H)

In order to study the effect of the dopant on the formation of the methyl peroxy radical, two different NEB calculations were performed with each of the configurations in figure 4.6 acting as starting points. Interestingly, the energy barrier for the formation of the methyl peroxy radical with structure **(b)** as a starting point ($106.0 \text{ kJ mol}^{-1}$) was found to be similar to the value obtained on the pure surface ($105.2 \text{ kJ mol}^{-1}$). An improved lower energy barrier of 91.5 kJ mol^{-1} was found when using structure **(a)** as a starting point. In order to rationalise the difference in the two energy barriers, the geometries of both transition states were examined (figure 4.7). In the transition state corresponding to structure **(a)**, the methyl radical was only 2.260 \AA away from the dopant and thus was strongly stabilised by it. As for the transition state of structure **(b)**, the methyl radical was slightly stabilised by the Au with a bond distance of 2.460 \AA . Since Pd is better at stabilising the methyl radical than Au as shown in chapter 3, the transition state where the methyl radical is interacting with the dopant is lower in energy.

These results strongly demonstrate the role played by both metals in the alloy. Once Au decreases the high affinity of the Pd surfaces to molecular oxygen, the high barriers for the production of the methyl peroxy radical are then reduced by Pd doping. Once generated, the methyl peroxy radical can then easily form the methyl hydroperoxide intermediate which as demonstrated earlier can then be converted to methanol effortlessly, which is in agreement with previous studies on the oxidation of cyclohexane to cyclohexanol via a cyclohexyl hydroperoxide intermediate where they described the role of the Au catalyst as a promoter for the production of the cyclohexyl hydroperoxide rather than as a catalyst that aids in its conversion to cyclohexanol^{189 30}.

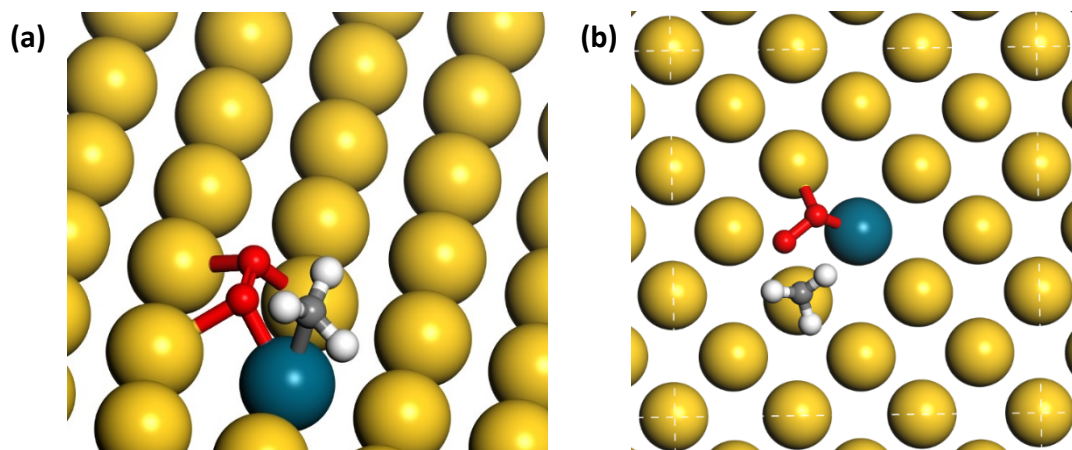


Figure 4.7: Geometry of the transition states of structure (a) and structure (b) of figure 4.6

4.4 Conclusions:

In this chapter, we have rationalised how the alloy catalyses the partial oxidation of methanol to methanol. The Au acts as a promotor for the production of the methyl peroxy radical by decreasing the affinity of the Pd surfaces to molecular oxygen thus preventing the formation of a PdO surface. With a decrease in the affinity to molecular oxygen, the Pd surfaces can then promote the reaction of the methyl radical and molecular oxygen thus allowing the formation of the methyl peroxy radical. Once formed, the formation of the methyl hydroperoxide and its subsequent conversion to methanol can then easily be accomplished.

Chapter 5 DFT-assisted Spectroscopic Studies on the Coordination of Small Ligands to Palladium: From Isolated Ions to Nanoparticles

This chapter concerns the use of nitrogen and oxygen containing compounds as capping agents for the synthesis of Pd nanoparticles. A brief introduction on the use of capping agents in metal-nanoparticle synthesis is first presented, followed by computational details of the different surfaces, and finally a thorough review and analysis of both computational and experimental results is given. The chapter summarises a collaboration with multiple groups. The experimental work was performed by a group at the Università degli Studi di Milano whilst the computational work was performed at Cardiff University. The non-periodic atom-centred simulations were performed by Cameron Beevers, whilst the present author performed the plane wave DFT calculations. For the sake of coherency and completeness, all the results are included here.

5.1 Introduction

5.1.1 Stabilisation of Metal Nanoparticles:

The unique physical properties of metal nanoparticles (MNPs) have made them intensively studied over the past few decades. Depending on their physical properties, MNPs can be used in optics, electronics, magnetics, biosensors, and catalysis⁹⁰. These properties depend on structural and morphological parameters such as composition, particle size, crystal structure, exposure of facets, and the environment⁹¹.

The size of MNPs can vary from small clusters containing tens of atoms to large clusters containing several thousand metal atoms⁹². The synthesis of colloidal nanoparticles is typically achieved in solution by reacting metal precursors with reducing agents.⁹³ However, as a result of their high dispersed states, MNPs in solution tend to agglomerate and coagulate and thus require stabilisation, which is normally achieved via either immobilisation on a support or capping in an organic ligand shell⁹⁴.

In many cases, the use of transition-metal nanoparticles in the field of catalysis relies on a solid support to which the nanoparticle either binds mechanically or chemically to its surface. This solid support, in return, guarantees a simple separation of products from the catalyst and prevents the degradation of the nanoparticles. However, the presence

of a support also means that turnover rates and selectivity can be negatively impacted. As a result, stabilisation using an organic ligand shell provides a better alternative⁹⁵. Capping agents such as surfactants, organic molecules, polymers, dendrimers, cyclodextrins, and polysaccharides have all been used for metal nanoparticles synthesis⁹⁴. Ammonium containing surfactants such as Aliquat 336 (tetra-*n*-octylammonium chloride) and CTAB (Cetrimonium bromide) are normally used to cap metal nanoparticles (Figure 5.1). The agglomeration of the metal is prevented using a combination of electrostatic and steric effects, which is normally achieved by having the charged nanoparticle surface surrounded by the negatively charged halide ions which are in turn surrounded by the positively charged ammonium groups thus ensuring electroneutrality (Figure 5.1(b))⁹⁶.

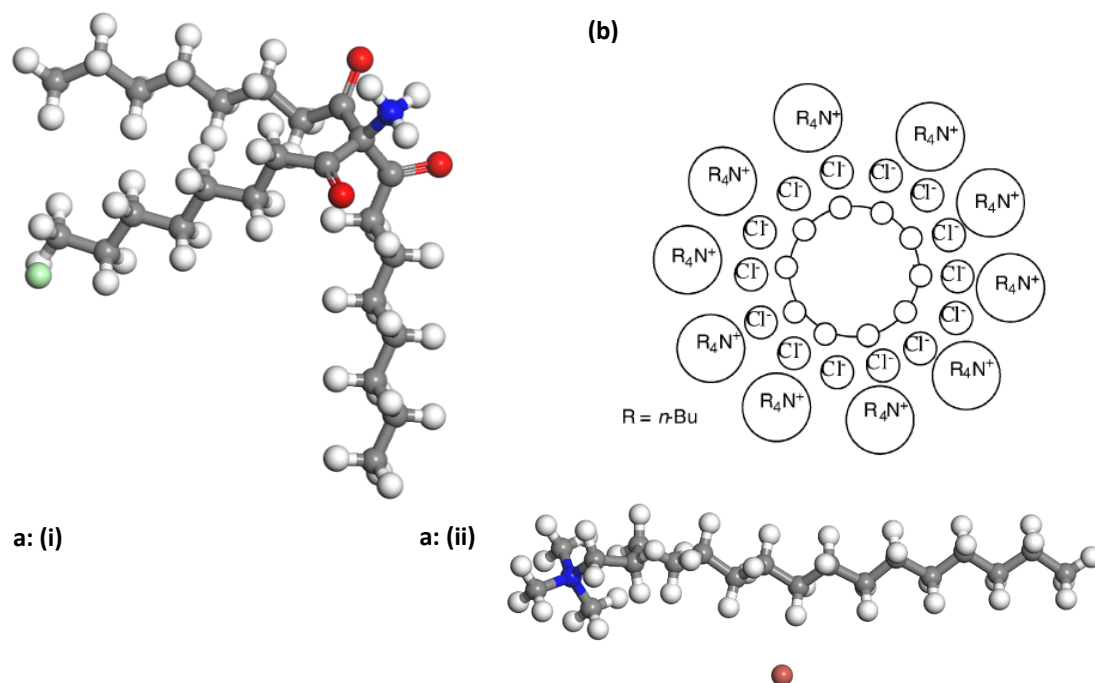


Figure 5.1: Examples of surfactants used as capping agents (a): (i) Aliquat 336 (ii) CTAB (b) Charge distribution in surfactant-stabilised nanoparticles (taken from reference number 97)⁹⁷

Colour code: C: grey, N: blue, H: white, O: red, Cl: green, and Br: red

Stabilisation can also be achieved using polymers and dendrimers. Polymers such as poly(*N*-vinyl-2-pyrrolidone) (PVP) and poly(vinyl alcohol) (PVA) and dendrimers such as poly-(amidoamine) (PAMAM) and poly(propylene imine) (PPI) are widely used to protect metal nanoparticles.⁹⁶

Another important group of capping agents that is frequently used for the synthesis of metal nanoparticles is based on hetero-atom containing ligands. Ligands containing atoms such as sulphur (thiols), phosphorus, and nitrogen (amines) have lone pairs which result in strong binding to metal nanoparticles (Figure 5.2)⁹⁶.

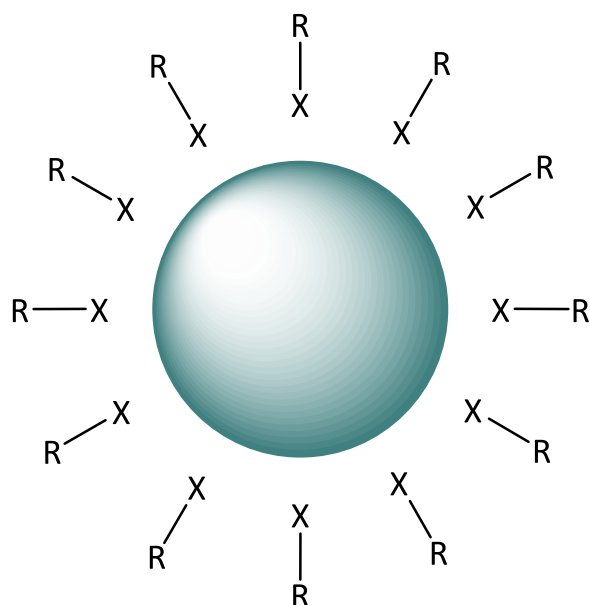


Figure 5.2: Stabilisation of metal nanoparticles using hetero atom containing ligands⁹⁶

Code: Pd: Green, hetero atom (N, S, P): X, R group: R

Since the focus of this chapter is mainly nitrogen containing ligands, these will now be discussed in greater detail.

Oleyamine is one of the main nitrogen-containing ligands used for the stabilisation of Pd nanoparticles⁹⁸. It is often used in its pure form but can also be used in combination with other surfactants.⁹⁵ Hu *et al.* generated Pd nanoparticles of different shapes (spheres, tetrahedra, and multipods) by using oleyamine combined with alkylammonium alkylcarbamate (AAAC) to reduce Pd(II) acetylacetonate ($\text{Pd}(\text{acac})_2$) with a borane-tert-butylamine complex⁹⁹.

Other types of nitrogen-containing ligands have also been used, including: primary amines¹⁰⁰, aromatic amines¹⁰¹, pyridyl groups, imidazole derivatives¹⁰², and porphyrins¹⁰³.

5.1.2 Effect on Catalysis

Transition metal nanoparticles such as Au and Pd, are crucial in the field of catalysis as they effect metal surface activation at a nanoscale level thus allowing control over efficiency and selectivity of heterogenous catalysis⁹². However, since these nanoparticles need to be stabilised by capping agents, it is important to ensure that any steric hinderance to the catalytic process resulting from their presence is minimised. Their effect on the catalytic performance of metal nanoparticles has been widely investigated. Since the capping agent normally surrounds the catalyst (as shown in figures 5.1 and 5.2), the access of the reactants to the surface of the catalyst is thus hindered⁹⁴.

Li *et al.* studied the effect of surfactant removal on the electrocatalytic performance of Pt nanoparticles¹⁰⁴. The group employed different methods (UV-Ozone irradiation, acetic acid washing, and thermal annealing) to remove oleyamine from Pt nanoparticles. The resultant nanoparticles were then used to catalyse the reduction of oxygen to water. Thermal annealing was found to be the most effective surfactant removal method, as it did not result in any structural or morphological changes of the nanoparticle. The electrocatalytic activity was also found to be strongly dependent on the surfactant removal method employed. Based on polarisation curves and Tafel plots, the thermal annealing method had the highest Oxidation Reduction Reaction (ORR) activity.

Other studies have shown the ability of capping agent molecules to create a metal-ligand interphase resulting in diffusional, steric, and electronic effects that can alter the activity and selectivity of catalytic reactions^{91,94}.

The presence of an organic shell generated by surfactants introduces two different types of interfaces: (i) An interface between the metal and the ligand (a metal-ligand interface) (ii) An interface between the ligand and the solution (a ligand-solution interface). Since there is no distinct border between the two interfaces, an intermixed interface may form and is known as metal-ligand interphase, which can affect different mechanistic aspects such as charge transfer, chirality, adsorption geometry, steric hindrance, and molecular recognition⁹⁴.

In this study, a combination of UV-Visible (UV-Vis.) spectroscopy, Fourier transform infrared (FT-IR) spectroscopy and Density Functional Theory (DFT) modelling is

employed to investigate the coordination of small ligands (diols and amino alcohols) to Pd^{2+} ions and Pd nanoparticles. The combined use of spectroscopic techniques and theoretical modelling has already been proven to be a powerful tool to study metal-ligand interactions in Au and Ag nanoparticles^{105,106,107}.

The aim of the study is to compare the binding interactions exhibited by amino and hydroxyl groups to Pd nanoparticles. Molecules such as 3-Aminopropan-1-ol have more than one heteroatom, so the capping agent is likely to bind to the Pd^{2+} ions through either atom (O or N in this case). Spectroscopic studies were performed on propanediol (OH group containing ligand) and aminopropanol (OH & NH_2 containing ligand) and were then backed up by both periodic and non-periodic (atom-centred) simulations.

5.2 Computational Details

We again use Density Functional Theory (DFT) as incorporated within the VASP (Vienna Ab initio Software Package)^{69,68,70,71}, discussed in Chapter 2 and ORCA simulation packages¹⁰⁸ to model already formed nanoparticles as extended surfaces and precursor molecules respectively. As noted, the latter calculations were undertaken by Cameron Beevers (Cardiff Chemistry)

As discussed in Chapter 2, the Perdew-Burke-Ernzerhof (PBE) exchange-correlation functional^(51,78) was employed to account for the exchange and correlation effects on formed nanoparticles with the projector augmented-wave (PAW) method used to represent atomic core states^{25,26}.

Extended tests were performed with PBE and Becke-Perdew-86 functional (BP86) in order to ensure consistency between periodic and non-periodic simulations. These tests have indicated that PBE function is a reasonable compromise between cost and accuracy and thus can be used further for the remainder of the work.

Dispersion effects were included in both atom-centred and plane-wave models using Grimme's empirical DFT-D3 model⁸¹. For non-periodic, atom centred models, DFT-D3BJ (DFT-D3 with Becke-Johnson damping) was used to prevent artificial short-range repulsive interactions^{81,109–111}.

Dipole correction along the z-direction of the periodic slab model was applied in all calculations. A Monkhorst-Pack grid was used to sample the Brillouin zone⁸². For optimisation calculations, the number of k -points used was $7 \times 7 \times 7$ for the optimisation of the fcc unit cell bulk structure, and $7 \times 7 \times 1$ for the surfaces. For the adsorption calculations on the (111) surface, a 5 atomic layers thick slab with a $p(4 \times 4)$ surface supercell (80 atoms), was employed. For the (100) surface a $c(3 \times 3)$ surface slab was constructed, again 5 layers thick (90 atoms). During optimisation calculations, the top two layers of the slabs were relaxed and the lower 3 layers fixed at their optimised bulk positions. A $3 \times 3 \times 1$ k -points sampling was used for all surface calculations. The periodically repeated slabs were separated by a 20 Å vacuum layer along the Z direction, which is enough to avoid any spurious interaction with periodically replicated images. A kinetic energy of the plane waves was set to 400 eV ensuring no Pulay stress. The convergence criterion was set such that the calculations converge when the forces are less than 0.02 eV Å⁻¹ for adsorption calculations, 0.001 eV Å⁻¹ for the bulk, and 0.01 eV

\AA^{-1} for surface optimisation calculations. The adsorption energy was computed using equation (5.1).

$$E_{ads} = (E_{ad+sl} - E_{sl} - E_{ad}) \quad (5.1)$$

where E_{ad+sl} is the energy of the adsorbate adsorbed on the slab, E_{sl} is the energy of the naked slab, and E_{ad} is the energy of the adsorbate in gas phase, i.e. in a cell large enough to avoid intermolecular interactions.

The ORCA implementation of Karlsruhe quadruple zeta with valence and polarisation functions basis set (def2-QZVP), the auxiliary Weigend basis set (def2/J), and Stuttgart–Dresden effective core potentials (ECPs) were used for all non-periodic atom-centred DFT calculations^{112–114}. The convergence criteria for these calculations were an energy change of 2.72×10^{-5} eV with a maximum gradient of 5.14×10^{-3} eV \AA^{-1} and a maximum displacement of 5.29×10^{-4} \AA .

The species present in the reaction solutions have been examined through comparison of experimental with computed spectra. Simulated UV-Vis. spectra were calculated using the simplified Tamm-Dancoff approximation of time-dependent DFT (sTDA-DFT), which has been shown to give good agreement with time-dependent DFT for the electronic transitions energies, although, it is known that intensities calculated using this method are less reliable¹¹⁵. The calculation efficiency of sTDA-DFT has also been increased by employment of the RIJCOSX approximation of the Coulomb and exchange integrals. Structures showing sTDA-DFT transitions consistent with the wavelength of experimentally observed bands were also calculated using the more demanding time-dependent DFT (TD-DFT) with the RIJCOSX integral approximation. TD-DFT spectra were examined using the Multiwfn software package, which applies Gaussian curve broadening¹¹⁶. Calculated excitations and orbital compositions were determined using the Mulliken method.¹¹⁷ Localised orbital centroid analysis was also undertaken in order to examine the ligand bonding and oxidation state of the Pd^{2+} ions in the nanoparticle precursor molecule using the methodology of Vidossich and Lledós.¹¹⁸ This utilised the ORCA software package's implementation of the Pipek-Mezey population-localisation methodology to derive localised orbitals from the DFT-calculated electronic structure^{119, 120}. The gas phase energy changes of reaction, ΔE_r , were calculated using equation 5.2.

$$\Delta E_r = \sum E_{products} - \sum E_{reactants} \quad (5.2)$$

5.3 Results and Discussion

The experimental group in Milan started by examining the coordination of the capping agent molecules 3-aminopropanol (AP) to Pd²⁺ ions using UV-Vis spectroscopy. H₂PdCl₄ was used as a precursor for the preparation of the Pd nanoparticles. The preparation of Pd nanoparticles using H₂PdCl₄ was reported by other groups as well. Klasovsky *et al.* prepared (Hydr-)oxidic PdO_xH_y colloids by hydrolysing H₂PdCl₄ in the presence of poly(vinylpyrrolidone) under pH control. The main species found in acidic media were PdCl₄²⁻ and [PdCl₃(H₂O)]⁻.¹²¹ These species were found to be responsible for ligand to metal charge-transfer (CT) and d–d electronic transitions. Wang *et al.* also observed the same species when using solid PdCl₂ as a precursor. The group collected UV-vis. spectra of solutions depending on the pH of the media.¹²² Charge-transfer and d-d transitions at 280 nm/475 nm and 320 nm/430 nm were observed when the pH of the solution was 1.3. Upon hydrolysis, these transitions disappeared and were replaced by a rise at short wavelengths with a peak centred at 270 nm.

To begin, the H₂PdCl₄ precursor was characterised by UV-Vis spectroscopy with clear visible bands at 310 and 418 nm (Figure 5.3). In order to assign these bands to specific species, Time-Dependent Density Functional Theory (TD-DFT) simulations were carried out by Cameron Beevers to model UV-Vis. absorption spectra of PdCl₄²⁻ (Figure 5.3(A)), Pd₂Cl₆²⁻ species (Figure 5.3(B)), and [PdCl₃(H₂O)]⁻ (Figure 5.3(C)). The TD-DFT computed spectra for PdCl₄²⁻ and Pd₂Cl₆²⁻ are in good agreement with the observed experimental spectrum. The data obtained from the computational work indicate that the band present at 420 nm in the experimental spectra is due to a transition from the Cl *p* orbital to the Pd *s* orbital. The width of the band is most likely a contribution from two other transitions: the 470 nm transition which corresponds to a Pd *d* to Pd *p* excitation within the two Pd ions of the dimer and a 388 nm transition, shown in the computed spectra of PdCl₄²⁻ which is attributed to a *p-p* excitation from chlorine to palladium. Therefore, the experimental band centred at 418 nm could include all the contributions predicted by the model systems.

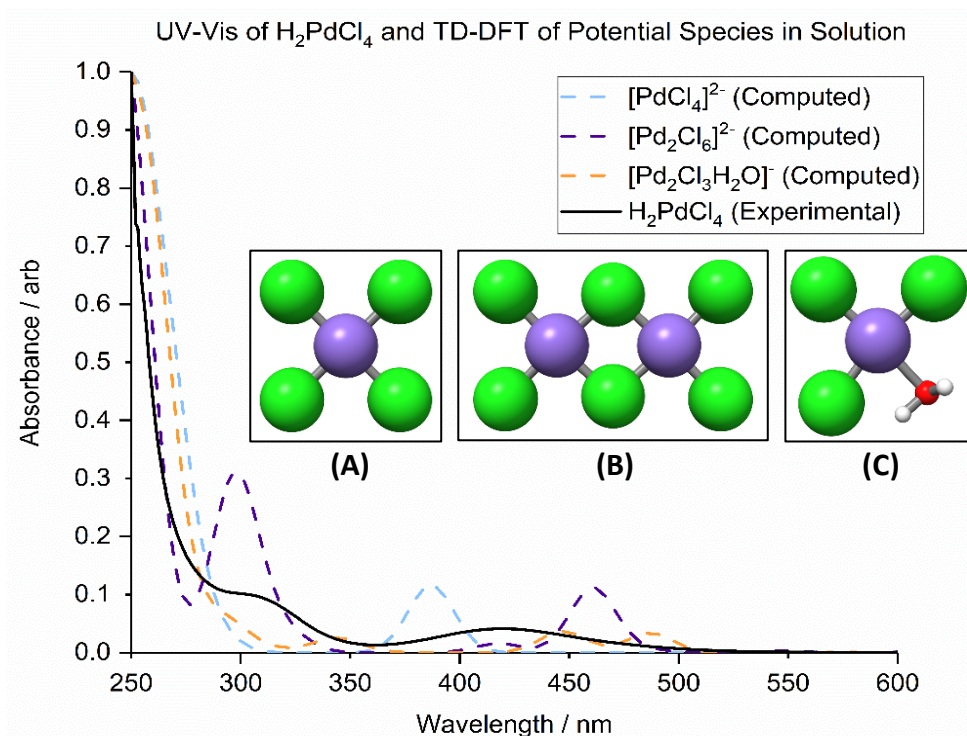


Figure 5.3: Experimental UV-Vis. spectra of H_2PdCl_4 in solution at pH 3 (black), computed UV-Vis. spectra of $[\text{PdCl}_4]^{2-}$, $[\text{Pd}_2\text{Cl}_6]^{2-}$, and $[\text{PdCl}_3\text{H}_2\text{O}]^-$. Inset: Structures of PdCl_4^{2-} , (A); $\text{Pd}_2\text{Cl}_6^{2-}$, (B); and $[\text{PdCl}_3(\text{H}_2\text{O})]^-$, (C). Colour code: Pd: purple; Cl: green; O: red and H: light grey.

This agreement with the experimental spectrum suggests that the Pd sol is comprised of an equilibrium mixture of all these species, which is also supported by the calculated energies of reaction for the formation of $\text{Pd}_2\text{Cl}_6^{2-}$ and $[\text{PdCl}_3(\text{H}_2\text{O})]^-$ from PdCl_4^{2-} (Table 5.1). The calculated values, which are for gas phase reactions. indicate that the formation of the dimer and the hydrated complex are both exothermic processes with the dimer being more energetically favourable.

Table 5.1: Energy change of reaction (ΔE_r) for the formation of $\text{Pd}_2\text{Cl}_6^{2-}$ and $[\text{PdCl}_3\text{H}_2\text{O}]^-$ from PdCl_4

| Products | $\Delta E_r / \text{kJ mol}^{-1}$ |
|---|-----------------------------------|
| $\text{Pd}_2\text{Cl}_6^{2-}$ | -252 |
| $[\text{PdCl}_3(\text{H}_2\text{O})]^-$ | -215 |

Aminopropanol was then added to the Pd^{2+} sol and then reduced with NaBH_4 . The recorded experimental UV-Vis. spectrum is shown in Figure 5.4. The initial UV-Vis. spectrum of Pd^{2+} sol is consistent with both the experimental and the computational plots produced in figure 5.4. Upon the addition of aminopropanol (green line in figure

5.4), the initial broad peak present at 418 nm disappears with a shift and broadening of the peak at 307 nm to 312 nm. These changes in wavelength and absorbance are a result of the chlorine ligand substitution by the aminopropanol capping agent.

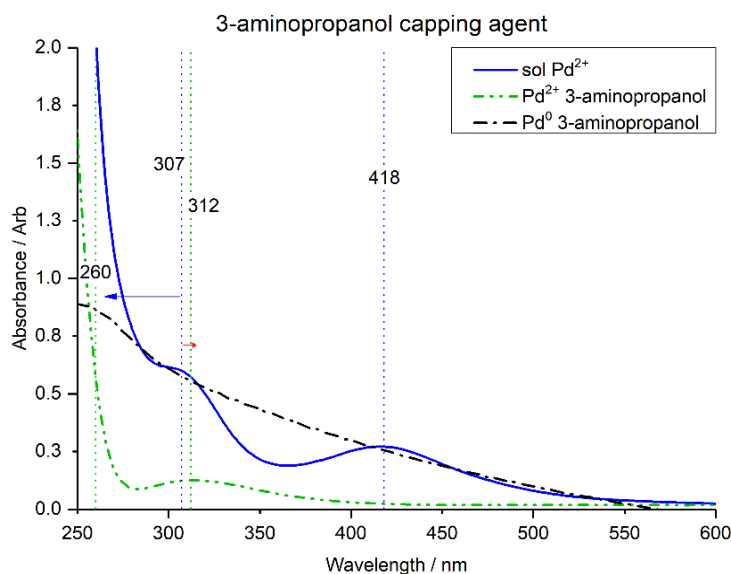


Figure 5.4: UV vis spectra of H_2PdCl_4 in solution (blue), in presence of the capping agent 3-aminopropanol (green), Pd with 3-aminopropanol reduced (black).

The TD-DFT spectrum of the most favourable product, $[\text{PdCl}_3\text{AP}]^-$, (Figure 5.5, dashed blue line) was also consistent with experimental results thus suggesting that the lowest energy structure binds through the nitrogen of aminopropanol. The energy of reaction for the formation of the ligand coordinated complexes from PdCl_4 are shown in table 5.2. The peak observed at 334 nm in the computational spectrum shows an excitation from a hybrid Pd d -Cl p orbital to a molecular orbital composed from the palladium sp and a hybridisation of orbitals in the aminopropanol ligand.

Table 5.2: Energy change of reaction for the potential products of the reaction between PdCl_4 and 3-aminopropanol.

| Potential Products | $\Delta E_r / \text{kJ mol}^{-1}$ |
|--|-----------------------------------|
| $\text{PdCl}_2\text{OHAp (cis)}$ | -207 |
| $\text{PdCl}_2\text{OHAp (trans)}$ | -188 |
| PdCl_3Ap | -305 |
| PdCl_2Ap_2 | -295 |

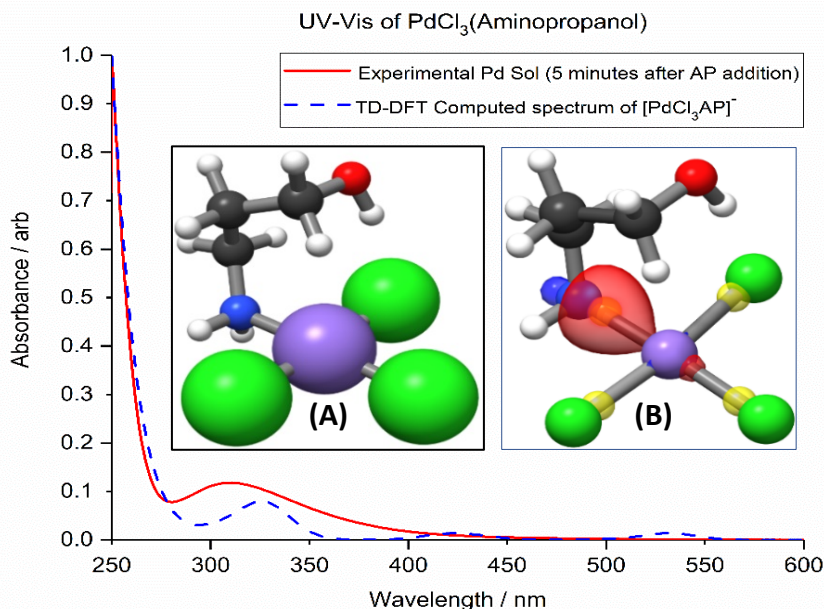


Figure 5.5: UV-Vis. spectra of PdCl_4^{2-} sol in presence of the capping agent 3-aminopropanol (green) and computed TD-DFT spectrum of PdCl_3AP (blue dashed). Inset: (A), $\text{PdCl}_3\text{AP}^{1-}$ lowest energy geometry; (B), $[\text{PdCl}_3\text{Ap}]^-$ with the Pd—N localised bonding orbital and the centroids for the Pd—N and Pd—Cl bonds. Colour code: Pd: lilac; Cl: green; O: red; N: blue; C: dark grey; H: white; and localised orbital centroids: translucent yellow.

This agreement with the experimental spectrum suggests that the aminopropanol is directly binding to the Pd^{2+} species in a manner consistent with structure figure 5.5(A). The interaction between the amino group and the Pd^{2+} is strong enough that it could induce a change in the actual oxidation state of the metal by partial reduction. As a result, centroid analysis of the Pipek-Mezey localised orbitals was utilised to examine the oxidation state of Pd and the character of the AP—metal bond, figure 5.5(B).

Analysis of the centroids centred upon the Pd atom indicate that the electronic configuration of Pd is consistent with that of Pd (II)($4s^2 4p^6 4d^8$). Moreover, the localised bonding orbitals indicate that the bond between aminopropanol and Pd is largely dative in character with the electrons in the bonding orbitals being biased towards the more electronegative nitrogen.

FT-IR spectra of the Pd complexes were also recorded and compared to the pure ligand molecules (figure 5.6). Upon the addition of aminopropanol to Pd^{2+} ions, the peaks observed at 3483 and 3442 cm^{-1} decrease in intensity and new bands at 3229 and 3137

cm^{-1} appear. Moreover, the -N-H bending mode observed at 1605 cm^{-1} is shifted to 1586 cm^{-1} .

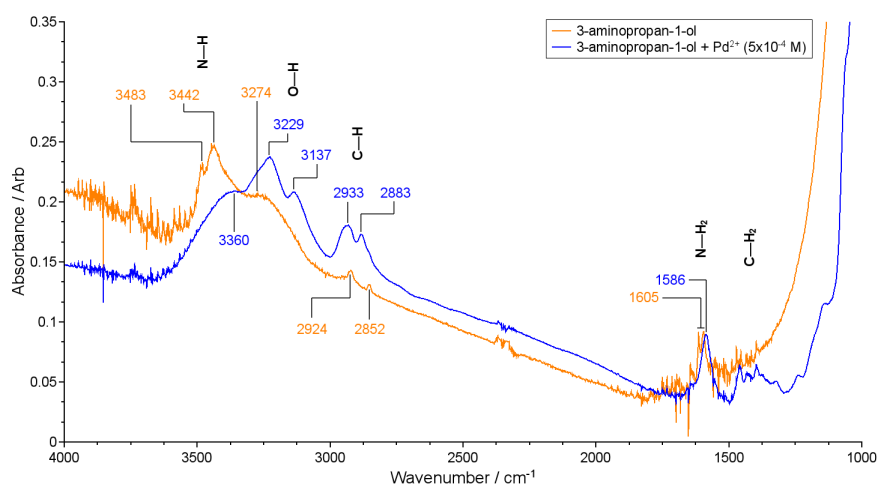


Figure 5.6: FT-IR spectra of 3-aminopropanol (AP) and Pd-AP.

Reduction with NaBH_4 was next investigated by the experimental group. It was found to result in a peak shift toward shorter wavelengths (260 nm) in the UV-Vis. spectrum (figure 4, black line) with a broadening of the band at 310 nm in the presence of the AP capping agent. An increase in the background absorbance was also observed which can be attributed to Willis-Tyndall scattering which is characteristic for the formation of particles.

In order to rationalise the differences between the two spectra, periodic models of the surfaces were modelled and frequency calculations of the most stable conformations of the Pd (II)-AP complex were performed. (The periodic calculations were the main contribution of this work to the collaborative research project)

In order to determine the most stable conformation of the adsorbate, different conformations were first optimised in gas phase. Upon optimisation with both plane-wave and atom-centred models, two conformations were found to be the most favourable: One where an internal hydrogen bond between the hydroxyl oxygen and the amino nitrogen is taking place and another that is a straight chain configuration (figure 5.7). Both plane-wave and atom-centred models confirmed that the H-bonded conformation is more stable with an electronic energy $\sim 0.8 \text{ eV}$ lower than that of the other structure.

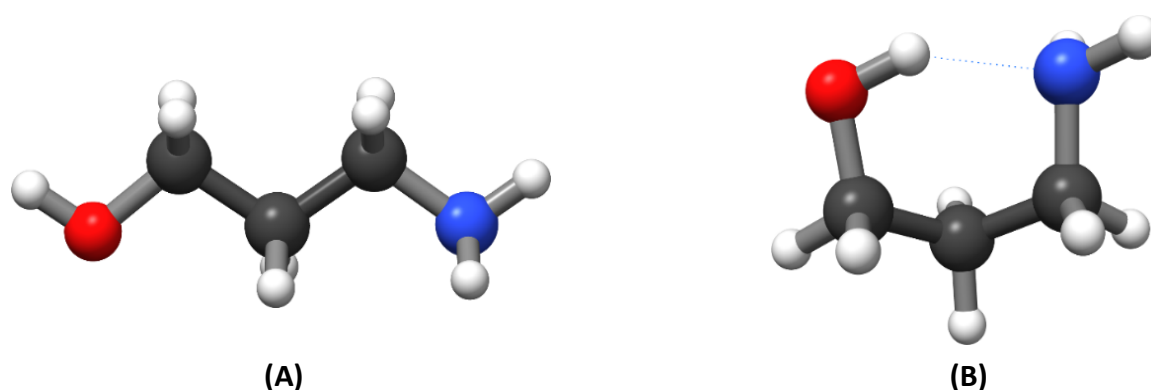


Figure 5.7: Optimisation of two different conformations of the AP adsorbate in the gas phase: (A) all trans, (B) conformation with internal H-bond. (Colour code: Blue: N, Red: O, Grey: C, and White: H)

The most stable conformation of AP was then adsorbed on the two low index surfaces of palladium metal: Pd (111) and Pd (100). Different conformations of the aminopropanol on the surfaces were then investigated. Structures with both heteroatoms binding to the surface were found to be unstable due to internal strain within the 3-aminopropanol. In the case with AP adsorbed through the amine N atom, the hydroxyl hydrogen is attracted also towards the surface. Table 5.3 and figures 5.8, 5.9, 5.10, and 5.11 summarise the results obtained.

Table 5.3: Adsorption energies of the different configurations of 3-aminopropan-1-ol on Pd (100) and Pd(111) surfaces

| Pd(111) surface | | |
|----------------------------------|--|--------------------------------------|
| Configuration | Energy of Adsorption/ kJ mol^{-1} | N-Pd or O-Pd distance / \AA |
| Nitrogen Binding | -145 | 2.15 |
| Oxygen Binding | -95 | 2.34 |
| Pd(100) surface | | |
| Configuration | Energy of Adsorption/ kJ mol^{-1} | N-Pd or O-Pd distance / \AA |
| Nitrogen Binding (O up) | -127 | 2.16 |
| Nitrogen Binding (O Down) | -149 | 2.15 |
| Oxygen Binding | -86 | 2.32 |

On both Pd(111) and Pd(100) surfaces, the conformation with the nitrogen binding to the Pd was found to be more stable. As a result of the high stability of the (111) surface, the bonding of the nitrogen-binding conformations to the Pd (100) surface is stronger, which results in the ligand preferentially adsorbing on Pd(100) facets making the surface less accessible. As a result, nanoparticle growth on the Pd(111) facet is favoured

resulting in a greater surface area of Pd (100) facets. This observation confirms the important role of the capping agent in controlling the growth mechanism and directing the final particle shape. In addition, the selective blocking of Pd(100) surface can have an important impact on the catalytic performances of Pd NPs.

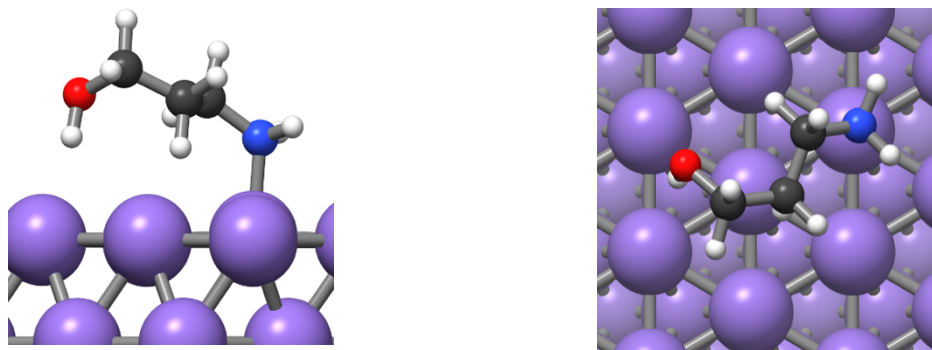


Figure 5.8: Adsorption of the AP adsorbate on the Pd(111) surface with the nitrogen binding to the surface. (Colour code: Purple: Pd, Blue: N, Red: O, Grey: C, and White:

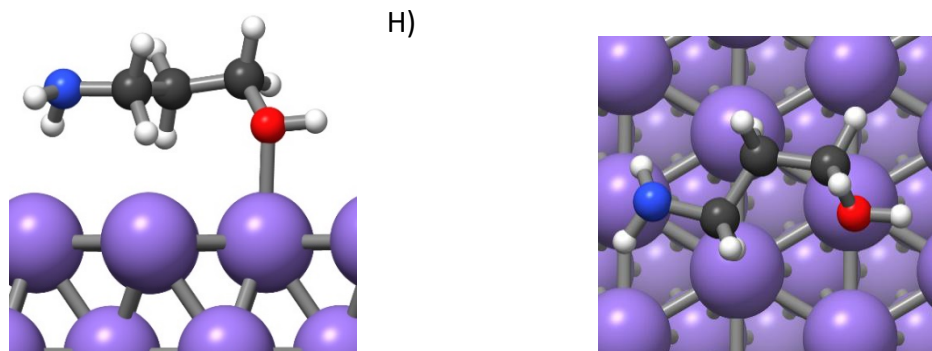


Figure 5.9: Adsorption of the AP adsorbate on the Pd(111) with the oxygen binding to the surface. (Colour code: Purple: Pd, Blue: N, Red: O, Grey: C, and White: H)

Frequency calculations on the most stable conformations were then performed in order to predict the IR spectra. Figure 5.12 shows the spectra of the most stable different conformations and their comparison with the experimental spectrum. The strong correlation between the spectra can be taken as a good indication that the aminopropanol caps the nanoparticle surfaces by bonding through the amino moiety. This is further supported by the oxygen binding spectra which indicate that the O—H vibrational modes are significantly less infrared active than the nitrogen binding O—H modes in both the experimental and computed nitrogen binding spectra. Whilst the accuracy of the extended-surface model for many properties of small NPs is limited, the assignment of the spectrum to the N-binding species should not be of concern. The

spectra for the nitrogen binding of AP on the Pd (111) and Pd (100) surfaces are very similar. Given that the difference between the two surfaces is the number of surrounding atoms, it can be concluded that the coordination number of Pd has very little effect on the vibration energies. Therefore, if the nanoparticles are small to an extent where the corner or edge sites are significant, the adsorption of AP on these sites is not likely to affect the resultant spectra.

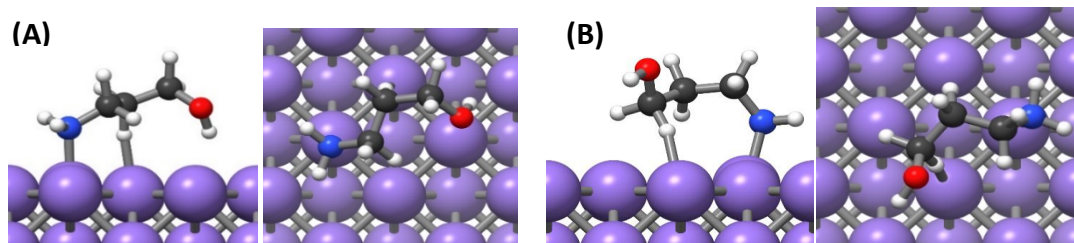


Figure 5.10: Adsorption of the AP adsorbate on the Pd(100) with the Nitrogen binding to the surface and (A) the oxygen pointing downwards and (B) the oxygen pointing upwards. (Colour code: Purple: Pd, Blue: N, Red: O, Grey: C, and White: H)

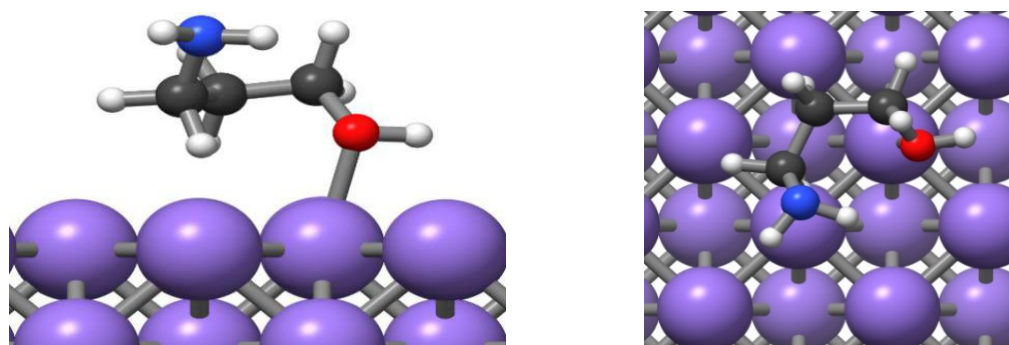


Figure 5.11: Adsorption of the AP adsorbate on the Pd(100) with the oxygen binding to the surface. (Colour code: Purple: Pd, Blue: N, Red: O, Grey: C, and White: H)

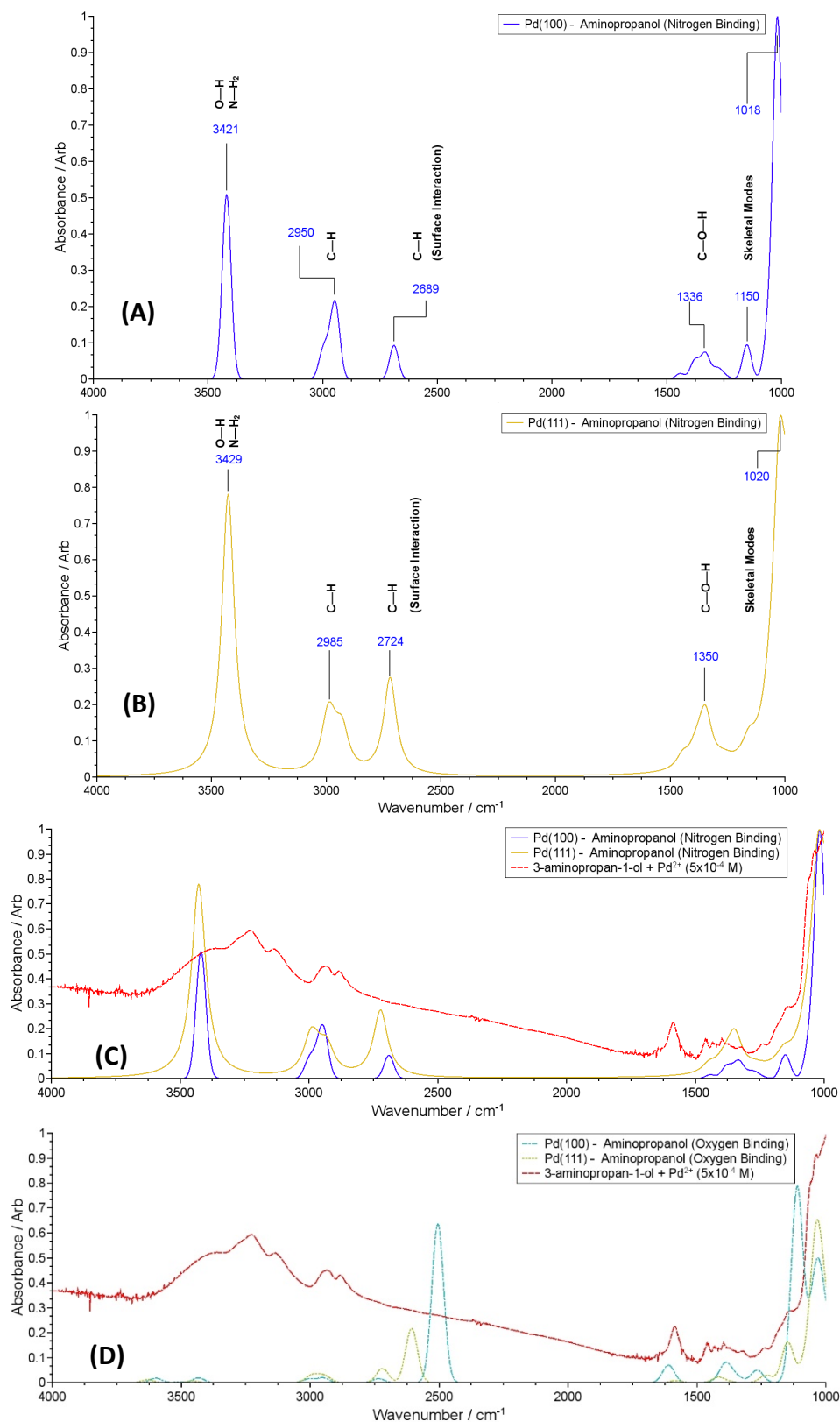


Figure 5.12: IR spectra for the most stable conformations: (A) nitrogen binding of the aminopropanol on the Pd (100) surface (B) nitrogen binding of the aminopropanol on the Pd (111) surface (C) plots A and B overlaid with the experimentally obtained IR spectrum (D) oxygen binding on the Pd (111) and Pd (100) surfaces overlaid with the experimentally obtained IR spectrum

5.4 Conclusion

The combination of experimental spectroscopic techniques and theoretical modelling has allowed us to understand the coordination of hydroxyl- and amino-group containing ligands to Pd species derived from PdCl₂ during the formation of metal nanoparticles. The addition of aminopropanol to the molecular precursors results in a displacement of the chloride ion to form a Pd(II)Cl₃AP complex. Due to the high stability of the (111) surface, the ligand binds more strongly to the (100) surface making it less accessible. As a result, the aminopropanol is able to direct the growth process which in turn affects the shape of the resultant nanoparticles. Although the complexity of AP does not resemble that of other macromolecules such as polymers and dendrimers, these results help by shedding light on the different processes occurring at the interface between the metal surface and the ligand layer.

Future work will rely on results provided in this chapter to investigate further the role of capping agents in metal nanoparticle synthesis. Since the ubiquity of Pd nanoparticles in the field of catalysis is a result of the activity of Pd, it is therefore important to investigate whether using aminopropanol as a capping agent will affect its catalytic activity.

The work presented in this chapter has been published in the Journal of Physical Chemistry C.⁹¹

Chapter 6 Summary and General Conclusions

In this thesis we studied the partial oxidation of methane to methanol on Au and Pd surfaces using hydrogen peroxide and molecular oxygen as oxidants. The adsorption energy of hydrogen peroxide is more negative on the Pd surfaces thus making the cleavage of the O–O bond easier on Pd than on Au. The transition state for the cleavage of the hydrogen peroxide corresponds to the rotation of the hydroxyl bond pointing towards the surface thus making the energy barrier for the cleavage step relatively small on both surfaces (4.5 kJ mol⁻¹ on the Pd(100) and 21.7 kJ mol⁻¹ on the Pd(111)). The barriers for the cleavage of H₂O₂ on the Au(100) and Au(111) surfaces were found to be 38.3 kJ mol⁻¹ and 57.3 kJ mol⁻¹. Thus, the cleavage of hydrogen peroxide on Pd proceeds more easily than Au.

The cleavage of the hydrogen peroxide results in the production of hydroxyl radicals which are responsible for the hydrogen abstraction step from methane. In the configurations for the adsorption of methane and the hydroxyl radical, the hydroxyl group was in a bridge position with the hydrogen of the hydroxyl group pointing away from the methane. Upon hydrogen abstraction, a methyl radical and water are produced with the methyl radical being strongly stabilised by the surfaces. Calculations of the energy of reaction (ΔE) reveal that the (111) surfaces are exothermic while the (100) surfaces are slightly endothermic, which initially suggests that the (111) surfaces are better at stabilising the methyl radical than the (100) surfaces. However, the calculation of the adsorption energy of a methyl radical and a hydroxyl radical on their own reveal that the higher (endothermic) energies observed for the (100) surfaces are largely a result of the higher adsorption energy of the hydroxyl radical on these surfaces. The energy barriers for the hydrogen abstraction step is similar across all four surfaces with the values ranging from 87-97 kJ mol⁻¹.

With the generation of the methyl radicals, the next step of the reaction mechanism involves the reaction of the methyl radical with molecular oxygen. This is a key step as it will determine the ability of the methyl radical to react with molecular oxygen to form the methyl peroxy radical. Optimisation of the methyl radical and molecular oxygen reveal that the methyl radical is in a top position (strongly stabilised by the surface) with molecular oxygen binding in a bridge-bridge position on the (100) surfaces and bridge-top on the (111) surfaces. The methyl peroxy radical generated, is strongly activated on

the Pd(111) surface and completely cleaves on the Pd(100) surface. The barriers for the formation of the methyl peroxy radical relative to the adsorbed methyl and oxygen on the Au(111), Au(100), and Pd(111) surfaces were found to be 64.0 kJ mol⁻¹, 105.2 kJ mol⁻¹ and 127.8 kJ mol⁻¹. In order to compare the barriers for the different steps, the overall energy profile for methane abstraction and the formation of the methyl peroxy radical was plotted (figure 6.1).

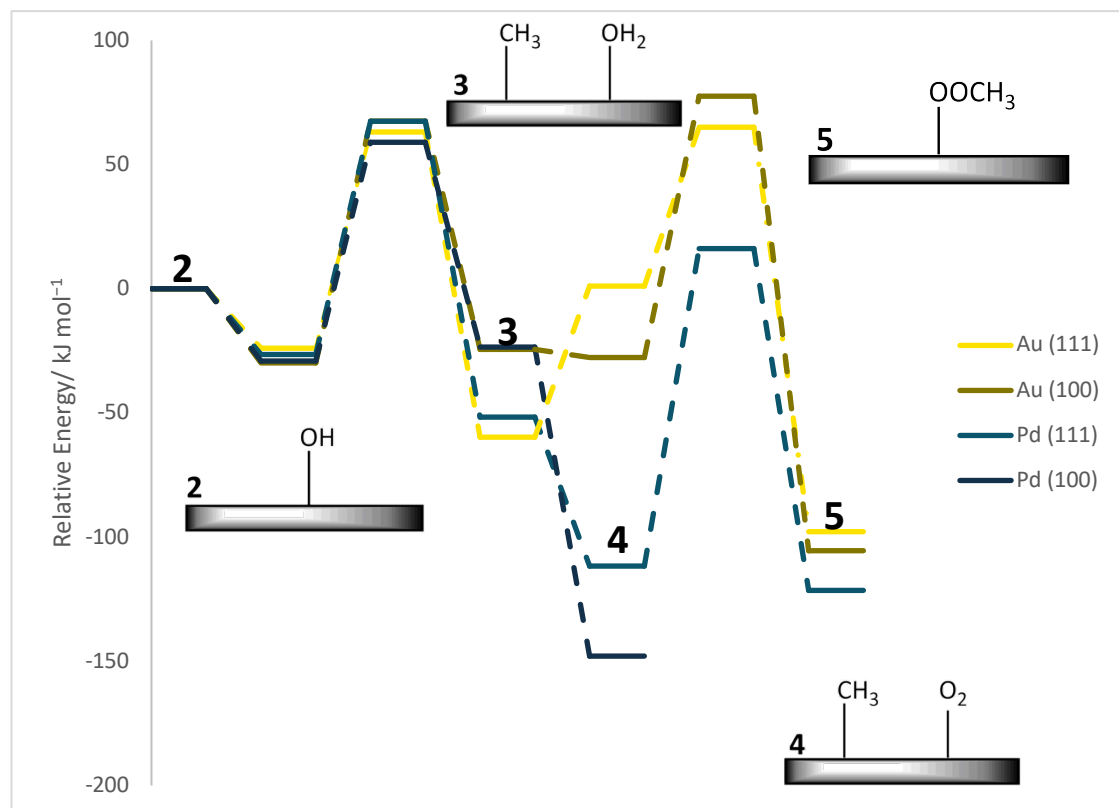


Figure 6.1: Energy profile for methane abstraction and the formation of the methyl peroxy radical on the different surfaces relative to the adsorbed hydroxyl on the respective surfaces, and methane and oxygen in gas phase.

It appears that the binding of water on a surface stabilised methyl radical is energetically more favourable than the binding of molecular oxygen on the Au(111) surface; in fact, there is a decrease in the overall energy of the system when transitioning from structure **3** to structure **4**. This suggests that the adsorption of molecular oxygen is unfavourable on the Au surfaces with an endothermic energy difference of +60.8 kJ mol⁻¹ for water displacement on the Au(111) and a slightly exothermic energy difference of -3.3 kJ mol⁻¹ for the (100). Interestingly, the opposite effect is observed on the Pd surfaces with both Pd surfaces exhibiting a high affinity to molecular oxygen. In fact, the adsorption of molecular oxygen on the (100) is so strong that only a barrier of +8.9 kJ mol⁻¹ is

needed for the oxygen cleavage. The barrier for the oxygen cleavage on the Pd(111) is $+62.8 \text{ kJ mol}^{-1}$ which is about half the energy barrier for the formation of the methyl peroxy radical on the surface; thus suggesting that the oxygen will cleave on the surface before it can react with the methyl radical. This suggests that a PdO surface is likely to form on the Pd surfaces. Since oxygen is more soluble in water than methane, this means that the oxygen cleavage step will most likely happen before even methane is activated by the hydroxyl radicals. With a completely oxidised surface, no vacant sites will be left on which the methyl radical can adsorb. This explains why no primary products were observed experimentally; the high and low affinity to molecular oxygen of the Pd and the Au surfaces respectively will most likely hinder the formation of the methyl hydroperoxide intermediate.

Modelling of the doped systems then reveals a change in the affinity for oxygen adsorption on both surfaces. The high affinity to molecular oxygen of the Pd surface is decreased upon the introduction of a single Au atom with the barriers for oxygen cleavage increasing from 8.9 kJ mol^{-1} to 18.1 kJ mol^{-1} on the Pd(100) surface and $+62.8 \text{ kJ mol}^{-1}$ to $+122.4 \text{ kJ mol}^{-1}$ on the Pd(111). The energy of displacement of water by molecular oxygen (ΔE) for the Au surfaces also improved with a change from $+60.8 \text{ kJ mol}^{-1}$ to $+2.20 \text{ kJ mol}^{-1}$ on the Au(111) surface and -3.3 kJ mol^{-1} to $-11.1 \text{ kJ mol}^{-1}$ on the Au(100) surface.

As for the production of the methyl peroxy radical, the dopant on the Au-doped Pd(111) lowered the energy barrier from $+127.8 \text{ kJ mol}^{-1}$ on the pure surface to $+119.9 \text{ kJ mol}^{-1}$; a difference of about 8 kJ mol^{-1} . An improved energy barrier for the formation of the methyl peroxy radical was also observed on the Pd-doped Au(100) surface with an energy difference of 13.7 kJ mol^{-1} .

The second section of the thesis addressed the use of 3-aminopropan-1-ol as a capping agent for the production of Pd nanoparticles. DFT studies on the adsorption of aminopropanol on the Pd(111) and Pd(100) surfaces reveal that the capping agent prefers to bind to the Pd surface through the amino-nitrogen rather than the hydroxyl-oxygen. This is further supported by a comparison of the computed IR and experimental spectra which show strong correlation.

Future work would include working on the alloyed system in order to understand how exactly it catalyses the reaction. The doped system results suggest that there is a balance between having enough affinity for molecular oxygen to adsorb and activate it but a low enough affinity that it does not dissociate leading to the formation of a metal oxide. Identification of the optimal alloy composition and surface geometry of the nanoclusters would require extensive further calculations looking at the whole potential energy surface for methane oxidation as a function of alloy composition. At the beginning, different bulk structures of the alloy would be modelled in order to determine the lowest energy structure. From there on, the (111) and the (100) surfaces would be cut and the reaction mechanism would be modelled whilst keeping in mind the results obtained for the pure metal surfaces. Bader charge analyses would also be included to determine the charge distribution along the alloyed surface along with the charge present on different intermediary species. Since only hydroxyl radicals and atomic oxygen have been examined for methane activation, we can extend the study to include other species such as molecular oxygen and peroxy radicals, the latter which can be performed by hydrogen abstraction of molecular oxygen from water. Since the presence of an aqueous medium is essential for the reaction, we aim to model the presence of water molecules by examining different implicit and explicit models in order to determine which of the two is best for our detailed mechanistic study.

We would also extend the study to other catalysts such as iron- and copper-containing zeolites which as discussed in chapter 1 have already been shown to be active species for this reaction. Most of the work discussed in chapter 1 has been performed using Density Functional Theory (DFT) using the Vienna Ab initio Simulation Package (VASP). Whilst this produces reliable results, it is computational expensive as the system is large. Therefore, it would be interesting to try using Hybrid Quantum Mechanics/Molecular Mechanics (QM/MM) simulations to compare both the results obtained and the computational time. We would also extend the study to include other zeolites such as chabazite and faujasite. Methods will also be developed to include the effect that the solvent phase has on the transport of hydrocarbons in porous materials. Some of the preliminary results and benchmarking for this work is shown in the appendix.

References:

- 1 U. Energy Information Administration, *International Energy Outlook 2016*, 2040.
- 2 M. C. Alvarez-Galvan, N. Mota, M. Ojeda, S. Rojas, R. M. Navarro and J. L. G. Fierro, *Catal. Today*, 2011, **171**, 15–23.
- 3 G. Iaquaniello, G. Centi, A. Salladini and E. Palo, in *Methanol*, Elsevier, 2018, pp. 595–612.
- 4 P. Tian, Y. Wei, M. Ye and Z. Liu, *ACS Catal.*, 2015, **5**, 1922–1938.
- 5 M. Khanmohammadi, S. Amani, A. B. Garmarudi and A. Niaei, *Chinese J. Catal.*, 2016, **37**, 325–339.
- 6 Z. Azizi, M. Rezaeimanesh, T. Tohidian and M. R. Rahimpour, *Chem. Eng. Process. Process Intensif.*, 2014, **82**, 150–172.
- 7 J. H. Jones, *Platin. Met. Rev.*, 2000, **44**, 94–105.
- 8 B. A. Arndtsen, R. G. Bergman, T. A. Mobley and T. H. Peterson, *Acc. Chem. Res.*, 1995, **28**, 154–162.
- 9 M. Ravi, M. Ranocchiari and J. A. van Bokhoven, *Angew. Chemie - Int. Ed.*, 2017, **56**, 16464–16483.
- 10 A. A. Latimer, H. Aljama, A. Kakekhani, J. S. Yoo, A. Kulkarni, C. Tsai, M. Garcia-Melchor, F. Abild-Pedersen Ab and J. K. Nørskov, *Phys. Chem. Chem. Phys*, 2017, **19**, 3575.
- 11 A. A. Latimer, A. R. Kulkarni, H. Aljama, J. H. Montoya, J. Suk Yoo, C. Tsai, F. Abild-Pedersen, F. Studt and J. K. Nørskov, , DOI:10.1038/NMAT4760.
- 12 E. G. Lance, D. Elworthy, *French Pat. 352687*.
- 13 D. M. Newitt and A. E. Haffner, *Proc. R. Soc. A Math. Phys. Eng. Sci.*, 1932, **134**, 591–604.
- 14 E. H. Boomer and V. Thomas, *Can. J. Res.*, 1937, **15b**, 414–433.
- 15 E. H. BOOMER and S. N. NALDRETT, *Can. J. Res.*, 1947, **25**, 494–501.
- 16 V. Atroshchenko, Z. M. Shchedrinskaya and N. A. Gavrya, *J. Appl. Chem*, 1965, **38**, 643–649.
- 17 D. A. Dowden and G. T. Walker, *Br. Pat. 1244001*.
- 18 R. S. Hanson and T. E. Hanson, *Methanotrophic Bacteria*, 1996, vol. 60.
- 19 N. A. Elango, R. Radhakrishnan, W. A. Froland, B. J. Wallar, C. A. Earhart, J. D. Lipscomb and D. H. Ohlendorf, *Protein Sci.*, 2008, **6**, 556–568.




- 20 G. C. Bond and D. T. Thompson, *Gold Bull.*, 2000, **33**, 41–50.
- 21 G. J. Hutchings, *Gold Bull.*, 1996, **29**, 123–130.
- 22 A. K. Sinha, S. Seelan, S. Tsubota and M. Haruta, *Top. Catal.*, 2004, **29**, 95–102.
- 23 J. K. Edwards, B. Solsona, P. Landon, A. F. Carley, A. Herzing, M. Watanabe, C. J. Kiely and G. J. Hutchings, *J. Mater. Chem.*, 2005, **15**, 4595–4600.
- 24 P. Landon, P. J. Collier, A. J. Papworth, C. J. Kiely and G. J. Hutchings, *Chem. Commun.*, 2002, **18**, 2058–2059.
- 25 R. M. Finch, N. A. Hodge, G. J. Hutchings, A. Meagher, Q. A. Pankhurst, M. R. H. Siddiqui, F. E. Wagner and R. Whyman, *Phys. Chem. Chem. Phys.*, 1999, **1**, 485–489.
- 26 J. K. Edwards, B. E. Solsona, P. Landon, A. F. Carley, A. Herzing, C. J. Kiely and G. J. Hutchings, *J. Catal.*, 2005, **236**, 69–79.
- 27 D. I. Enache, J. K. Edwards, P. Landon, B. Solsona-Espriu, A. F. Carley, A. A. Herzing, M. Watanabe, C. J. Kiely, D. W. Knight and G. J. Hutchings, *Science (80-.)*, 2006, **311**, 362–365.
- 28 M. H. Ab Rahim, M. M. Forde, R. L. Jenkins, C. Hammond, Q. He, N. Dimitratos, J. A. Lopez-Sanchez, A. F. Carley, S. H. Taylor, D. J. Willock, D. M. Murphy, C. J. Kiely and G. J. Hutchings, *Angew. Chemie Int. Ed.*, 2013, **52**, 1280–1284.
- 29 X. Liu, M. Conte, M. Sankar, Q. He, D. M. Murphy, D. Morgan, R. L. Jenkins, D. Knight, K. Whiston, C. J. Kiely and G. J. Hutchings, *Appl. Catal. A Gen.*, 2015, **504**, 373–380.
- 30 M. Conte, X. Liu, D. M. Murphy, K. Whiston and G. J. Hutchings, *Phys. Chem. Chem. Phys.*, 2012, **14**, 16279–16285.
- 31 N. Agarwal, S. J. Freakley, R. U. McVicker, S. M. Althahban, N. Dimitratos, Q. He, D. J. Morgan, R. L. Jenkins, D. J. Willock, S. H. Taylor, C. J. Kiely and G. J. Hutchings, *Science (80-.)*, 2017, **358**, 223–227.
- 32 S. J. Tauster, , DOI:10.1021/ar00143a001.
- 33 A. Bruix, J. J. Rodriguez, P. J. Ramirez, S. D. Senanayake, J. Evans, J. B. Park, D. Stacchiola, P. Liu, J. Hrbek and F. Illas, *J. Am. Chem. Soc.*, 2012, **134**, 8974.
- 34 Y. Xi and A. Heyden, , DOI:10.1021/acscatal.9b01619.
- 35 N. A. G. V. I. Atroshchenko, Z. M. Shchedrinskaya, *Russ. J. Appl. Chem.*, 1965, **38**, 643–649.
- 36 A. C. Rosenzweig, C. A. Frederlck, S. J. Lippard and P. Nordlund, *Crystal structure*

of a bacterial non-haem iron hydroxylase that catalyses the biological oxidation of methane, 1993.

- 37 C. Hammond, M. M. Forde, M. H. Ab Rahim, A. Thetford, Q. He, R. L. Jenkins, N. Dimitratos, J. A. Lopez-Sanchez, N. F. Dummer, D. M. Murphy, A. F. Carley, S. H. Taylor, D. J. Willock, E. E. Stangland, J. Kang, H. Hagen, C. J. Kiely and G. J. Hutchings, *Angew. Chemie Int. Ed.*, 2012, **51**, 5129–5133.
- 38 C. Hammond, R. L. Jenkins, N. Dimitratos, J. A. Lopez-Sanchez, M. H. ab Rahim, M. M. Forde, A. Thetford, D. M. Murphy, H. Hagen, E. E. Stangland, J. M. Moulijn, S. H. Taylor, D. J. Willock and G. J. Hutchings, *Chem. - A Eur. J.*, 2012, **18**, 15735–15745.
- 39 J. Yuan, L. Wang and Y. Wang, *Ind. Eng. Chem. Res*, 2011, **50**, 6513–6516.
- 40 M. F. Fella and I. Onal, , DOI:10.1021/jp9097292.
- 41 B. R. Wood, J. A. Reimer, A. T. Bell, M. T. Janicke and K. C. Ott, *J. Catal.*, 2004, **225**, 300–306.
- 42 D. A. (Donald A. McQuarrie and J. D. (John D. Simon, *Physical chemistry : a molecular approach*, University Science Books, 1997.
- 43 L. De Broglie, *Philos. Mag. Lett.*, **86**, 411–423.
- 44 E. Schrödinger, *Phys. Rev.*, 1926, **28**, 1049–1070.
- 45 W. Koch and M. C. Holthausen, *Wolfram Koch , Max C. Holthausen A Chemist ' s Guide to Density Functional Theory*, Wiley-VCH Verlag GmbH, 2001, vol. 3.
- 46 E. Fermi, *Rend. Accad. Naz. Lincei*, 1927, **6**, 602–607.
- 47 P. Hohenberg and W. Kohn, *Phys. Rev.*, 1964, **136**, 864–871.
- 48 W. Kohn and L. J. Sham, *Phys. Rev.*, 1965, **140**, 1133–1138.
- 49 D. M. Ceperley and B. J. Alder, *Phys. Rev. Lett.*, 1980, **45**, 566–569.
- 50 J. P. Perdew and Y. Wang, *Phys. Rev. B*, 1992, **45**, 13244–13249.
- 51 J. P. Perdew, K. Burke and M. Ernzerhof, *Phys. Rev. Lett.*, 1996, **77**, 3865–3868.
- 52 P. Tereshchuk and J. L. F. Da Silva, *J. Phys. Chem. C*, 2012, **116**, 24695–24705.
- 53 K. Tonigold and A. Groß, *J. Chem. Phys.*, 2010, **132**, 224701.
- 54 Y. Yu, X. Wang and K. H. Lim, *Catal. Letters*, 2011, **141**, 1872–1882.
- 55 M. Pozzo and D. Alfè, *Int. J. Hydrogen Energy*, 2009, **34**, 1922–1930.
- 56 F. Jensen, *Introduction to computational chemistry*, John Wiley & Sons, 2007.
- 57 R. Dronskowski, *Computational Chemistry of Solid State Materials*, Wiley, 2005.
- 58 P. E. Blöchl, P. Margl and K. Schwarz, 1996, pp. 54–69.

- 59 D. R. Hamann, M. Schlüter and C. Chiang, *Phys. Rev. Lett.*, 1979, **43**, 1494–1497.
- 60 D. Vanderbilt, *Phys. Rev. B*, 1990, **41**, 7892–7895.
- 61 D. S. Sholl and J. A. Steckel, *Density Functional Theory: A Practical Introduction*, John Wiley and Sons, 2009.
- 62 H. JÓNSSON, G. MILLS and K. W. JACOBSEN, World Scientific Pub Co Pte Lt, 1998, pp. 385–404.
- 63 G. Henkelman, B. P. Uberuaga and H. Jónsson, *J. Chem. Phys.*, 2000, **113**, 9901–9904.
- 64 G. Henkelman and H. Jónsson, *J. Chem. Phys.*, 1999, **111**, 7010–7022.
- 65 A. Heyden, A. T. Bell and F. J. Keil, *J. Chem. Phys.*, 2005, **123**, 224101.
- 66 V. Petkov, B. Prasai, S. Shastri, J. W. Kim, S. Shan, H. R. Kareem, J. Luo and C. J. Zhong, *J. Phys. Chem. C*, 2017, **121**, 7854–7866.
- 67 J. R. Kitchin, J. K. Nørskov, M. A. Barteau and J. G. Chen, *J. Chem. Phys.*, 2004, **120**, 10240–10246.
- 68 G. Kresse and J. Hafner, *Phys. Rev. B*, 1993, **47**, 558–561.
- 69 G. Kresse and J. Hafner, *Phys. Rev. B*, 1994, **49**, 14251–14269.
- 70 G. Kresse and J. Furthmüller, *Comput. Mater. Sci.*, 1996, **6**, 15–50.
- 71 G. Kresse and J. Furthmüller, *Phys. Rev. B*, 1996, **54**, 11169–11186.
- 72 M. P. Teter, M. C. Payne and D. C. Allan, *Phys. Rev. B*, 1989, **40**, 12255–12263.
- 73 D. M. Bylander, L. Kleinman and S. Lee, *Phys. Rev. B*, 1990, **42**, 1394–1403.
- 74 D. M. Wood and A. Zunger, *J. Phys. A. Math. Gen.*, 1985, **18**, 1343.
- 75 P. Pulay, *Chem. Phys. Lett.*, 1980, **73**, 393–398.
- 76 D. D. Johnson, *Phys. Rev. B*, 1988, **38**, 12807–12813.
- 77 V. Minasyan, G. Grigoryan and A. Nalbandyan, *Oxid. Commun.*, 1998, 87–97.
- 78 J. P. Perdew, K. Burke and M. Ernzerhof, *ERRATA Generalized Gradient Approximation Made Simple [Phys. Rev. Lett. 77, 3865 (1996)]*, 1997.
- 79 P. E. Blöchl, *Phys. Rev. B*, 1994, **50**, 17953–17979.
- 80 G. Kresse and D. Joubert, *Phys. Rev. B*, 1999, **59**, 1758–1775.
- 81 S. Grimme, J. Antony, S. Ehrlich and H. Krieg, *J. Chem. Phys.*, 2010, **132**, 154104.
- 82 H. J. Monkhorst and J. D. Pack, *Phys. Rev. B*, 1976, **13**, 5188–5192.
- 83 G. Kresse, M. Marsman and J. Furthmüller, *VASP the GUIDE*, 2018.
- 84 N. E. Singh-Miller and N. Marzari, *Phys. Rev. B - Condens. Matter Mater. Phys.*, 2009, **80**, 235407.

- 85 A. Plauck, E. E. Stangland, J. A. Dumesic and M. Mavrikakis, *Proc. Natl. Acad. Sci. U. S. A.*, 2016, **113**, E1973–E1982.
- 86 J. K. Edwards, A. F. Carley, A. A. Herzing, C. J. Kiely and G. J. Hutchings, *Faraday Discuss.*, 2008, **138**, 225–239.
- 87 N. Dimitratos, A. Villa and L. Prati, *Catal. Letters*, 2009, **133**, 334–340.
- 88 X. Liu, M. Conte, M. Sankar, Q. He, D. M. Murphy, D. Morgan, R. L. Jenkins, D. Knight, K. Whiston, C. J. Kiely and G. J. Hutchings, *Appl. Catal. A Gen.*, 2015, **504**, 373–380.
- 89 C. Della Pina, E. Falletta and M. Rossi, *Chem. Soc. Rev.*, 2012, 41, 350–369.
- 90 T. Yonezawa, in *Nanoparticle Technology Handbook*, Elsevier, 2018, pp. 829–837.
- 91 S. Campisi, C. Beevers, A. Nasrallah, C. R. A. Catlow, C. E. Chan-Thaw, M. Manzoli, N. Dimitratos, D. J. Willock, A. Roldan and A. Villa, *J. Phys. Chem. C*, , DOI:10.1021/acs.jpcc.9b09791.
- 92 D. Astruc, in *Nanoparticles and Catalysis*, Wiley-VCH Verlag GmbH & Co. KGaA, 2008, pp. 1–48.
- 93 Z. Niu and Y. Li, *Chem. Mater.*, 2014, **26**, 72–83.
- 94 S. Campisi, M. Schiavoni, C. Chan-Thaw and A. Villa, *Catalysts*, 2016, **6**, 185.
- 95 D. J. Gavia and Y.-S. Shon, *ChemCatChem*, 2015, **7**, 892–900.
- 96 J. Cookson, *Platin. Met. Rev.*, 2012, 56, 83–98.
- 97 D. Astruc, *Inorg. Chem.*, 2007, 46, 1884–1894.
- 98 S. Mourdikoudis and L. M. Liz-Marzán, *Chem. Mater*, 2013, **25**, 1465–1476.
- 99 B. Hu, K. Ding, T. Wu, X. Zhou, H. Fan, T. Jiang, Q. Wang and B. Han, *Chem. Commun.*, 2010, **46**, 8552–8554.
- 100 Z. Li, J. Gao, X. Xing, S. Wu, S. Shuang, C. Dong, M. C. Paa and M. M. F. Choi, *J. Phys. Chem. C*, 2010, **114**, 723–733.
- 101 A. A. Athawale, S. V. Bhagwat, P. P. Katre, A. J. Chandwadkar and P. Karandikar, *Mater. Lett.*, 2003, **57**, 3889–3894.
- 102 C. J. Serpell, J. Cookson, D. Ozkaya and P. D. Beer, *Nat. Chem.*, 2011, **3**, 478–483.
- 103 T. Mayer-Gall, A. Birkner and G. Dyker, *J. Organomet. Chem.*, 2008, **693**, 1–3.
- 104 D. Li, C. Wang, D. Tripkovic, S. Sun, N. M. Markovic and V. R. Stamenkovic, *ACS Catal.*, 2012, **2**, 1358–1362.
- 105 M. M. Bittner, D. Kraus, S. V. Lindeman, C. V. Popescu and A. T. Fiedler, *Chem. - A Eur. J.*, 2013, **19**, 9686–9698.

- 106 D. K. Singh, R. Jagannathan, P. Khandelwal, P. M. Abraham and P. Poddar, *Nanoscale*, 2013, **5**, 1882.
- 107 I. Šloufová, B. Vlčková, M. Procházka, J. Svoboda and J. Vohlídal, *J. Raman Spectrosc.*, 2014, **45**, 338–348.
- 108 F. Neese, *Wiley Interdiscip. Rev. Comput. Mol. Sci.*, 2012, **2**, 73–78.
- 109 S. Grimme, S. Ehrlich and L. Goerigk, *J. Comput. Chem.*, 2011, **32**, 1456–1465.
- 110 S. Grimme, *J. Comput. Chem.*, 2006, **27**, 1787–1799.
- 111 E. F. Valeev, 2018.
- 112 D. Andrae, U. H.   ermenn, M. Dolg, H. Stoll and H. Preu , *Theor. Chim. Acta*, 1990, **77**, 123–141.
- 113 F. Weigend and R. Ahlrichs, *Phys. Chem. Chem. Phys.*, 2005, **7**, 3297.
- 114 F. Weigend, , DOI:10.1039/b515623h.
- 115 S. Grimme, *J. Chem. Phys.*, 2013, **138**, 244104.
- 116 T. Lu and F. Chen, *J. Comput. Chem.*, 2012, **33**, 580–592.
- 117 T. Lu and F. W. Chen, *Acta Chim. Sin.*, **69**, 2393–2406.
- 118 P. Vidossich and A. Lledós, *Dalt. Trans.*, 2014, **43**, 11145–11151.
- 119 J. Pipek and P. G. Mezey, *J. Chem. Phys.*, 1989, **90**, 4916–4926.
- 120 P. H.-L. Sit, F. Zipoli, J. Chen, R. Car, M. H. Cohen and A. Selloni, *Chem. - A Eur. J.*, 2011, **17**, 12136–12143.
- 121 F. Klasovsky, P. Claus and D. Wolf, *Top. Catal.*, 2009, **52**, 412–423.
- 122 H.-F. Wang, W. E. Kaden, R. Dowler, M. Sterrer and H.-J. Freund, *Phys. Chem. Chem. Phys.*, 2012, **14**, 11525–11533.
- 123 P. Sherwood, A. H. De Vries, M. F. Guest, G. Schreckenbach, C. R. A. Catlow, S. A. French, A. A. Sokol, S. T. Bromley, W. Thiel, A. J. Turner, S. Billeter, F. Terstegen, S. Thiel, J. Kendrick, S. C. Rogers, J. Casci, M. Watson, F. King, E. Karlsen, M. Sjøvoll, A. Fahmi, A. Schäfer and C. Lennartz, *J. Mol. Struct. THEOCHEM*, 2003, **632**, 1–28.
- 124 S. A. F. Nastase, A. J. O'Malley, C. R. A. Catlow and A. J. Logsdail, *Phys. Chem. Chem. Phys.*, 2019, **21**, 2639–2650.

Appendix: QM/MM Studies of Fe and Cu Containing Zeolites

As discussed in chapter 1, iron- and copper-containing zeolites have been shown to be effective catalysts for the partial oxidation of methane to methanol. Most of the work performed by the Cardiff research team shown in figure 1.5 of chapter 1 has been performed using Density Functional theory (DFT) calculations run using the Vienna Ab initio Simulation Package (VASP) which as discussed earlier is a periodic code. Since the efficiency of periodic codes reduces with unit cell size, this led us to investigate the use of QM/MM techniques which combine highly accurate quantum mechanical calculations with a fast-molecular mechanical environment. This project is in collaboration with Dr. German Sastre at Universitat Politècnica de València (UPV). The aim of this project is to use the specialisation of Sastre in force field methods to adapt the simulation methodology to QM/MM using the ChemShell package¹²³. This has been developed to use existing MM (Gulp, DLPOLY) and QM programs (NWChem, GAMESS-UK) within a python-based wrapper to control the communication between the MM and QM regions. The code is designed to run efficiently on HPC-systems and so will be ideal for looking at the oxidation mechanism within the zeolite environment.

We started by optimising the size of the cluster needed for Chabazite and Faujasite as these represent one of the smallest and largest members of the Zeolites family respectively. Since methanol production is our aim, we studied the adsorption of methanol on different cluster sizes ranging from 30-75 Bohr radius. Methanol adsorption in zeolites has been studied in detail by Nastase *et al.*¹²⁴.

The size of the active region was 25 Bohr with the size of the QM region corresponding to the first nearest neighbour atoms to the central Al. These calculations were performed with PBE using GAMESS-UK to describe the QM region and DL_POLY to describe the MM region while employing the force field of Hill and Sauer. A Split Valence Polarisation (SVP) basis set was used to represent the atomic orbitals

The adsorption energy was then computed using the formula shown in A1:

$$E_{ads} = (E_{met+zeo} - E_{zeo} - E_{met}) \quad (A1)$$

where $E_{met+zeo}$ is the electronic energy of the adsorption of methanol on the zeolite, E_{zeo} is the energy of the cluster in gas phase, and E_{met} is the energy of methanol in gas

phase.

Table A1: Adsorption of methanol on varying cluster sizes of Chabazite and Faujasite

| Radius of the cluster / Bohr radius | Adsorption Energy/ kJ mol ⁻¹ | |
|--|--|-----------------|
| | Chabazite | Faujasite |
| 30 | -134.503 | -128.422 |
| 35 | -134.348 | -128.881 |
| 40 | -134.495 | -129.018 |
| 45 | -135.036 | -129.055 |
| 50 | -134.568 | -129.078 |
| 55 | -134.500 | -129.031 |
| 60 | -134.558 | *Not converged* |
| 65 | -134.574 | *Not converged* |
| 70 | -134.739 | -129.139 |
| 75 | -134.770 | -129.070 |

As shown in table A1, the cluster size has very little effect on the adsorption energy of methanol with about only a 0.1 kJ mol⁻¹ energy difference between the clusters. In all cluster sizes, the methanol was protonated by the cluster upon adsorption. In order to ensure a sufficient gap between the MM region and the active region is present, the 55 Bohr cluster was used for further calculations.

The size of the QM region was then examined. Using the 55 Bohr radius cluster, the adsorption of methanol was studied with the size of the QM region varying from 1 nearest neighbour (NN), 3NNs, 5NNs, 7NNs, and 9 NNs. As shown in table A2, the adsorption energy varies with the number of nearest neighbours where the energy increases (becomes less negative) as you increase the size of the QM region. The adsorption of methanol on the 7NNs and 9NNs clusters was too computationally demanding and thus could not be optimised within the wall-time provided. A similar effect was seen when optimising the 5NN cluster where the job had to be submitted more than once to reach convergence.

Table A2: Adsorption Energy of Methanol on Chabazite with varying number of nearest neighbours for the QM region

| Number of nearest neighbours | Adsorption Energy/ kJ mol ⁻¹ |
|---------------------------------|--|
| 1NN | -134.500 |
| 3NNs | -128.364 |
| 5NNs | -113.367 |
| 7NNs | *Not converged* |
| 9NNs | *Not converged* |

Periodic calculations on Chabazite and Faujasite clusters were also performed. These were performed using VASP using the same computational details highlighted in chapter 3.2 but without the dipole correction and using a U value of 4 for the iron atom in the di-iron complex.

The chabazite structure used for the periodic calculations is different from the structure used for the QM/MM calculations shown above as the ratio of the Si:Al was changed to 30:1 in order to ensure comparability with the VASP results obtained in the published work. Two different configurations for the adsorption of methanol were examined: end-on and side-on (figure A1). As shown in table A3, the end-on configuration is more stable on Faujasite than on Chabazite with an energy difference of about 20 kJ mol⁻¹. Another interesting difference between the two structures is that methanol adsorbed in an end-on conformation was protonated by the zeolite on both chabazite and Faujasite. The adsorption of methanol on chabazite appears to be endothermic indicating that the adsorption is unfavourable.

Table A3: Adsorption energy of methanol on Chabazite and Faujasite

| Configuration | Adsorption Energy/ kJ mol ⁻¹ | |
|---------------|--|-----------|
| | Chabazite | Faujasite |
| End-on | +64.1 | -82.8 |
| Side-on | +61.2 | -60.5 |

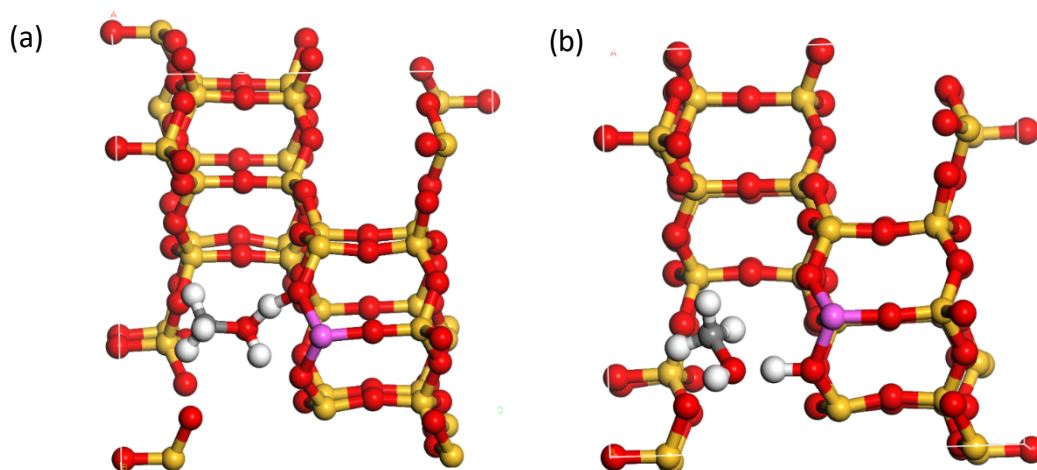


Figure A1: Adsorption of methanol on Chabazite (a) end-on configuration (b) side-on

The main active species for this reaction is a di-iron complex which has been proposed to have the following structure (figure A2):

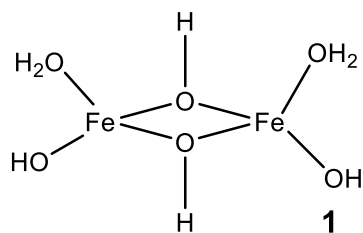


Figure A2: Structure of the di-iron complex

We started by optimising the Fe_2O_2 complex in gas phase. This was then followed by the addition of two hydroxyl groups which was then followed by the addition of two water molecules. The energy required for the addition for the addition of the hydroxyl groups onto the Fe_2O_2 complex was then computed using equation A2:

$$E_{\text{Fe}_2\text{O}_2[\text{OH}]_2} - E_{\text{Fe}_2\text{O}_2} - (2 \times E_{\text{OH}}) \quad (\text{A2})$$

Similarly, the energy required for the addition of the water molecules onto the $\text{Fe}_2\text{O}_2[\text{OH}]_2$ was computed using equation A3:

$$E_{\text{Fe}_2\text{O}_2[\text{OH}]_2[\text{H}_2\text{O}]_2} - E_{\text{Fe}_2\text{O}_2[\text{OH}]_2} - (2 \times E_{\text{H}_2\text{O}}) \quad (\text{A3})$$

The amount of energy needed to add two hydroxyl groups to the di-iron oxide complex in gas phase was found to be strongly negative with a value of -7.8 eV. The energy then to add two water molecules to the $\text{Fe}_2\text{O}_2[\text{OH}]_2$ complex in gas phase was found to be -1.9 eV.

The adsorption of the $\text{Fe}_2\text{O}_2[\text{H}_2\text{O}]_2$ complex was then studied on Faujasite. The di-iron oxide complex was first adsorbed on the cluster and optimised. This was then followed by the addition of two water molecules to the di-iron complex and optimising. The energy required for the addition of two water molecules to the adsorbed di-iron oxide structure was calculated using equation A4:

$$E_{\text{Fe}_2\text{O}_2[\text{H}_2\text{O}]_2} = E_{\text{Fe}_2\text{O}_2[\text{H}_2\text{O}]_2} - E_{\text{Fe}_2\text{O}_2} - [2 \times E_{[\text{H}_2\text{O}]}] \quad (\text{A4})$$

The energy required for the addition of two water molecules to the di-iron oxide

complex adsorbed on Faujasite was found to be only -0.41 eV

This work is still in progress. Future work will entail studying the reaction mechanism shown in figure 5 of chapter 1 using QM/MM in order to compare adsorption energies of intermediary species and activation barriers for the different steps of the reaction mechanism. These results will then be compared with the results obtained using VASP in order to determine whether both codes produce the same results.